The Pennsylvania State University

The Graduate School

Department of Mechanical and Nuclear Engineering

GPS/INS SENSING COORDINATION FOR VEHICLE STATE IDENTIFICATION AND ROAD GRADE POSITIONING

A Thesis in

Mechanical Engineering

by

Ryan David Martini

Submitted in Partial Fulfillment
of the Requirements
for the Degree of

Master of Science

August 2006

Ryan Martini

The thesis of Ryan Martini was reviewed and approved* by the following:

Sean N. Brennan
Assistant Professor, Department of Mechanical and Nuclear Engineering
Thesis Advisor

H.J. Sommer III
Professor and Interim Head Department of Mechanical and Nuclear Engineering
Thesis Reader

Stefan Thynell
Professor-In-Charge of Graduate Programs in Mechanical and Nuclear Engineering

*Signatures are on file in the Graduate School

ABSTRACT

This work demonstrates a methodology of estimating vehicle states through the use of a GPS/INS based sensing architecture. A sensing system has been developed and implemented in a vehicle for real-time data acquisition and model based state prediction. The experimental data is then used to modify existing dynamic models to improve their accuracy. Modeling results are presented in both the time and frequency domain.

A novel method of longitudinal positioning has also been developed. The method uses pitch angle measurements to estimate the disturbances input to the system from the road surface. An estimation of road grade can then be made to increase the accuracy of the longitudinal positioning solution. A model inversion process is used to make this positioning routine possible for any road vehicle. By utilizing a road grade map, the measurements of commercial grade inertial sensors may achieve positioning accuracy equivalent to that of a high end differential GPS system.

TABLE OF CONTENTS

LIST OF FIGURES

LIST OF TABLES

ACKNOWLEDGEMENTS

I would first like to thank the National Science Foundation, the Department of Mechanical Engineering and the Pennsylvania Transpiration Institute for providing me with the funding and facilities to make my graduate education possible.

Thanks to my advisor, Dr. Brennan for his endless support and guidance throughout the course of this work. He has taught me a tremendous amount about vehicle dynamics and research in general; in particular the importance of a literature review. Dr. Brennan gave me the opportunity to work on some very interesting projects which made my graduate experience quite unique.

Also, big thanks to my lab group members - especially Vishi, Haftay and Bridget. Vishi spent many hours helping me over the past two years -I believe every all-nighter I have ever had was with him. His brilliance still amazes me. With Haftay I share the unique experience of being both an NSF GK-12 fellow and a student in Dr. Brennan's lab. He is the only one who truly understands both sides of the story as we have vented many times together. Bridget has been through the sometimes painful experience of sharing a test vehicle with me. Our days in Blue Steel are not to be forgotten – I thank her for her help, her patience and her ability to calm me down when nothing seems to be working.

I would also like to thank all of the great people I have met during my six year stay in State College. In particular my undergraduate friends who I still keep in touch with. I could not have asked for a better crew to spend my time with. You are the only ones who can truly understand and appreciate my college experience.

And to my girlfriend, Kara – where would I be without you? Four perfect years with you and my love for you grows stronger every day. Years ago I would have doubted a relationship like this could have ever existed. Thank you for all of your love and support.

And last but not least, I would like to thank my parents. Over the past six years you have given me more support than I could have ever hoped for. In a time of crisis, you dropped everything to be by my side. You helped me through the most difficult experience in my life and I cannot thank you enough. Your love, hard work and dedication have made me who I am today. I hope that one day I can be as good of a parent to my children as both of you are to me. I love you both.

Chapter 1

Introduction

This thesis outlines the development, integration and implementation of a real-time data acquisition system which utilizes the Global Positioning System and inertial sensors for vehicle state identification. The system is capable of accurately estimating vehicle states and supplying control efforts in real-time for modeling, control and guidance.

This work then uses the real-time data acquisition system to investigate the planar dynamics of a passenger vehicle through the Bicycle Model. Several methods of estimating front and rear cornering stiffness values are presented and their effects on the Bicycle Model are shown through model comparisons. The Bicycle Model is then modified to account for higher-order phenomena such as tire lag and camber thrust to increase the model's accuracy. The effects of these changes are investigated in both the time and frequency domains.

The data collection and modeling efforts of this work revealed very strong terrain influences on vehicle state measurement. This dependence suggested a new method of vehicle localization through the analysis of road input disturbances. Pitch-plane vehicle models were derived and used in an inversion process to assist in this positioning routine and made the generalization of this positioning methodology possible on any passenger vehicle.

1.1 Motivation

Over the past several years vehicle research groups in the automotive industry and academia have turned their focus to integrating computer-based systems into vehicles in order to increase safety by assisting the driver in high-risk situations. Today, driver-assist systems such the Anti-lock Brake System (ABS) and Electronic Stability Program (ESP) come standard in many vehicle makes and models. These two systems use various sensors to detect excessive wheel slip and automatically apply or adjust braking forces when deemed appropriate. These systems are successful because the control actions can be applied faster and more consistently by a computer than by the average driver.

As computer processing power increases and cost decreases, more advanced sensing technology can be integrated into the vehicle. The increased computational power allows for data processing in real-time and for the development of model-based predictive algorithms. By continuously monitoring the vehicle states and using this data in vehicle models running onboard the vehicle, advanced safety systems such as Rollover Detection and Lane Detection become possible.

In order for these systems to be successful, accurate vehicle models must be developed. It is critical that the models are sufficiently complex to accurately predict the vehicle's dynamics while still remaining as simple as possible to allow real-time implementation onboard vehicle processors.

A large portion of this work was motivated by a previous study by John Cameron [1]. In Cameron's study, a sensing system architecture was developed and used in a vehicle model comparison between several 3 Degree of Freedom (DOF) roll models found in literature. The system was used to analyze rollover mitigation algorithms. The sensing system was based on commercial grade rate sensors and accelerometers which were inherently noisy and susceptible to drift. Therefore, an accurate estimation of vehicle attitude (roll, pitch and yaw) was difficult to obtain through integration of these sensor readings. At the conclusion of Cameron's work, the quality of the test data was brought into question as the system exhibited a poor Sensor-to-Noise ratio. It was determined that a more accurate sensing architecture was needed for a more thorough model comparison.

This thesis began with the development and integration of a military grade GPS/INS-based data acquisition system for vehicle dynamic studies. A detailed description of the system components, functionality and capabilities is presented. GPS/INS based sensing has been used extensively in literature with a vehicle dynamics focus [2-9]. Most relevant to this work are those of Ryu and Bae [4, 9] of Chris Gerdes' group at the Dynamic Design Laboratory at Stanford University and the research group of Dave Bevly [7] of the GPS and Vehicle Dynamics Laboratory at Auburn University. Although the hardware components used in these other projects are not the same as used here, it must be noted that these research groups laid important ground work on the subject and therefore their work will be referenced extensively in this thesis.

With this new sensing system in place, it was necessary to re-perform all experimental tests presented in Cameron's work. This includes both frequency- and time-domain analysis. As a parallel to Cameron's work, [1], the planar Bicycle Model is revisited. This work will show significant differences between the results presented in [1] and those determined with the new sensing architecture. Perhaps the most important model-based result presented here is a new method of cornering stiffness estimation. Common methods of cornering stiffness estimation presented in [1] as well as in vehicle dynamics texts such as [10, 11] were attempted first before a new method is developed. The differences between the previous methods and the one developed for this work are explained and discussed.

After the basic low-order planar model is established, higher-order dynamics such as tire lag and camber effects are investigated and found to be necessary for adequate model fit. These effects are most easily seen in the frequency domain. Results show that the addition of these phenomena increases the model's accuracy without greatly increasing its complexity.

Throughout the analysis of the experimental data, the effects due to the non-uniform terrain became apparent. These effects were determined to be highly repeatable and location dependent. These two characteristics allow the terrain effects to be used to assist in a positioning solution. The terrain influences have been studied previously in works such as [6] where they were removed from the state estimates to improve state accuracy. Also, the concept of Road Grade positioning was investigated in [12] where the terrain effects were identified with commercial grade sensors; however, performance was limited in positioning accuracy due to its inferior computing and sensing architecture – a pressure sensor to measure changes in vehicle height – as well as its lack of vehicle dynamic considerations. This work attempts to eliminate these shortcomings.

This work will also derive and compare multiple Pitch-plane models to help achieve higher accuracy in a terrain-based positioning method. The goal of incorporating vehicle dynamics into the correlation algorithm is to allow the terrain disturbance positioning routine to be used on a wide range of passenger vehicles and speeds.

1.2 Outline of Remaining Chapters

The remaining chapters of this work will structured as follows:

Chapter 2 will present the basic concepts behind GPS and INS systems and their integration into a vehicle data-acquisition system. Although the fine technicalities of each of these sensors will not be presented, it is important for the users of the data acquisition system to have a fundamental understanding of the principles of operation of each component.

Chapter 3 will present the standard 2 DOF planar Bicycle Model which is used extensively throughout this work. Its derivation will be given as well as an explanation of the physics behind the model

Chapter 4 will describe the vehicle instrumentation that is used in this study. This includes the GPS/INS system, the steering sensors and the custom real-time data acquisition system.

Chapter 5 outlines a methodology of vehicle parameter estimation utilizing data collection and the Bicycle Model. The experiments performed will be explained, and a discussion will be given on how the data is post-processed for model comparison. A new method of cornering stiffness estimation is explained, and it is compared to more traditional methods that are common in literature.

Chapter 6 will present a modification to the Bicycle Model to incorporate tire lag while Chpater 7 will add the effects of camber.

Chapter 8 introduces the concept of using Road Grade and road disturbances to help assist in the positioning solution. The preliminary analysis used as a proof-of-concept is described before the process is refined further in Chapter 9.

Chapter 9 includes the refinement of the road disturbance positioning routine as well as the introduction and implementation to several Pitch-plane models. These models are used in an inversion process to increase the accuracy of the positioning routine and to generalize measurement of a single vehicle at a single velocity to any vehicle (with known model) at any velocity. To identify pitch-model characteristics, a method of estimating vehicle spring constants and damping coefficients is given and the effects of the model inversion are demonstrated through simulation and experimental data.

Chapter 10 will present the thesis conclusions as well as the future work.

Appendix A consists of the detailed portions of the Pitch-plane model derivations from Chapter 9.

Appendix B outlines a detailed example of the data acquisition code. This is necessary for users who will follow this work and need to adjust the system to accommodate additional system inputs.

Appendix C is a data acquisition system troubleshooting guide to be used as necessary.

1. Cameron, J.T., *Vehicle Dynamic Modeling for the Prediction and Prevention of Vehicle Rollover*. 2005: The Pennsylvania State University.
2. Chen, G. and D.A. Grejner-Brzezinska. *Land-Vehicle Navigation Using Multiple Model Carrier Phase DGPS/INS*. in *Proceedings of the 2001 American Control Conference*. 2001. Arlington, Virginia.
3. Farrell, J., T. Givargis, and M. Barth. *Differential Carrier Phase GPS-Aided INS for Automotive Applications*. in *Proceedings of the 1999 American Control Conference*. 1999. San Diego, California.
4. Ryu, J., E.J. Rossetter, and J.C. Gerdes. *Vehicle Sideslip and Roll Parameter Estimation using GPS*. in *AVEC 2002: 6th International Symposium on Advanced Vehicle Control*. 2002. Hiroshima, Japan.
5. Yang, Y., J. Farrell, and H.-S. Tan. *GPS-aided INS based Control State Calculation for AHS*. in *Proceedings of the 2001 American Control Conference*. 2001. Arlington, Virginia.
6. Ryu, J. and J.C. Gerdes. *Estimation Of Vehicle Roll And Road Bank Angle*. 2004. Boston, Massachusetts.
7. Bevly, D.M., et al. *The Use of GPS Based Velocity Measurements for Improved Vehicle State Estimation*. in *Proceedings of the 2000 American Control Conference*. 2000. Chicago, Illinois.
8. Bevly, D.M., R. Sheridan, and J.C. Gerdes. *Integrating INS Sensors with GPS Velocity Measurements for Continuous Estimation of Vehicle Sideslip and Tire Cornering Stiffness*. in *Proceedings of the 2001 American Control Conference*. 2001. Arlington, Virginia.
9. Bae, H.S., J. Ryu, and J.C. Gerdes. *Road Grade and Vehicle Parameter Estimation for Longitudinal Control Using GPS*. in *Proceeings of IEEE Conference on Intelligent Transportation Systems*. 2001.
10. Gillespie, T.D., *Fundamentals of Vehicle Dynamics*. 1992: Society of Automotive Engineers (SAE). 495.
11. Karnopp, D., *Vehicle Stability*. 2004, New York: Marcel Dekker, Inc.
12. Holzapfel, W., M. Sofsky, and U. Neuschefer-Rube, *Road Profile Recognition for Autonomous Car Navigation and Navstar GPS Support.* IEEE Transactions on Aerospace and Electronic Systems, 2003. **39**(1): p. 2-12.

Chapter 2

Introduction to GPS and INS: History, Background and Basic Functions

This chapter will introduce the fundamentals of two major components of the vehicle sensing system: the Global Positioning System (GPS) and the Inertial Navigation System (INS). Although it is not necessary to know all theoretical details of these systems in order to understand the use of GPS in passenger vehicle applications, a conceptual understanding is necessary for proper implementation and troubleshooting. This chapter provides an essential foundation for using these sensors in a vehicle dynamic study.

2.1 GPS Background

The Global Positioning System is a Department of Defense operated radio-based navigation system consisting of 24 satellites orbiting approximately 11,000 miles above the surface of the earth. The GPS of today has evolved from early radio navigation systems such as MIT's LORAN (Long Range Area Navigation) system of the 1940's [1]. Initially developed for military use, the system was declared available to civilian use in 1983 and by 1984 the commercial GPS market began to take off though its use in surveying. The Global Positioning System can best be described in three main segments: Space Segment, Control Segment and User Segment. Below is a description of each, followed by a description of their integration together.

2.1.1 Space Segment

The space segment consists of a constellation of 24 NAVSTAR (NAVigation Satellite Timing and Ranging) Satellites which orbit the earth at 11,000 miles above the surface. The present constellation consists of 24 operational satellites deployed in six evenly spaced planes (A to F) with an inclination of 55 degrees and with four satellites per plane [2]. This arrangement guarantees 4-8 visible satellites from any given point on the earth assuming open sky visibility. These solar powered satellites orbit the earth once every 12 hours at a speed of 3.9 km/s. Each satellite is equipped with 4 atomic clocks accurate to a billionth of a second.

The NAVSTAR's accuracy is directly affected by the accuracy of each satellite's onboard atomic clocks. These clocks are used to synchronize all system processes and to produce the fundamental L-band carrier frequency on which GPS data is modulated. The two frequencies used by GPS are denoted L1 (1575.42 MHz) and L2 (1227.60 MHz). Civilian GPS receivers use only the L1 frequency on which navigation data and Coarse Acquisition (C/A) code for Standard Positioning Service (SPS) is transmitted. On the other hand, the L2 frequency only carries P-Code (or encrypted P-Code, called Y code) to be used by receivers designed for Precision Positioning Service (PPS) – namely military grade receivers. The C/A code is purposely omitted from the L2 carrier which allows the Joint Program Office (JPO) to control the information broadcast by the satellites and allows them to deny full system accuracy to nonmilitary users [2].

2.1.2 Control Segment

The control segment consists of one Master Control Station (MCS) and five Monitoring Stations (MS). The main operational tasks for the control segment are to track the satellites for orbit, clock determination and prediction, to perform time synchronization of the satellites, and to upload this information in a data message to the satellites to ensure accurate position solutions [2]. One MS is located at the MCS, at the Falcon Air Force Base in Colorado Springs, Colorado, and the remaining four are located on Hawaii, Ascension, Diego Garcia and Kwajalein islands. These stations collect altitude, position, speed and the health of the orbiting satellites for all satellites in view, and send this information to the MCS for real-time data processing. This whole process is performed twice a day by each of the Monitoring Stations. From the data collected, the MCS calculates any position or clock errors for each satellite and sends these corrections back to the satellites for more accurate solutions for the end-user.

2.1.3 User Segment

The user segment is the most well known portion of the entire GPS system. As one may imagine, this segment is made up of all users who receive GPS satellite data. This includes military, civilian and commercial users. The uses for GPS amongst these groups are for the most part, common knowledge. This work will only investigate the use of GPS in the user segment defined by civilian and commercial users – namely the automotive industry, and the ability to use a GPS system as a sensor to measure vehicle states. One must note that upon inception, the Global Positioning System was designed as a two-tiered system in which military capability was far superior to commercial and civilian ability. The DoD strictly regulated the accuracy of non-military users though Selective Availability (SA). Today, the differences between these two sectors have decreased tremendously as the commercial and civilian sector have researched ways around SA to improve accuracy without military-grade equipment.

2.2 GPS Functionality

With the three segments outlined, the system can be explained in a straight forward manner. First, the simple or ideal case can be described to demonstrate how a satellite's position in orbit can translate into precise position on the earth's surface. After the ideal case is explained, more technical content will be presented.

2.2.1 Ideal Description

Each satellite transmits its own specific binary code which is modulated on a carrier frequency. Although the code may appear to be noise, it is actually unique to each satellite and completely predicable given the right algorithm. Because of this noise-like appearance, the code is referred to as Pseudo-Random Noise (PRN). Each receiver on earth has the ability to regenerate the carrier frequencies as well as the PRN codes for each satellite. When the receiver locks onto a satellite, it can compare the code being received with that it has stored.

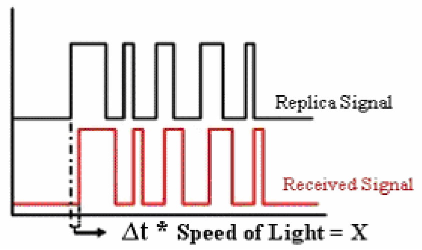

Figure 2.1: Replica and Received Signal Comparison

The receiver can then estimate the signal travel time by subtracting the time its internal clock registers from the time indicated by the satellite when it transmitted the relevant pulse (phase lag of the received signal from that generated within the receiver)[1]. The travel time can then be multiplied by the speed of light to tell the receiver how far it is from a given satellite – X miles. This then implies that the receiver is located somewhere on the surface of a sphere that has a radius of X miles, and is centered at the location of the satellite. When calculated for three satellites in three dimensional space, the three spheres will intersect at 2 points. One of which will be on the earth's surface, while the other intersection point will be either off in space or well below the earth's surface and therefore can be disregarded. Thus the remaining point will be the user's location on the earth's surface. This process is represented pictorially in Figure 2.2:

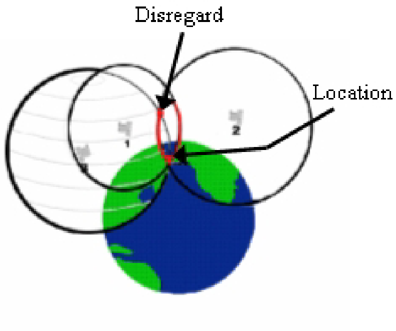

Figure 2.2: Ideal GPS Positioning

The simple description of GPS operation presented above does not capture all of the intricacies of GPS. Although many of these issues fall beyond the scope this work, it is necessary to have a greater understanding than the ‘ideal’ case in order to implement a GPS system in a vehicle environment. Because of this, a more descriptive, but not a complete description of the details of GPS has been included below.

2.2.2 Technical Description

2.2.2.1 Satellite Signals

Each NAVSTAR Satellite transmits three codes in the form of Pseudo-Random Noise (PRN) modulated on the two carrier frequencies – L1 and L2. There are two ranging codes referred to as the Coarse Acquisition Code (C/A) and Precision code (P-Code) as well as a Navigation message code which contains critical satellite information. All three of these codes are modulated on the L1 frequency, and only the P-code is modulated on the L2 frequency. They are modulated on each carrier signal by a rarely used modulation method called Bi-Phase Modulation (as opposed to the Amplitude Modulation (AM) and Frequency Modulation (FM) of common radio signals). In Phase Modulation the carrier signals phase reverses when data transmission starts and then re-syncs phase at the end of transmission. This modulation method is discussed further in [2], and shown in Figure 2.3:

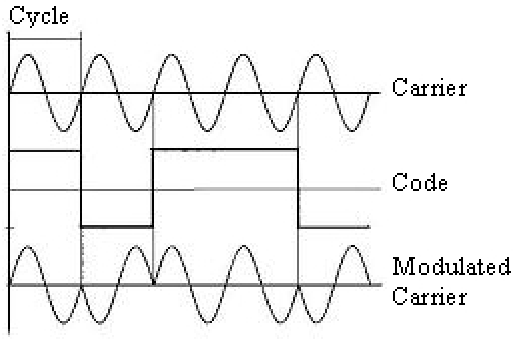

Figure 2.3: Bi-phase Modulation of Carrier Wave

The general public has been given free access to the C/A code on the L1 carrier frequency. Each satellite has its version of the C/A code characterized by each satellites PRN number. These messages are relatively short in length (1023 bits) and are repeated every millisecond. A GPS receiver capable of reading C/A code on the L1 frequency can use its own internal clock to replicate the L1 carrier frequency signal as well as the PRN signals from each satellite. The receiver can then compare these replicated signals (sometimes called reference signals) with those received to generate ranges as described previously.

In addition to the C/A code on the L1 frequency, each satellite also transmits a Navigation message containing its orbital elements, clock behavior, system time and status messages. An almanac is also provided which gives the approximate location for each active satellite so the receiver can track and lock onto additional satellites more efficiently. The information in the Navigation message being sent by each satellite is monitored and updated by the MCS and its monitoring stations to ensure accuracy. At all times the MCS knows exactly where each satellite is, and where it should be next.

Until the year 2000, non-military users operating on the L1 frequency were affected by a service called Selective Availability (SA). SA is the intentional degradation of GPS messages on the L1 frequency. SA was put in place by the DoD to stop users from having dangerously accurate systems. During this time, when C/A messages were decoded on a single receiver one could achieve accuracy on the order of 100 meters in the horizontal direction. As the demand for a more accurate, non-military system increased, users found ways around SA. This eventually led to the cancellation of SA in 2000 and users gained access to the full accuracy of the C/A message – approximately 15 meters in the horizontal direction on a single receiver. This system of receiving and processing free C/A code on the L1 frequency is known as the Standard Positioning Service (SPS).

The DoD and people authorized by the government can have access to the P-code that is modulated on both carrier frequencies. When necessary, this code can be further encrypted to Y-code for added security through a method called anti-spoofing. The code is much longer than the C/A code at 2e14 bits (37 weeks long). Each satellite transmits a different 7 day segment of code before the code is reset. The pure length of this message makes it nearly impossible for unauthorized users to gain access. Advanced dual frequency receivers use the C/A code on startup to help track and match the longer P-code. When demodulated by the receiver, the P-code message gives accuracy to approximately 5-8 meters. This is known as the Precision Positioning Service (PPS).

2.2.2.2 Calculating Position

Each GPS receiver uses its own internal clock (usually inexpensive quartz crystal oscillators) to replicate the L-band carrier frequencies as well as the available PRN codes. It then uses bi-phase modulation to combine the PRN codes with the carrier signal to generate reference signals for each satellite. By aligning and comparing its reference signals to those received from the satellites, the receiver can calculate the phase lags between the two signals. This phase lag corresponds to the signal travel time from the satellite to the phase center of the GPS antenna. This time multiplied by the speed of light gives the receiver-satellite range. If the receiver's onboard clock could *exactly* match that of the satellite, a receiver would be able to precisely calculate its position from only three satellite ranges. In practice this is not possible because the quartz clock has an inherent time drift which creates a timing offset from true GPS time. Because of this offset, the distance measured to the satellite is slightly longer or shorter than the "true" range [2]. Thus, the calculated distance is not the true range, but a pseudorange. The pseudorange measurement can typically be modeled as:

$$P_n = (t_k - t^n) \cdot c \qquad \textbf{2.1}$$

Where P_n is the pseudorange between the receiver and satellite *n*; t_k is the receiver clock time, t^n is the satellite transmit time and c is the speed of light.

Both the receiver and satellite have their own clock biases which create errors in the true range calculation. The satellite clock bias can be modeled as a polynomial whose coefficients are transmitted to the receiver in the Navigation message [2]. The satellite bias can then be easily removed from the range calculation. The receiver can then estimate its own clock bias by calculating pseudoranges for four satellites instead of three. The four pseudorange equations will allow the receiver to solve for the four unknowns – three position components and the receiver clock bias. The equation set can be represented by equation **2.2**

$$(X_n - U_x)^2 + (Y_n - U_y)^2 + (Z_n - U_z)^2 = (P_n - C_R)^2 \ \text{n} = 1,2,3,4 \qquad \textbf{2.2}$$

Where U_x, U_y and U_z are the receivers coordinates, $X_n, Y_n,$ and Z_n are the position coordinates of satellite *n* and C_R is the receiver clock bias which is common for all four ranging solutions [1]. The clock bias can then be removed from the pseudorange calculations for a more accurate position solution.

$$R_n = P_n - c \cdot C_R \qquad \textbf{2.3}$$

Where R_n is the true distance from satellite n, and P_n is the corresponding pseudorange and C_R is the receiver clock bias. The Code Pseudorange calculation and correction above can result in approximately 3m accuracy on an L1 single frequency receiver, and 30cm on an L1,L2 dual phase receiver.

Users with very stringent accuracy requirements can utilize Carrier Phase (or Phase Psedudoranging) GPS. This method of calculating distance measures the phase of the GPS carrier wave and compares that to the replica carrier [3]. Compared to Code Pseudorange algorithms, much more accurate position solutions can be achieved: carrier-based algorithms can achieve accuracies of 1-2 cm [4]. This method is typically used in Real-Time Kinematic differential positioning solutions. In order to perform this measurement, the receiver removes the known PRN code from the received satellite signal. After PRN removal, the received signal still contains the navigation message which can be decoded and eliminated by high-pass filtering. The final result is the Doppler-shifted carrier on which phase measurement can be performed [2].

The Carrier Phase to be measured is the difference between phase of receiver's replica signal and the signal received plus the number of cycles at the initial start of tracking. This number will have an integer and fractional component, e.g. 123456789.871 cycles. The fractional component, if known, can be used to provide additional time resolution which therefore provides additional resolution in the position estimate.

The derivation of the carrier phase positioning technique is presented in [2] and its details will not be presented here. The method is based off of electromagnetic wave propagation and is beyond the scope of this work. The resulting equation however, has been re-written to agree with previous notation and is presented in equation **2.4**

$$\Phi = \frac{1}{\lambda} R + \frac{c}{\lambda} C_R + N \qquad \mathbf{2.4}$$

Where Φ is the measurable phase, λ is the wavelength, C_R is the receiver clock bias, c is the speed of light, R is the true range and N is the initial number of cycles between the satellite carrier wave and that replicated by the receiver upon initial signal tracking.

By multiplying the frequency equation, equation 2.4 (expressed in cycles) by the wavelength, λ, of the carrier a range equation is formed.

$$P_n = R_n + c \cdot C_R + N\lambda \qquad \textbf{2.5}$$

Rearranging equation 2.5 allows for direct comparison to the Code Pseudorange equation presented earlier.

$$R_n = P_n - c \cdot C_R - N\lambda \qquad \textbf{2.6}$$

Comparing equation 2.6 to equation 2.3 shows that the Carrier Phase measurement differs from the Code Pseudorange measurement by only an integer number of wavelengths. Hofmann-Wellenhof, [2], points out that the phase of a carrier can be measured to 1% (0.01 cycles) of its wavelength which corresponds to millimeter precision, assuming no other errors are introduced.

2.2.2.3 Single and Dual Frequency Receivers

The military-grade dual frequency receivers have several advantages over the single frequency receivers. Their access to the coded messages on the L1 and L2 frequencies give them superior accuracy for various reasons, two of which are presented here.

As discussed above, a receiver can calculate its position using Code Pseudoranging or both Code Pseudoranging and Carrier Phase positioning. If only C/A code is available for a given receiver, it may only use the above techniques on the messages transmitted on the L1 frequency. However, if a receiver has access to both C/A and P(Y)-Code, it may perform these calculations on both frequencies. By having access to the P(Y)-Code on the L2 frequency, a receiver can directly remove the code from the L2 frequency and use the underlying Doppler shifted carrier frequency for Carrier Phase positioning. Without knowledge of the P(Y)-code, one has to use codeless or quasi-codeless techniques for reconstruction of the unmodulated carrier wave from which the phase of the base carrier is measured [1]. The codeless and quasi-codeless techniques are inherently less accurate than the coded method.

Another advantage of dual frequency receivers are their ability to estimate ionospheric and atmospheric delays. In the previous cases, it was assumed that the satellite signal propagated at the speed of light. It must be noted that this is only true in a vacuum. In practice, satellite signals see a delay while traveling though the ionosphere which is approximately proportional to the amount of free electrons the signal encounters [1]. In the dual frequency system, differences in the Ll and L2 observations are used directly solve for the ionospheric delay thus reducing ionospheric effects [5].

2.2.3 Differential GPS

Differential GPS (DGPS) was initially developed to eliminate the errors introduced through SA. It is a system which combines two GPS receivers to produce a position solution accurate to 3-5 meters even when only standard L1 C/A code is used. One receiver, referred to as the base station, is setup at a fixed, known location and remains stationary at that point for its entire operation. This receiver's job is to receive data from the L-phase carriers, compute the position indicated by the received data as in ordinary GPS operation, and then calculate the error between the computed solution and the known location. The base station estimates the slowly varying error components of each satellite range measurement and forms a correction for each GPS satellite in view [3]. These error and bias calculations are then broadcasted on a communication link to the second GPS receiver known as the rover station[4]. The rover is free to move and receives these corrections via radio, internet or other communication means. The rover uses the base stations corrections for every satellite used in its position calculations.

DGPS operation drastically increases accuracy and almost entirely removes timing biases due to satellite clock error, ionospheric and tropospheric, and ephemeris prediction errors.

2.2.3.1 DGPS Issues

When considering the use of DGPS as a sensor for vehicle state identification, there are several issues which need to be resolved. Perhaps the most important issue is the possibility of GPS outages when a direct line of sight to satellites is not available. A GPS receiver is not capable of accurate positioning when less than 4 satellites are available for its calculations. Tunnels, buildings, trees and other environmental factors make GPS outages common in vehicle applications. This lack of signal requires the use of additional sensors to compliment the DGPS system.

Another issue with GPS is the relatively slow update rate of the sensor, only 5 to 20Hz at best. The low update rate of GPS leads the system to high frequency errors which also cause problems in vehicle applications.

Because of these shortcomings, alternate sensing configurations have been investigated for many years. Due to their complimentary nature, much attention has been paid to the integration of an Inertial Navigation System (INS) to existing GPS systems.

2.3 INS Background

Chatfield, [6], defines Inertial Navigation as the computation of current velocity and position from initial velocity and position and the time history of the kinematic acceleration. This definition is based on the concept that a vehicles current velocity is equal to the initial velocity plus the integral of the vehicles acceleration with respect to time. Similarly, the vehicles position is equal to its initial position plus the integral of the vehicles velocity with respect to time. Therefore if an initial velocity and position is known, it is possible to position a vehicle by simply measuring accelerations and performing the integration and addition described above.

Inertial Navigation Systems, which perform this type of positioning, were initially developed in the late 1940's for aircraft navigation. The systems have since been refined for high accuracy and small size.

2.4 INS Functionality

INS systems use measurements captured from an Inertial Measurement Unit (IMU) to calculate position of a vehicle in the inertial frame. The IMU is a sensor which uses three accelerometers (X, Y, Z) and three rate gyros (roll, pitch and yaw) to measure how a vehicle is moving and rotating in space. The system uses these measurements to integrate and solve differential equations to estimate vehicles position, velocity and attitude relative to initially known states. These estimates can be made available as fast as they system computer can calculate them.

Although the INS system can offer high speed, continuous estimates of position, velocity and attitude, these estimates are subject to integration error over long periods of time. Small errors in acceleration readings grow as they are integrated over time – this results in large errors in velocity estimates and even larger errors in position calculations. These errors make it necessary to restart or correct stand alone INS systems to ensure accurate operation. Since INS calculates change in system orientation and acceleration, it needs initial values for these parameters to be input from an external source.

2.5 GPS/INS Integration

The complimentary nature of GPS and inertial navigation has been well known since the inception of GPS. In theory, the continuity of the inertial system can both fill in positioning gaps left by GPS satellite outages and reduce the effect of high frequency GPS errors, while the unbiased nature of the GPS signals can limit the size of the low frequency errors in the inertial system [7]. The integration of GPS/INS creates an accurate, high speed positioning system that can continue to operate when satellite visibility is limited. This integration of these sensors is system-specific but is usually performed though a Kalman filtering process which corrects the INS positioning solution with that of the GPS. This integration will be discussed in more detail in Chapter 4.

1. Logsdon, T., *Understanding the NAVSTAR: GPS, GIS and IVHS*. Second ed. 1995, NY, NY: Van Nostrand Reinhold.
2. Hofmann-Wellenhof, B., H. Lichtenegger, and J. Collins, *GPS: Theory and Practice*. Fourth, revised edition ed. 1997, Austria: Springer-Verlag Wien New York.
3. Parkinson, B.W. and J.S.J. (eds), *Global Positioning System: Theory and Applications, Volume II*. In: Progress in Astronautics and Aeronautics, Vol 164, ed. P. Zarachan. 1996, Washington, D.C.: American Institute of Aeronautics and Astronautics, Inc.
4. Novatel, *OEM4 Family of Receivers User Manual - Vol. 1 Installation and Operation, OM-20000046, Rev. 19*. 2005: Alberta, Canada.
5. Janet Brown-Neumann, A.M., Thomas Ford, Orest Mulyk, *Test Results from a New 2 cm Real Time Kinematic GPS Positioning System*. 1996: The Institute of Navigation, Washington DC. p. 183.
6. Chatfield, A.B., *Fundamentals of High Accuracy Inertital Navigation*. Progress in Astronautics and Aeronautics, Vol 174, ed. P. Zarchan. 1997, Washington, D.C.: American Institute of Aeronautics and Astronautics, Inc.
7. Tom Ford, J.N., P. Fenton, M. Bobye, J. Hamilton. *OEM4 Inertial: A Tightly Integrated Decentralised Inertial/GPS Navigation System*. 2001. Salt Lake City, Utah.

Chapter 3

Two Degree-of-Freedom Model

The planar dynamics of a vehicle is often represented in the form of single track, 2 degree of freedom model known as the Bicycle Model. This model has been used extensively throughout literature because of its ability to accurately model a vehicle's lateral velocity and yaw dynamics. It is defined on a body fixed coordinate system which is centered at the vehicle center of gravity and which rotates and translates with the vehicle. In this chapter the derivation of the bicycle model and an important handling characteristic, the understeer gradient, will be given.

3.1 Bicycle Model Derivation

Figure 3.1 shows the Bicycle Model layout and Table 3.1 describes the model parameters. Note that the tire slip angles are shown to be negative in the figure.

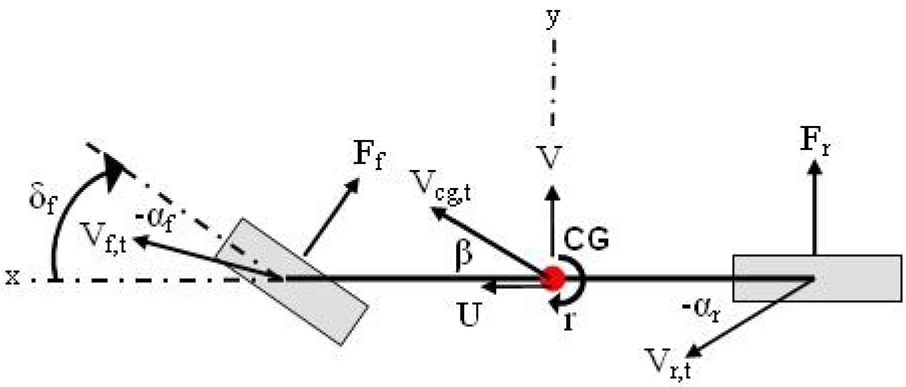

Figure 3.1: Bicycle Model

Table 3.1: Bicycle Model Parameters

Symbol	*Parameter Description*
$V_{cg,t}$	Total velocity vector at CG
U	Longitudinal velocity
V	Lateral velocity
r	Yaw rate about Z axis
β	Side slip angle
δ_f	Front steering angle
α_f	Front slip angle
$V_{f,t}$	Total velocity vector at front tire
F_f	Lateral force generated at front tire
α_r	Rear slip angle
$V_{r,t}$	Total velocity vector at rear tire
F_r	Lateral force generated at rear tire

The coordinate system definition is presented in Figure 3.2

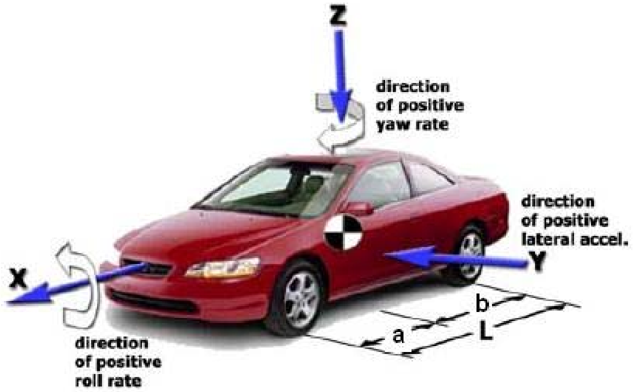

Figure 3.2: SAE Coordinate System Definition

Several assumptions must be made when using the bicycle model formulation. First, the vehicle mass and tire forces are both assumed to be symmetric about the X-Z plane. Therefore the vehicle can be modeled as a single-tracked vehicle where the two front and two rear wheels can be represented together as a single front and single rear wheel respectively. The vehicle is also assumed to have constant longitudinal velocity, *U*, and tires which roll without slipping in the longitudinal direction. This means there are no acceleration or braking forces being applied. The front and rear tires are also assumed to produce lateral forces which are linearly proportional to their respective cornering stiffnesses. Finally, the model also assumes all angles are small, and therefore the following simplifications can be applied:

$$\cos(\theta) \cong 1$$
$$\sin(\theta) \cong \theta$$

The states, or variables required to fully describe the motion of the bicycle model are *V*, the vehicles lateral velocity at the CG, and *r*, the angular velocity about the z-axis.

The equation of motion of the vehicle can be derived using Newtonian mechanics as described below.

Summing forces in the lateral direction, summing moments about the Z axis and applying the small angle approximation the following equations are obtained:

$$\begin{gathered} m \cdot a_y = \sum F_y = F_f \cos(\delta) + F_r \cong F_f + F_r \\ I_{zz} \cdot \frac{dr}{dt} = \sum M_z = F_f \cos(\delta) \cdot a - F_r \cdot b \cong F_f \cdot a - F_r \cdot b \end{gathered} \qquad \mathbf{3.1}$$

Under the assumption that the front and rear tire lateral forces are linearly dependent on their respective slip angles and cornering stiffnesses, and negative cornering stiffness values are used

$$\begin{gathered} F_f = C_{\alpha f} \cdot \alpha_f \\ F_r = C_{\alpha r} \cdot \alpha_r \end{gathered} \qquad \mathbf{3.2}$$

The front and rear slip angles can be solved for by looking at the lateral and longitudinal velocities at each tire as in Figure **3.3:**

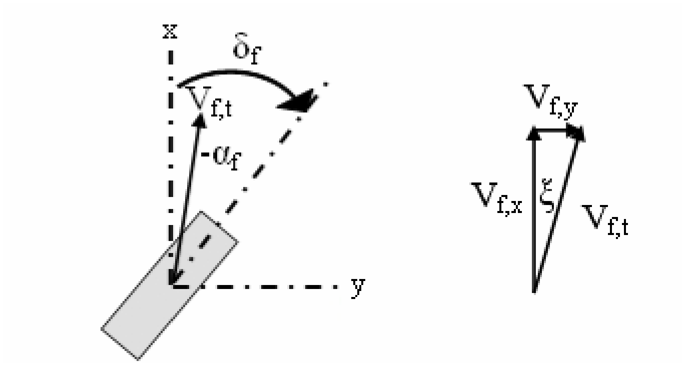

Figure 3.3: Wheel Velocity Vector Summation

Assuming small angles, we can then write:

$$\xi = \tan^{-1}\left(\frac{V_{f,y}}{V_{f,x}}\right) \cong \left(\frac{V_{f,y}}{V_{f,x}}\right) \qquad 3.3$$

And from geometry:

$$\alpha_f = \xi - \delta_f \qquad 3.4$$

The lateral velocity vector for the front tire can be written as:

$$V_{f,y} = V + a \cdot r \qquad 3.5$$

Longitudinal velocity is approximately equal to the vehicles velocity at the center of gravity:

$$V_{f,x} \cong U \qquad 3.6$$

By combining equations. 3.5, 3.5 ,3.5, and 3.6 the equation for front slip angle can be formed:

$$\alpha_f = \frac{V + a \cdot r}{U} - \delta_f \qquad 3.7$$

By repeating the above procedure for the rear tire and recalling that there is no steering input at the rear, the equation for rear slip angle can be written

$$\alpha_r = \frac{V - b \cdot r}{U} \qquad 3.8$$

Combining equations 3.2, 3.2, 3.7 and 3.8:

$$m \cdot a_y = C_{\alpha f}\left(\frac{V + a \cdot r}{U} - \delta_f\right) + C_{\alpha r}\left(\frac{V - b \cdot r}{U}\right) \qquad 3.9$$

$$I_{zz} \cdot \frac{dr}{dt} = C_{\alpha f}\left(\frac{V + a \cdot r}{U} - \delta_f\right) \cdot a - C_{\alpha r}\left(\frac{V - b \cdot r}{U}\right) \cdot b \qquad 3.10$$

Lateral acceleration in body-fixed coordinates can be expressed as:

$$a_y = \frac{dV}{dt} + U \cdot r \qquad 3.11$$

Rearranging equations 3.9 , 3.11 expressions for lateral acceleration and the time rate of change of the yaw rate can be written:

$$\frac{dV}{dt} = \left(\frac{C_{\alpha f} + C_{\alpha r}}{m \cdot U}\right) \cdot V + \left(\frac{C_{\alpha f} a - C_{\alpha r} b}{m \cdot U} - U\right) \cdot r + \left(\frac{-C_{\alpha f}}{m}\right) \cdot \delta_f \qquad 3.12$$

$$\frac{dr}{dt} = \left(\frac{C_{\alpha f} a - C_{\alpha r} b}{I_{zz} \cdot U}\right) \cdot V + \left(\frac{C_{\alpha f} a^2 + C_{\alpha r} b^2}{I_{zz} \cdot U}\right) \cdot r + \left(\frac{-C_{\alpha f} a}{m}\right) \cdot \delta_f \qquad 3.13$$

Equations. 3.12 and 3.13 can be represented in standard state space form as in equation 3.14:

$$\begin{bmatrix} \frac{dV}{dt} \\ \frac{dr}{dt} \end{bmatrix} = \begin{bmatrix} \frac{C_{\alpha f} + C_{\alpha r}}{m \cdot U} & \frac{C_{\alpha f} a - C_{\alpha r} b}{m \cdot U} - U \\ \frac{C_{\alpha f} a - C_{\alpha r} b}{I_{zz} \cdot U} & \frac{C_{\alpha f} a^2 + C_{\alpha r} b^2}{I_{zz} \cdot U} \end{bmatrix} \cdot \begin{bmatrix} V \\ r \end{bmatrix} + \begin{bmatrix} \frac{-C_{\alpha f}}{m} \\ \frac{-C_{\alpha f} a}{m} \end{bmatrix} \cdot \delta_f \qquad 3.14$$

3.1.1 Derivation of Understeer Gradient

A vehicle’s handling behavior can be characterized by a parameter known as the understeer gradient. In this study, the understeer gradient will be used for its ability to relate a vehicles weight distribution to its tires’ force generating abilities. The understeer gradient is a widely used parameter in vehicle dynamics, and its full derivation can be found in many text books including [1], and [2]. It was also presented in previous work, [3]. For simplicity, only a brief derivation has been included here.

Figure 3.4 shows a 2 DOF, single track vehicle in a high speed steady state turn of radius *R*. The forces are shown in the positive direction; however the slip angles are shown as negative in agreement with SAE standards.

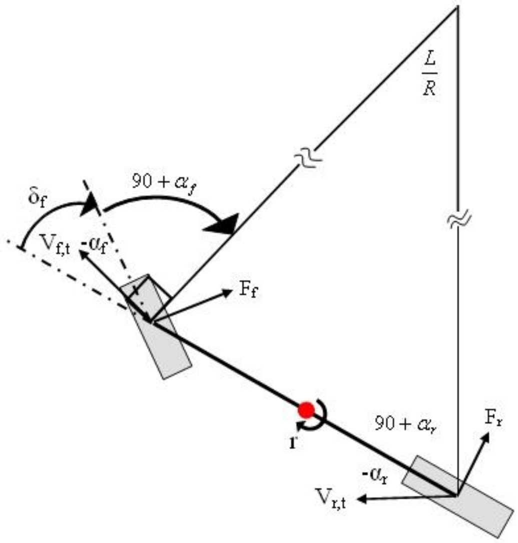

Figure 3.4: Bicycle Model - Steady State Turn

By summing the interior angles of the triangle, an equation for the required steering input to negotiate the turn can be solved:

$$\delta_f = \frac{L}{R} - \alpha_f + \alpha_r \quad \mathbf{3.15}$$

As in equation 3.1 the sum of forces in the lateral direction the sum of moments about he Z axis gives:

$$\begin{aligned} m \cdot a_y &= F_f + F_r \\ I_{zz} \cdot \frac{dr}{dt} &= F_f \cdot a - F_r \cdot b \end{aligned} \quad \mathbf{3.16}$$

In a steady state turn the acceleration in the lateral direction is exactly equal to the centripetal acceleration:

$$a_y = \frac{U^2}{R} \qquad 3.17$$

In order for the vehicle to be at steady state, it must be in equilibrium about its center of gravity, and therefore the sum of moments about the z axis must be zero. By combining equations 3.16, 3.17 and setting the sum of moments to zero gives:

$$m\frac{U^2}{R} = F_f + F_r \qquad 3.18$$

$$F_f \cdot a = F_r \cdot b \qquad 3.19$$

In the standard bicycle model derivation, the lateral force generated by the tires was assumed to be proportional to each tires' cornering stiffness. Therefore equations 3.18 and 3.19 can be rearranged and combined with equation 3.2:

$$\begin{aligned} F_f &= \frac{b \cdot m}{L} \cdot \frac{U^2}{R} = C_{\alpha f}\alpha_f \\ F_r &= \frac{a}{b} \cdot F_f = \frac{a \cdot m}{L} \cdot \frac{U^2}{R} = C_{\alpha r}\alpha_r \end{aligned} \qquad 3.20$$

Where the cornering stiffness vales are *negative* quantities. To simplify, recognize that the weight on the front and rear axle can be written:

$$\begin{aligned} W_f &= \frac{m \cdot g}{L} \cdot b \\ W_r &= \frac{m \cdot g}{L} \cdot a \end{aligned} \qquad 3.21$$

Equation 3.20 can then be re-written in terms of vehicle axle weights and solved for the front and rear slip angles:

$$\begin{aligned} \alpha_f &= \frac{W_f}{C_{\alpha f}} \cdot \frac{U^2}{gR} \\ \alpha_r &= \frac{W_r}{C_{\alpha r}} \cdot \frac{U^2}{gR} \end{aligned} \qquad 3.22$$

Combining 3.22 with 3.15 gives:

$$\delta_f = \frac{L}{R} + \frac{U^2}{gR} \cdot \left(\frac{W_r}{C_{\alpha r}} - \frac{W_f}{C_{\alpha f}} \right) \qquad 3.23$$

Again the cornering stiffness values are *negative* quantities.

Equation 3.23 is used extensively in literature for its ability to correlate parameters which are easy to measure (steer angle, velocity, turn radius, vehicle length and axle weights) to quantities which are difficult to measure (front and rear cornering stiffnesses). From equation 3.23 the understeer gradient, K_{us}, is defined.

$$K_{us} = \left(\frac{W_r}{C_{\alpha r}} - \frac{W_f}{C_{\alpha f}} \right) \qquad 3.24$$

Once again it must be noted that the cornering stiffness values used in equation 3.24 are *negative* values.

The understeer gradient derived in this section is important in characterizing the steering characteristics of a vehicle. A vehicle with a positive understeer gradient will be referred to as an understeer vehicle. The steering input required for an understeer vehicle to negotiate a steady state turn increases as the speed of the vehicle increases. On the other hand, a vehicle with a negative understeer gradient is known as an oversteer vehicle. An oversteer vehicle actually requires decreasing steering inputs to negotiate a turn for increasing speeds. Production vehicles are predominately understeer since oversteer vehicles become unstable in certain turning maneuvers. Further discussion of this topic can be found in many vehicle dynamics text books, [1, 2], or in previous work [3], and will not be presented here.

1. Gillespie, T.D., *Fundamentals of Vehicle Dynamics*. 1992: Society of Automotive Engineers (SAE). 495.
2. Karnopp, D., *Vehicle Stability*. 2004, New York: Marcel Dekker, Inc.
3. Cameron, J.T., *Vehicle Dynamic Modeling for the Prediction and Prevention of Vehicle Rollover*. 2005: The Pennsylvania State University.

Chapter 4

Vehicle Systems and Integration

This chapter will outline the sensing system layout and then present each component of the system. Pictures of the system are presented at the end of the chapter. A 1992 five door Mercury Tracer has been selected as the test vehicle for this study. The vehicle is equipped with a military grade GPS/INS system, linear string potentiometer steering sensors and an onboard DSP based data acquisition system. The integrated system currently measures roll, pitch, yaw, velocity magnitude, velocity direction, latitude, longitude, altitude and steering angle in real time at a rate of 50Hz. If necessary the system can also output accelerations, angular rates and various other measurements at 100Hz. This system has significant advantages over systems used in previous studies.

4.1 Vehicle System Layout

The current vehicle system can most easily be described in four parts: the Rover Station, the Base Station, the Steering Sensors and the Data Acquisition system. The Rover Station, steering sensors and Data Acquisition system are installed in the vehicle while the Base Station remains outside the vehicle in a fixed location. Each of these parts will be descried in the subsequent sections of this chapter. Figure **4.1** below shows a general block diagram of the entire setup:

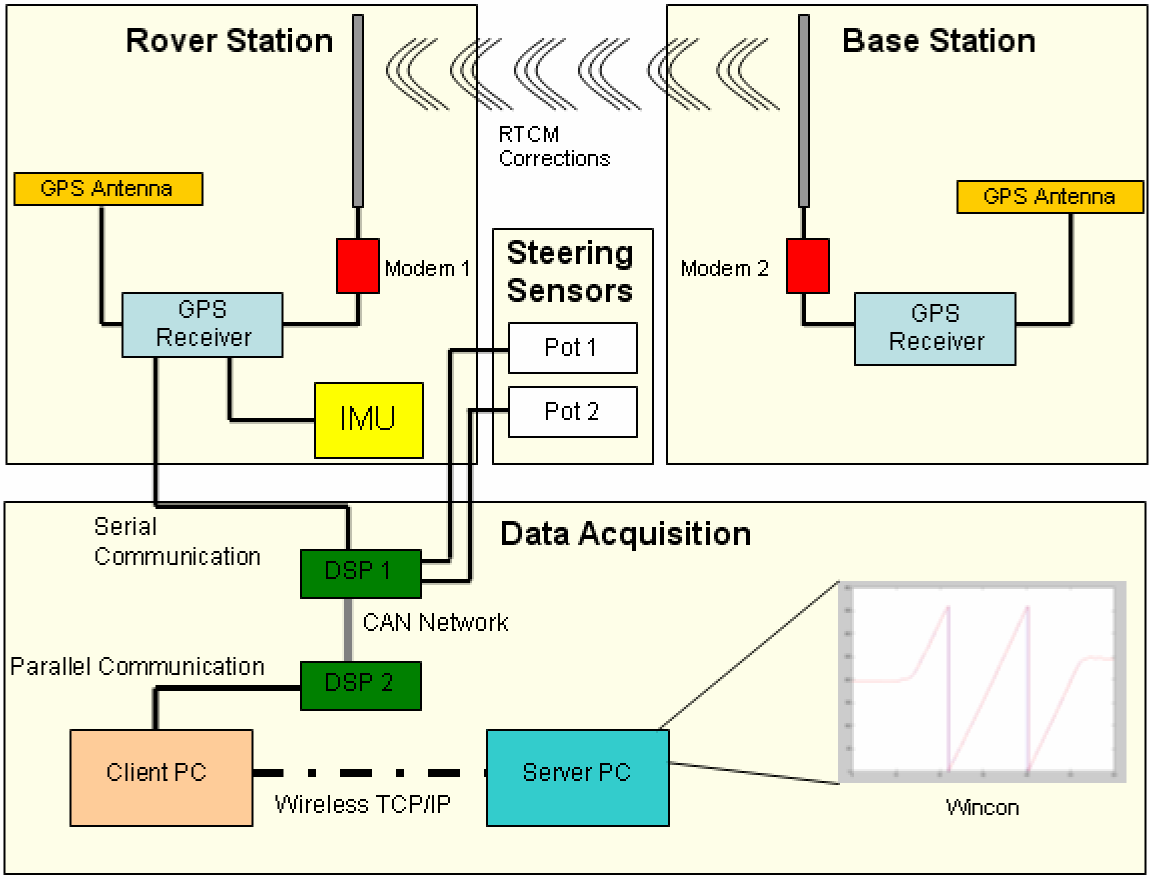

Figure 4.1: System Layout

4.1.1 Part 1: Rover Station – GPS/INS system

The Rover GPS/INS sensing system being used is the NovAtel SPAN (Synchronized Position Attitude Navigation) system based off two OEM4 dual frequency GPS receivers and the Honeywell HG1700 military tactical-grade IMU. This GPS/INS combination can provide estimates of position, velocity and attitude at rates up to 100Hz. In differential carrier phase fixed-integer mode and with continuous presence of GPS data, the system achieves a position solution with an accuracy of 2 cm (one sigma). Attitude can be estimated with an accuracy of 0.013 degrees for roll and pitch and 0.04 degrees for yaw while velocity error is a mere 0.007 m/s (one sigma) [1].

The GPS portion of the Rover system is a NovAtel DL4plus receiver which has modified software and hardware to accommodate interfacing with the HG1700 over a standard RS-232 serial port. The DL4plus is a dual frequency (L1/L2) receiver capable of both pseudorange and carrier phase positioning. These receivers can transmit GPS measurements at a rate of 20 Hz. In situations where GPS outages occur, they typically have L1 and L2 frequency reacquisition times of 0.5 and 1 second respectively. The DL4plus is equipped with NovAtel's patented Pulse Aperture Correlator (PAC) technology to virtually eliminate the effects of multipath errors seen in environments where buildings or other signal obstacles may exist [2].

Figure 4.2: NovAtel DL-4 Plus Receiver

The INS portion of the system consists of the Honeywell HG1700 AG17 strap-down ring laser gyro IMU used primarily in missile guidance systems, unmanned aerial vehicles and standoff weapons. This IMU exhibits a gyro bias of only 10 deg/hr and an acceleration bias of 3 milli-g [3]. The HG1700 is mounted in a 160 x 160 x 100mm case from which it can measure accelerations and rotational rates in all directions. Internally, velocity and angle changes are sampled at 600 Hz. NovAtel's firmware applies non-linear corrections to the raw measurements which makes these measurements available in their navigation software at a 100 Hz rate [4]. The IMU measurements are taken in its body frame as defined by the sensor axis of the IMU. The measurements then require a transformation into the vehicle's body frame to accurately determine vehicle attitude, velocity and accelerations.

Figure 4.3: Honeywell HG1700 IMU – NovAtel Enclosure

4.1.1.1 GPS/INS Integration

The SPAN system integrates the GPS and INS systems through two separate, but interacting filters in a decentralized Kalman filtering process. A Kalman filter is a procedure that broadly consists of two steps used to optimally estimate a series of parameters that describe the behavior of a system [5]. In Real-Time operation, the SPAN systems decentralized Kalman filter has 15 states: Earth Centered Earth Fixed (ECEF) position, velocity, attitude Euler angles with respect to the ECEF frame and gyro and accelerometer biases with respect to the IMU body frame [4]. The filter system collects IMU's measurements and time-tags them with the GPS time. It then uses a decentralized approach to generate a blended GPS/INS solution.

The filtering process of the SPAN system has been referred to as decentralized because the GPS and inertial processing occur in two separate filters. The advantages and disadvantages of using such a process have been discussed in great detail in [4, 5] and will not be discussed here. The two filters interact by sharing position and position covariance information. The GPS filter assists the inertial filter by supplying it with GPS position measurements to be used to control the error growth in the inertial filter. The inertial filter assists the GPS filter by supplying it with inertial position measurements to expedite satellite reacquisition times incase of signal interference or blockage. This integration process allows the system to be much more accurate than either GPS or INS alone. Further details of the Kalman filtering process, including the exact methodology of the propagation and update steps of the filter can be found in [5].

4.1.1.2 Rover Station Calibration

The Rover Station's GPS/INS system required several calibration steps in order to achieve centimeter level accuracy. The calibration procedure consists of three main steps which are described below.

The first step of calibration is performed automatically by the DL-4plus and IMU on startup. When it is initially powered, the IMU has no information regarding its mounting orientation. Although the IMU is labeled with its own body coordinates, X,Y,Z, it does not assume that Z is always inline with the gravity vector. In order to resolve its orientation, a calibration known as frame detection takes place on system startup.

> The alignment of the inertial system to the vehicle's body frame is derived with a combination of the measured accelerations of the IMU compared to the gravity vector, and the angular rate measured by the IMU compared to the earth rate. The alignment computation requires that the system does not experience any specific forces except gravity, is not physically rotating except from earth rotation, and that gyro bias in the unit is small compared to the earth rate [6].

The DL-4plus automatically completes this inertial system alignment after it locks onto four satellites and an initial position can be calculated from GPS. During this stationary calibration, the IMU's roll and pitch alignment is 0.18 degrees while it is only 45 degrees for yaw. The yaw is particularly inaccurate because of the system is using the latitude and the earths rotational rate to resolve the yaw angle. This calculation is therefore skewed by the high gyro drift to earth rate ratio [5]. However, over time the stationary system will resolve the yaw heading to within a few degrees (approximately 5 degree accuracy after 300 seconds at 40 degree latitude). In order to expedite the process, the system should be put in motion after the frame detection and coarse alignment and is complete. This will make the yaw angle observable and therefore increase its accuracy at a quicker rate. As the yaw accuracy improves, the INS status message in GPSolution will change from “Coarse Alignment Complete” to “INS Solution Good.” Data collection should only be performed after this occurs as the yaw angle will not be accurate until then.

It must also be noted that this frame detection procedure does not “zero” the IMU’s attitudes (roll, pitch, yaw) after mounting. Therefore the angular offsets due to mounting the IMU will show as constant offsets in the attitude data. This is accounted for by subtracting these values off the readings in data post processing.

The second stage the rover station calibration is to estimate the leverarm. The leverarm is defined as the three dimensional distance between the GPS antenna’s phase center, and the IMU’s center. The leverarm estimate is given to the DL-4plus through the GPSolution software via the SETIMUTOANTOFFSET command. After an accurate leverarm estimate is given, the receiver can precisely calculate the given leverarm through the built in LEVERARMCALIBRATE routine. NovAtel recommends the antenna’s phase center and IMU center be as close as possible, and if possible, should only be offset in the vertical direction. The antenna/IMU alignment and the accuracy of the initial estimate directly affect the accuracy of the calculated leverarm. Because of this, the initial measurement was taken carefully.

Since the antenna and IMU are separated by the vehicle windshield, an accurate initial leverarm estimate was not as straight forward as one may assume. Because the entire system has to be modular, modifying the vehicle for this measurement – such as removing the windshield - was deemed inappropriate. The easiest way to make this measurement was to use a plumb bob. The plumb bob was fixed to the GPS antenna at its phase center, and then lowered until the bob’s point touched the windshield. A mark was then made on the outside of the windshield at the point of contact and the strings length was measured. Then the process was repeated from the inside of the vehicle with the string fixed at the point of contact marked from the previous step. The bob was lowered to the center of the IMU, and once again the string length was measured. Although this is not an exact distance calculation, it was appropriate for an initial leverarm estimate.

Table 4.1: Leverarm Estimate

Inertial Frame Coordinate	Offset (m)	Uncertainty (m)
X	-0.02	+/- 0.03
Y	-0.09	+/- 0.03
Z	0.99	+/- 0.03

After the initial leverarm estimate was measured, and its X,Y and Z offsets were given to the DL4plus via the SETIMUTOANTOFFSET command, the receivers LEVERARMCALIBRATE routine could be run. During this built in calibration routine, the vehicle was driven in several maneuvers such as circles and figure eights. The routine runs until the user specified uncertainty is met (minimum 0.02 m) for all three offsets. After approximately 2 minutes, the calibration returned the calculated lever arm and the settings were automatically saved in system memory.

Table 4.2: Calculated Leverarm

Inertial Frame Coordinate	Offset (m)	Uncertainty (m)
X	-0.01	+/- .002
Y	-0.13	+/- .003
Z	1.04	+/- .02

Since the leverarm has been saved to memory, the leverarm calibration only needs to be performed if either the IMU or antenna is remounted.

The final stage of the rover calibration requires aligning the IMU body frame coordinate system with that of the vehicle. This routine allows the system to align itself while in motion if necessary and gives the user exact coordinate system rotational offsets to use in data post-processing. Once again, the DL4plus had a built in calibration routine, RVBCALIBRATE, which computed the coordinate system angular offsets and saved them into system memory. The routine consisted of the same circle and figure eight driving maneuvers used in the leverarm calibration. At the end of calibration, it returns the values for these offsets in the VEHICLEBODYROTATION log as:

Table 4.3: Vehicle Angular Offsets

Inertial Frame Coordinate	Offset (deg)
Pitch	-9.273
Roll	-0.071
Yaw	0.204

The angles in the above table indicate the angles offsets due to the IMU mounting. For example, while driving in a straight line, the velocity direction angle and the yaw angle will have a 0.204 degree disagreement. It is important that this is taken into account in data post processing for accurate attitude measurements. After this calibration was complete, the DL4plus receiver's settings are saved so the process only needs to be performed when the IMU is remounted.

4.1.2 Part 2: Base Station – GPS system

The base station also utilizes the NovAtel DL4plus receiver. Unlike the Rover station, this receiver has not been modified to communicate with the IMU. As described in previous sections, the base station is responsible for calculating and transmitting corrections to the Rover so that Real Time Kinematic differential GPS is possible. The base station and rover receivers are capable of communicating both pseudorange and carrier phase corrections for differential mode operation in standard RTCM (Radio Technical Commission for Maritime Services) format. This communication is accomplished using two FreeWave wireless radio modems set in a master/slave configuration which have a range of approximately 10 miles. The modems communicate with a baud rate of 56,200 bps and transmit RTCM 1, RTCM 3, RTCM 22, and RTCM 18/19 messages. Message type 1 contains the differential GPS corrections, message types 3 and 22 contain the base station and extended base station parameters respectively to be used in the Real Time Kinematic solution and message types 18 and 19 contain raw carrier phase and pseudorange measurement information [7], [8]. After the base station is powered on and calibrated, it automatically transmits the RTCM corrections to the Rover.

4.1.2.1 Base Station Calibration

In order for the base station to transmit proper corrections, it must compare its calculated position from satellite signals to its known position. According to NovAtel, a single stationary DL4plus receiver is capable of calculating its position accurate enough for base station operation in approximately 1 hour, however to ensure accuracy the position calculation was allotted 24 hours. After the calculation was complete, a FIXPOSITION command was given to the DL4plus to save its current position into system memory. Table **4.4** summarizes the calibrated base station position.

Table **4.4**: Base Station Position

WGS84 Coordinate	
Latitude (degrees)	40.86313783175
Longitude (degrees)	-77.83490273560
Ellipsoid Height (m)	367.353

The base station location was chosen by allowing it to send RTCM corrections to the rover, and then monitoring this communication as the vehicle was driven around the PTI test track. It was confirmed that the FreeWave wireless radio modems could successfully communicate the RTCM corrections for the vehicle's entire route, so the base station location was deemed appropriate. The current position is located on the loading dock on the left side of the skid pad as shown in Figure **4.4**

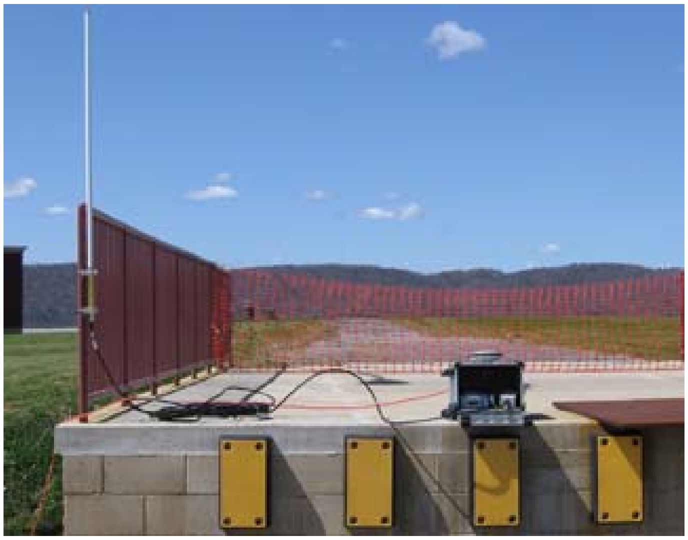

Figure 4.4: Base Station Location

4.1.3 Part 3: Steering Sensors

As in [9], the sensors used to determine the steering angle of the vehicle were linear string potentiometers. These sensors work well with this application because they are simple to use, and can be read on system startup or after momentary power outages without having to be returned to a zero or home position. As with any standard potentiometer, the linear string potentiometer returns a voltage proportional to the applied reference voltage and the position of the sensors wiper with respect to one of the end terminals. In the case of the string potentiometer, the output voltage is linearly dependent on the wiper position which is linearly dependent on the string's extension length.

In previous work [9], two of these potentiometers were mounted to the vehicle for redundancy purposes. The base of each sensor was mounted to the undercarriage of the vehicle via a custom mounting bracket with one sensor's cable mounted to the driver's side steering arm and the other on the passenger's side steering arm. In [9] and at the beginning of this study a constant 5V differential (0-5V) reference voltage was applied to each potentiometer. After several data sets were collected, it was determined that a 5V differential reference was not sufficient to supply angle readings with the necessary accuracy. Because of this, the reference voltage was increased to a 30V differential (-15V to 15V) via custom circuit based on the Autodyne SB1R5-515D regulator chip.

Due to the limited number of analog inputs available, previous studies, [9], only used one of the two potentiometers for steer angle readings. In this study this was determined to be inappropriate. In practice, a vehicles steering angle on each side of a vehicle will be different in order to optimize tire wear and performance. The exact difference is dictated by the vehicles Ackerman geometry and is a function of the vehicle's physical dimensions. Because of this, in this study both steering sensors were calibrated and the average angle recorded from both sensors was used as the true steering angle. This method is in agreement with the bicycle model which assumes the forces (and hence steering angles) on either side of a vehicle are symmetric and treats the four-tire model as a two-tire, single track vehicle.

4.1.3.1 Steering Sensor Calibration

The calibration routine in [9] was repeated in this work for each of the steering sensors. The vehicle was first driven in a straight line for 30 seconds, and the steering sensor output voltages were recorded. The vehicle was then driven in the opposite direction over the same path and once again the output voltage was recorded. The average reading for each sensor was taken, and this voltage was used as the sensors reading for zero steer angles.

Slip plates were then used to record the voltages of each steering sensor at 5 degree increments. Theses voltage readings were plotted with their corresponding angles, and best fit lines applied to each data set. Figure **4.5** shows the results of both sensor calibrations, and their best fit lines.

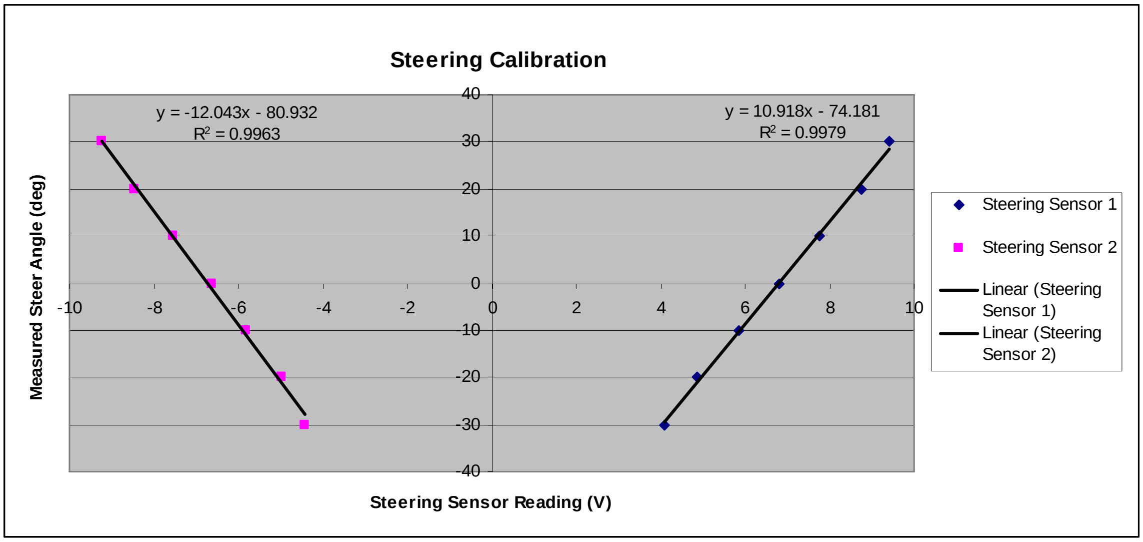

Figure 4.5: Steering Sensor Calibration

Figure 4.5 shows that voltage-angle relationships are linear with R^2 values of 0.9979 and 0.9963 respectively. Therefore the equations for the best fit lines were deemed appropriate for the voltage-angle conversion. As discussed earlier, the steer angles are computed for both steering sensors and their average reading is used for model-fits.

As pointed out in [9], the zero angle voltage of the string potentiometers tends to drift with over time when the system is not in operation. To account for this, before each data collection session the vehicle was driven along a laser aligned guide rail and the steering sensor voltages were recorded. This was then repeated with the vehicle heading the opposite direction. The (non-zero) angles calculated from the steering sensor voltage conversion for this straight line data were then subtracted from the angle readings for all data sets recorded during that session. This simple calibration routine improves the consistency of the system by eliminating any constant angle offset that may occur.

4.1.4 Data Acquisition System

The DL4plus comes with the ability to record data to an onboard compact flash card for post processing. This data acquisition routine would be sufficient for general vehicle dynamic studies and model matching. However, since the vehicle in this study will eventually require real-time control capabilities, it was necessary to setup a real-time data acquisition system capable of regulating control efforts for future use. The data acquisition system installed in the Tracer consists of two Texas Instruments TMS320C6713 Digital Signal Processor (DSP) Developer's Kits operating on a CAN bus, and a remotely accessible and programmable standard PC platform consisting of two windows-based PC's. The DSP and PC platform functionality are described below.

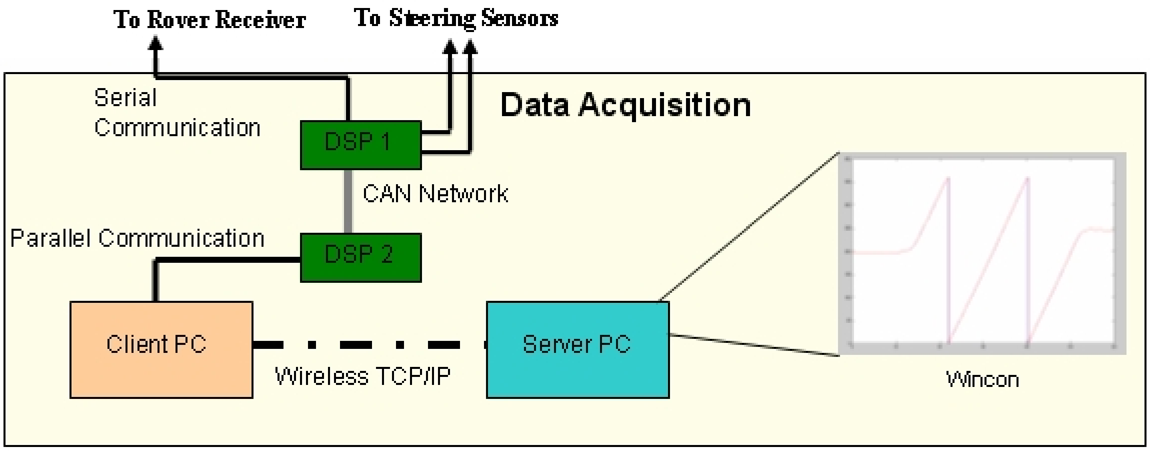

Figure 4.6: DAQ Overview

4.1.4.1 DSP Operation

The dual Texas Instrument DSP's are the heart of the current data acquisition system. Interfacing with the DSP chips is accomplished through standard address and data-bus pin headers. The pin headers allow for expansion via custom designed daughter cards such as the Digital I/O and CAN boards used in this project. The TI DSP's allow for the boards to be programmed via Code Composer Studio (CCS) – a standard C-code programming suite included with the developer's kit.

4.1.4.1.1 Interface DSP

In the current configuration, one DSP is responsible for data collection off of the rover DL4plus as well as reading the analog steering sensors. In order to accomplish this, this "Interface DSP" has been fitted with a custom daughter card developed by Dan Block at the Control Systems Instructional Laboratory at the University of Illinois at Urbana-Champaign. This I/O board gives the Interface DSP 4 analog I/O's, 8 Digital I/O, 2 RS-232 Serial Ports and an I2C Data bus.

Interfacing with the rover DL4plus is accomplished through standard serial RS-232 communication. When programmed, the DL4plus outputs its data logs in either ASCII or binary format. Since the system was designed for real time processing, the fastest possible communication was required – therefore binary format messages are transmitted. NovAtel's SPAN and OEM4 manuals present each log's header and message format which can be used to decode these logs on the processor side. The algorithm used to process the incoming messages on the Interface DSP has been outlined in the form of a flow chart in Figure **4.7** and will be explained in the paragraphs which follow.

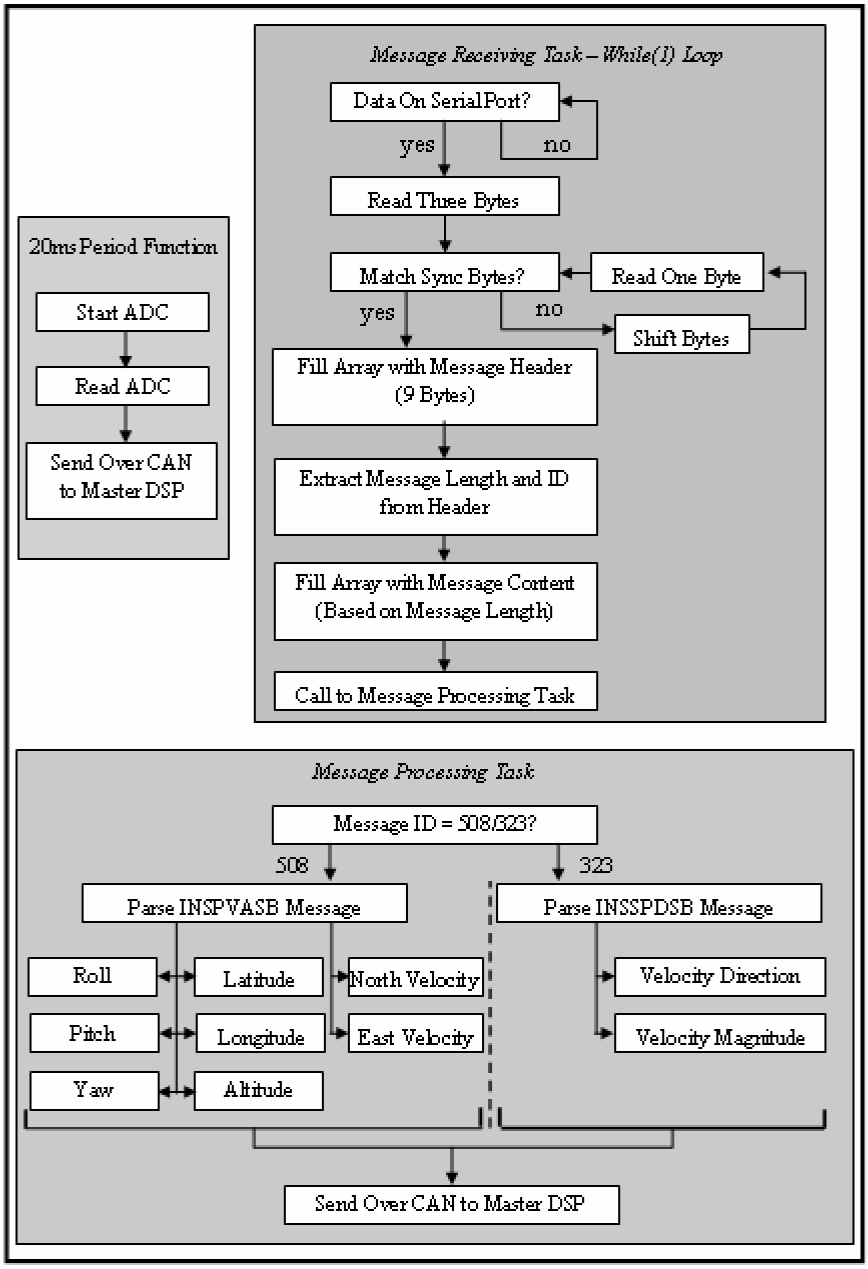

Figure 4.7: Interface DSP Algorithm

Using the CCS programming environment, the interface DSP was programmed with the above algorithm. A brief description of the algorithm described here and a detailed example of this code has been included in Appendix B.

The DSP continually monitors the serial ports of the Digital I/O board for incoming messages in the Message Receive Task. When specific sync characters (specified by NovAtel) are detected, this Task fills arrays with the message header and content. When the message is ready, Message Receive Task calls the Message Processing Task. In this second task, the DSP can identify the message content from the ID number extracted from the 9 byte header. Then variables such as roll, pitch and yaw can be extracted from their respective logs by their individual bytes according to the log format specified by NovAtel. In the current setup, the interface board decodes the receivers messages, extracts the desired variables and then transmits the ones needed for post processing over a CAN bus to the second DSP.

The Interface DSP also reads the two steering sensor string potentiometers through its analog I/O channels. The DSP is setup to perform the analog to digital conversion and read the converted value off of the ADC7864 chip at 50 Hz. Since the highest input frequency used in this work was approximately 4-5 Hz, the 50 Hz sampling rate is fast enough to capture all data without aliasing according to the Nyquist-Shannon Sampling Theorem. Sample rates above 50Hz were observed to cause system delays for unknown reasons and therefore were not used. The I/O channels on the DSP used to read the ADC data are limited to -10 to 10V. Since in the systems current configuration the string potentiometers only operate in a small portion of their maximum range, a 30V differential was applied to each potentiometer to give high resolution readings which still remained in the -10 to 10V range.

A more detailed description of the DSP programming, including sections of the code included in Appendix B.

4.1.4.1.2 Master DSP

After messages are decoded on the Interface DSP, they are transmitted to a second DSP referred to as the Master DSP via custom Controller Area Network (CAN) daughter cards designed by Vishisht Gupta of The Pennsylvania State University. The Master DSP has been programmed to run a continuous loop which prepares and sends the data received on the CAN bus over a parallel port to the Server PC. It was necessary to include this second DSP in the data acquisition system to ensure enough processing power was available for future vision and control integration. Also, the parallel port transmission requires continuous processor time which is not available on the Interface DSP due to the interrupts required to run the steering sensor ADC process. The master DSP's CAN processing code was developed by Vishisht Gupta and needed not modification for this project. It's details will not be presented here.

4.1.4.2 PC Operation

The data acquisition system's PC platform is used to monitor and record data in real-time after it has been processed by the DPS's. It also supplies the user a graphical interface via MATLAB's Simulink from which the user can adjust parameters such as controller gains, for real-time system modification and tuning. The PC platform is divided between a Client PC and a Server PC. This division allows the user to monitor data from outside the vehicle. The PC platforms functionality is described below.

After the dual DSPs acquire, process and re-send the GPS and steering sensor data over the parallel port, the data is received by the first half of the PC platform – the client PC.

The client PC has a 400 Mhz Pentium III processor which runs the client portion the Wincon software package. Wincon allows Simulink models to be run in real time and ensures that the real-time process is afforded the highest CPU priority and is not pre-empted by any competing tasks other than the core operating systems functions [10]. The data received on the Client PC is then immediately transmitted to the Server PC.

The Server PC runs MATLAB's Simulink along with the Wincon server to supply the user with a graphical interface for data monitoring and recording. Custom S-Functions were written which Wincon allows the user to save data files in standard MATLAB formats, which greatly simplifies post-processing. The Client-Server communication is accomplished via the standard TCP/IP network protocol. This is a built in capability of Wincon, which allows the users to monitor and record data in real-time from outside the vehicle, or anywhere internet is available. In the future this allows controller gains and other system inputs to be modified remotely.

An unfortunate downfall of the Wincon package is its inability to transmit variables of type double. This issue with the software prevents the user from monitoring latitude and longitude data collected from the GPS. In order to collect and save this data, it is transmitted as 4, 16 bit sections and reassembled in post processing. Since this data is almost always transformed into local planar coordinates during post processing, the DSP has been programmed to directly do this transformation in Real-Time. This eliminates the need to transfer data of double precision as the local X,Y data is calculated in meters can be captured with a float precision variable. This code however has not been tested at this time.

4.2 System Setup Pictures

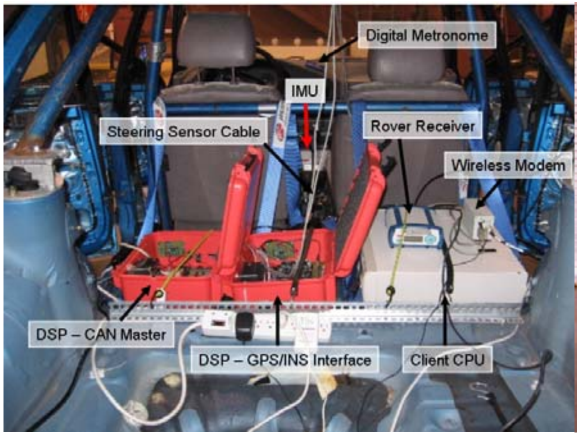

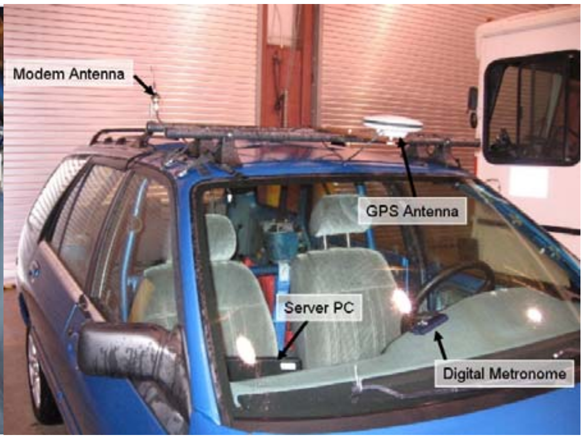

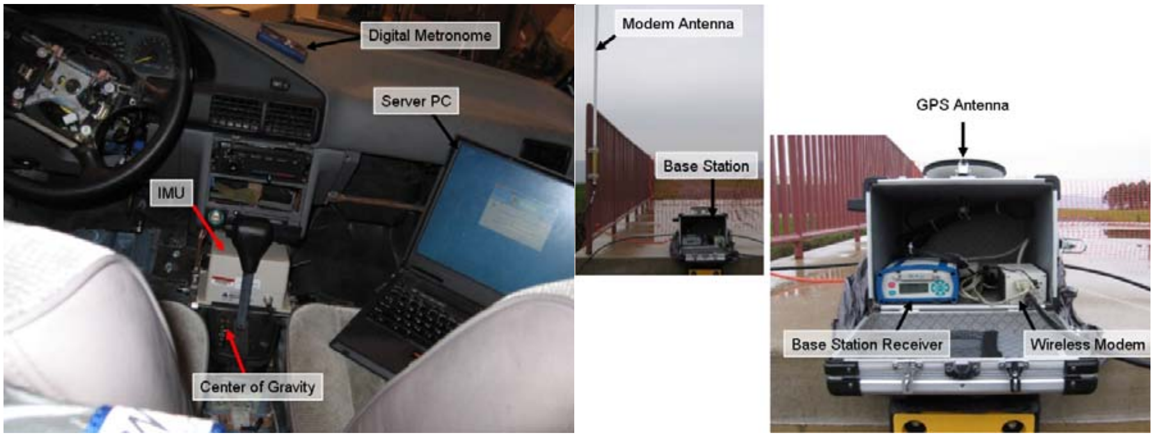

1. NovAtel, *SPAN Technology System Characteristics and Performance*. 2005: Alberta, Canada.
2. NovAtel, *NovAtel DL-4plus Specification Sheet version 2.0*. 2004: Alberta, Canada.
3. Honeywell, *HG1700 AG17 Datasheet*. 2005: Minneapolis, MN.
4. Ford, T., et al. *OEM4 Inertial: A Tightly Integrated Decentralised Inertial/GPS Navigation System*. in *Proceedings of ION GPS '01,*. 2001. Salt Lake City, Utah.: The Institute of Navigation, Washington, D.C.
5. Ford, T., J. Neumann, and M. Bobye. *OEM4 Inertial: An Inertial/GPS Navigation System on the OEM4 Receiver*. 2001. Banff, Alberta.
6. Ford, T., J. Hamilton, and M. Bobye. *Injected Alignment for an INS System for Trackmodel Data in a Race Car Environment*. in *Proceedings of ION GPS '03*. 2003. Portland, Oregon.
7. Janet Neumann, J.Z., G. Beutler, J. Kouba. *Real-Time Carrier Phase Positioning Using the RTCM Standard Message Types 20/21 and 18/19*. in *Proceedings of ION GPS '97*. 1997. Kansas City, Missouri.
8. NovAtel, *OEM4 Family of Receivers User Manual - Vol. 2 Command and Log Reference, OM-20000047, Rev 18*. 2005: Alberta, Canada.
9. Cameron, J.T., *Vehicle Dynamic Modeling for the Prediction and Prevention of Vehicle Rollover*. 2005: The Pennsylvania State University.
10. Quanser, *Wincon: Product Information Sheet*. 2004: Ontario, Canada.

Chapter 5

Vehicle Parameter and State Estimation – Measurements and Bicycle Model Predictions

The GPS/INS sensing and data acquisition system described in the previous chapter was used to measure vehicle roll, pitch, yaw, velocity direction, velocity magnitude and position in order to verify various models. This chapter will first present methods of vehicle parameter estimation based on bicycle model theory and the results of an investigation into the bicycle models accuracy. An alternate way of estimating cornering stiffness is then presented and the new method is tested. A comparison between two cornering stiffness estimation methods is given, followed by the chapter conclusions.

5.1 Vehicle Parameter Estimation

5.1.1 Mass and Vehicle Dimensions

The 1992 Mercury Tracer used in this study has been used in previous research, [1], for which several of the vehicles parameters were estimated. Many of these parameters have been confirmed against the NHTSA database of a 1998 Tracer and therefore they will be assumed accurate for this study. In particular, easily measured parameters such as vehicle mass, length, track width and CG location will be used from the previous study. These parameters have been repeated from [1] in table **5.1**

Table 5.1: NHTSA and Measured Vehicle Parameters

Parameter	NHTSA Value	Measured Value	Deviation from NHTSA Value (%)
m (kg)	1224	1106	9.64
L (m)	2.494	2.49	0.2
a (m)	0.927	0.93	0.32
b (m)	1.567	1.56	0.51
t (m)	1.43	1.4	2.1
W_f *(N)*	N/A	6339	N/A
W_r *(N)*	N/A	3781	N/A

5.1.2 Understeer Gradient

With a more accurate sensing system in place, it was necessary to recalculate important vehicle dynamic properties such as the understeer gradient. In order to estimate the understeer gradient data was collected from several steady-state turning maneuvers. The Constant Radius Method as described in [1] and [2] was used. The methodology is repeated below.

According to the bicycle model derivation in Chapter 3, the required steering input to negotiate a steady-state turn was derived to be:

$$\delta_f = \frac{L}{R} + K_{us}\frac{U^2}{gR} \qquad 5.1$$

with

$$a_y = \frac{U^2}{gR} \qquad 5.2$$

Where a_y is the lateral acceleration in a steady-state turn. Taking the derivative of 5.1 with respect to lateral acceleration gives:

$$\frac{d}{da_y}\delta_f = \frac{d}{da_y}\left(\frac{L}{R}\right) + K_{us}\frac{d}{da_y}a_y \qquad 5.3$$

Since the turn radius is assumed to be constant and vehicle length does not change, equation 5.3 reduces to:

$$K_{us} = \frac{d\delta_f}{da_y} \qquad 5.4$$

Equation 5.4 shows that the understeer gradient is simply the slope of the plot of steering angle versus lateral acceleration.

This relationship described by equation 5.4 was used to determine the understeer gradient by measuring steering angle and lateral acceleration around a steady-state turn. These measurements were recorded while driving around a 30.5 meter radius circle at 6 different speeds in both the clockwise and counterclockwise direction. Equation 5.1 was used to determine the lateral acceleration and the steering angles were measured directly from the string potentiometers. The exact turning radius for each pass was calculated by averaging GPS data readings for each completed circle. The results were complied and a best-fit line was added to the linear region of the data. The slope of the best-fit line corresponds to the calculated understeer gradient using the bicycle model. Figure 5.1 shows the results of the 30.5m radius as well as a 36.5m radius turn. Figure 5.1

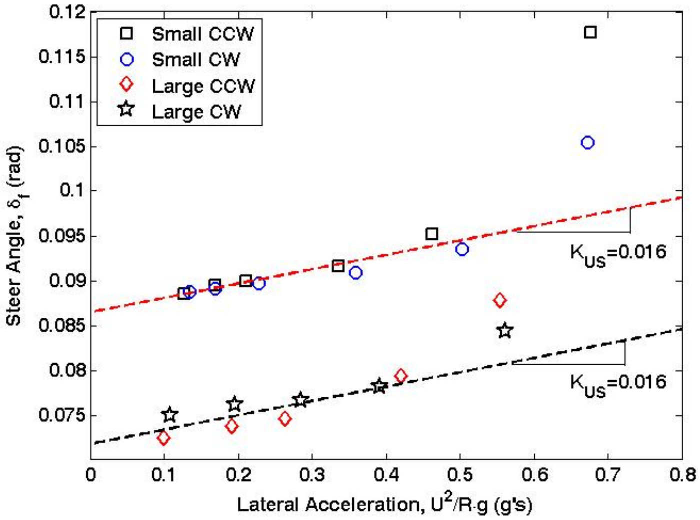

Figure 5.1: Understeer Gradient Calculation – 30.5 m Circle, Clockwise

Each of the best-fit lines has the same slope, 0.01605, regardless of the radius of the turning circle, as expected. This corresponds to the average understeer gradient. It is important to note that the understeer gradient is no longer linear at accelerations above 0.3-0.4g's, again in agreement with what others have noted in the past [3]. The exact slopes of each of the data sets (in the linear region) are presented in the table below:

Table 5.2: Understeer Gradient Calculation Results

Data Set	Kus (rad/g)
30.5 m circle	
CW	0.0125
CCW	0.0189
36.5 m Circle	
CW	0.0113
CCW	0.0215
Average	0.01605

Table Table 5.2 shows the vehicle understeer gradient value to be between 0.013 and 0.0215 rad/g. For simulation and model matching purposes, the average of the four measured understeer gradients was used ~ 0.01605 rad/g.

Another important feature of Figure 5.1 is the non-zero Y intercept of each of the best-fit lines. This steering angle, which occurs at zero lateral acceleration during a steady-state turn, is defined as the Ackerman angle. This angle is a function of vehicle length and the turn radius of the circle and is defined in [2] as:

$$\delta_{ack} = \frac{L}{R} \tag{5.5}$$

Table 5.2 summarizes the calculated and measured Ackerman Angles.

Table 5.3: Calculated and Best Fit Ackerman Angles

	Calculated Ackerman (deg)	Best-fit Ackerman (deg)	Error (deg)
Small Circles	4.58	4.95	0.37
Large Circles	3.75	4.11	0.36

The over-predicted Ackerman angle as presented in Table 5.2 suggests a constant steering offset error. This error can be applied as a correction later if necessary.

5.1.3 Cornering Stiffness Estimation

Throughout the course of this work, several methods were used in order to accurately determine the front and rear cornering stiffness values. An initial estimate of cornering stiffness was made by using the understeer gradient derived above. By using the bicycle model formulation an expression can be derived to relate the understeer gradient to the rear cornering stiffness. This derivation is presented below:

As a vehicle negotiates a steady-state turn, its total velocity vector at the center of gravity is offset from the vehicle's longitudinal axis by an angle known as the sideslip angle – β. As a vehicle's speed increases, the sideslip angle moves from a positive angle to a negative angle. In Figure 5.2 a vehicle in a high speed turn is shown:

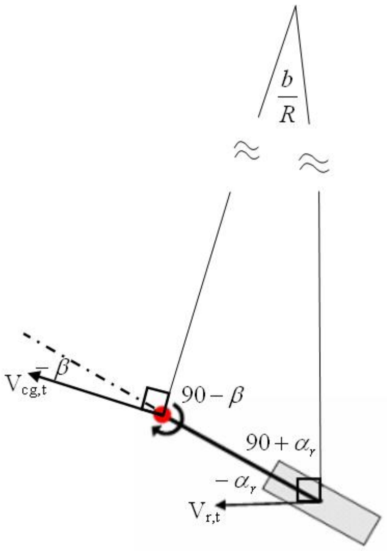

Figure 5.2: Bicycle Model SS Turn – Sideslip View

By summing the interior angles of the triangle, an expression for sideslip in a steady-state turn can be written:

$$\beta = \frac{b}{R} + \alpha_r \qquad \textbf{5.6}$$

The expression for rear slip angle derived in equation **3.8** can be substituted into equation **5.6**:

$$\beta = \frac{1}{R} \cdot \left(b + \frac{W_r U^2}{C_{\alpha r} g} \right) \qquad \textbf{5.7}$$

At the speed at which a vehicle's sideslip angle transitions from positive (low speed) to negative (high speed), the above equation can be solved for rear cornering stiffness:

$$C_{\alpha r} = -\frac{W_r U^2}{gb} \qquad \textbf{5.8}$$

Where the sideslip angle was set equal to zero and the cornering stiffness value is a negative quantity with units N/rad.

By definition, sideslip is the angle between the direction of velocity and vehicle body. Therefore, by measuring velocity direction and yaw angle, the current sensing system can directly measure sideslip by:

$$\beta = VelocityDirection - Yaw \qquad \textbf{5.9}$$

By measuring sideslip and velocity and using the measurements in equation **5.8**, the rear cornering stiffness can be determined experimentally. To do this, the Tracer was put into a steady-state turning maneuver and vehicle's speed was *slowly* increased in an attempt to keep approximate steady-state behavior. The speed continued to increase until the sideslip changed signs to a negative value. The data was then post-processed to determine the speed at which the zero-crossing occurred. Figure **5.3** shows the plot of sideslip versus time as vehicle speed was increased:

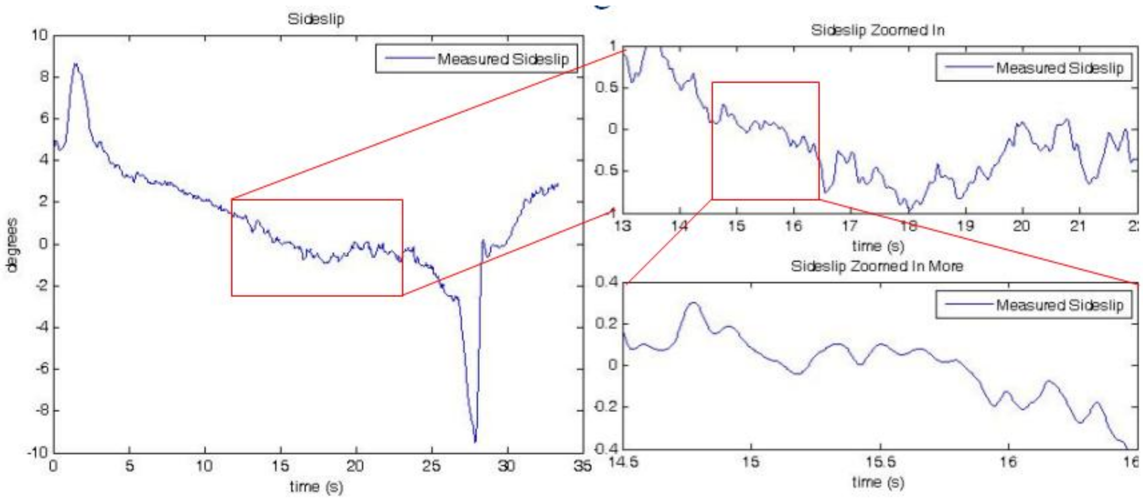

Figure 5.3: Sideslip Measurements – Cornering Stiffness Estimation

Since there is a timeframe where the sideslip measurements were approximately zero, the average velocity during that timeframe was used as the zero sideslip velocity. This procedure was repeated for three data collection sets where the same experiment was performed. The average zero sideslip velocity was determined to be 14.12 m/s.

The measured zero sideslip velocity, vehicle weight on the rear axle and dimension *b* were used in conjunction with Equation 5.8 to determine the rear cornering stiffness value.

$$C_{\alpha r} = -\frac{3781N}{1.56m \cdot 9.81\frac{m}{s}} \cdot \left(14.12\frac{m}{s}\right)^2 = -49258\frac{N}{rad} \qquad 5.10$$

The understeer gradient from equation 3.24 was used to determine the front cornering stiffness:

$$C_{\alpha f} = \frac{W_f C_{\alpha r}}{W_r - C_{\alpha r} K_{us}} = -68338\frac{N}{rad} \qquad 5.11$$

The table below shows a summary of values to be used in the bicycle model simulations:

Table 5.4: Bicycle Model Parameters

Parameter	Value
m (kg)	1106
a (m)	0.93
b (m)	1.56
Cαf (N/rad)	-68338
Cαr (N/rad)	-49258

5.2 Bicycle Model Simulation Results

In simulation, the parameters presented in table 5.4 were used in the state space representation of the Bicycle Model given in equation 3.14. The model's ability to predict lateral velocity and yawrate was investigated in both the time and frequency domain. In the time domain steady-state circles and chirp response maneuvers were used. The inputs to the state space model were the vehicle velocity and steering angle. The results are presented in subsections below:

5.2.1 Chirp Response

A frequency sweeping sinusoidal steering input, or chirp input, was given to the tracer at various speeds to investigate the bicycle model's accuracy in predicting lateral velocity and yawrate. This type of input is helpful in examining model accuracy in the time domain and also gives insight into the frequency domain. The frequency of the input was varied from 0.15 Hz to the fastest frequency the driver could input – approximately 4 Hz.

Figure 5.4 shows the predicted and measured yawrate while Figure 5.5 displays the lateral velocity measurements and predictions.

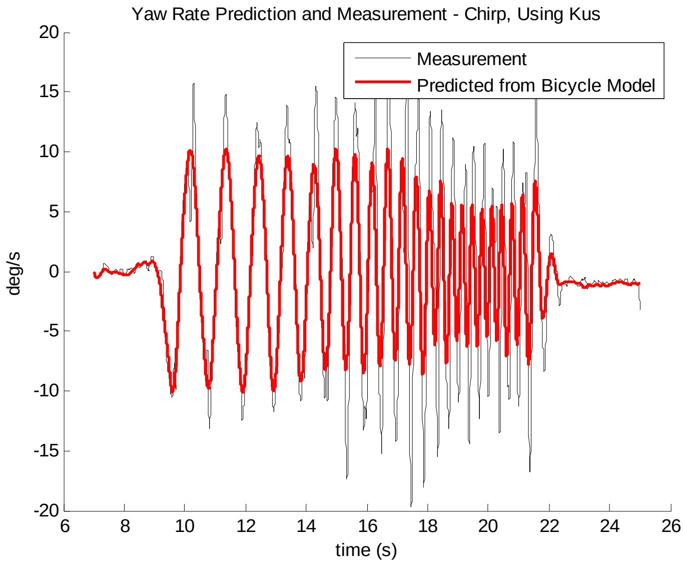

Figure 5.4: Yawrate Chirp Response – Kus Method

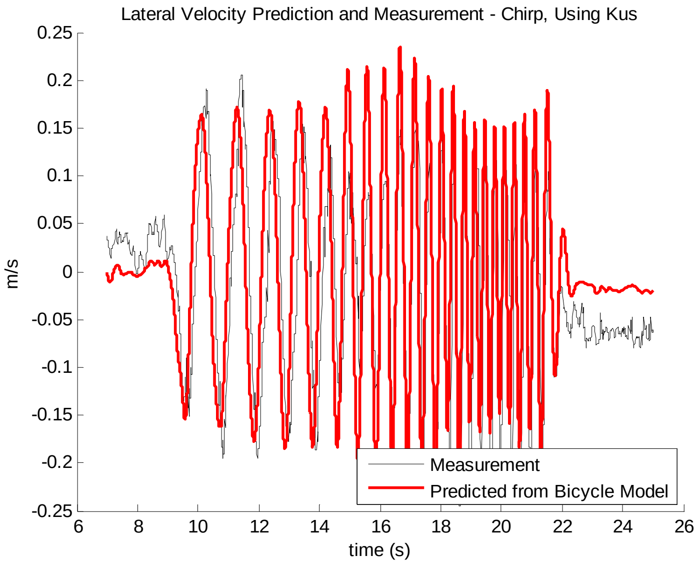

Figure 5.5: Lateral Velocity Chirp Response – Kus Method

Investigation of these plots shows some interesting results. With the current model parameters, the bicycle model predicts yawrate well for low frequencies; however it is unable to match at higher frequencies. Figure 5.5 clearly shows a disagreement of phase in the low frequencies for lateral velocity, and poor matching in both phase and amplitude at high frequencies.

5.2.2 Steady-State Circles

The bicycle model was then used to fit steady-state circle data at 25 miles per hour. The results are below:

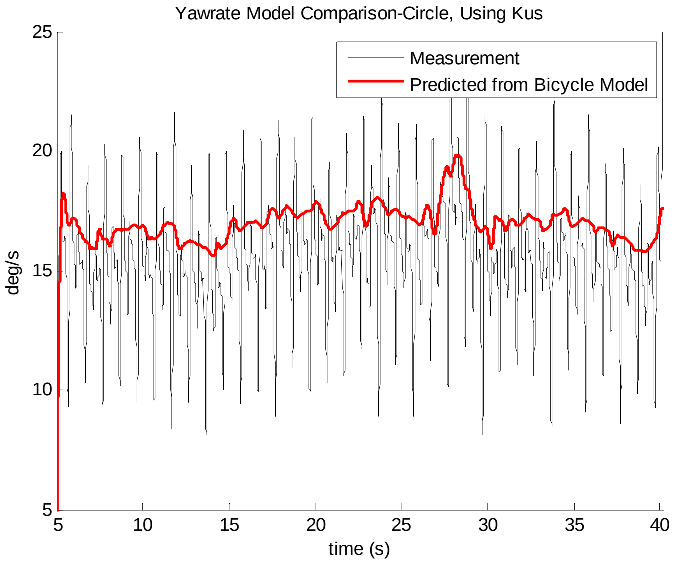

Figure 5.6: Yawrate Steady-State Circle Response – Kus Method

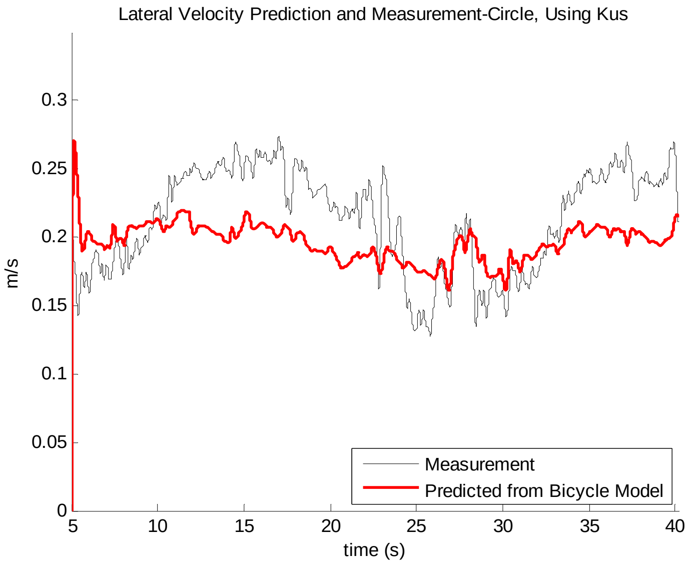

Figure 5.7: Lateral Velocity Steady-State Circle Response – Kus Method

Once again there is poor model matching for both yawrate and lateral velocity. Both model predictions are offset from the measured value and show some disagreement in transient regions. As with the chirp response, the yawrate shows better matching than lateral velocity.

5.2.3 Frequency Response

A frequency response routine was successfully developed and implemented in [1], and a similar procedure was followed here. Fifteen evenly spaced (on logarithmic scale) frequencies of sinusoidal steering inputs were given to the vehicle ranging from 0.15 Hz to 3.5 Hz. The steering inputs were synchronized with a digital metronome and their magnitudes were managed by using witness marks on the steering wheel. These inputs were given at two different amplitudes at a speed of 25mph.

Since it is impossible for a drivers input to exactly match the metronome (especially at high frequencies), a non linear fitting routine was used to extract the input magnitude and phase during post processing. As in [1], the routine consisted of minimizing the sum-of-squares error between the steering input data and a best-fit sine wave. The same procedure was performed on the output data (yawrate and lateral velocity), but the frequency of the best-fit sine wave was fixed at the input frequency. The input and output amplitudes and frequencies were used to determine the frequency responses for both yawrate and lateral velocity. It is important to note that the current sensor suite allows the frequency response to be performed on lateral velocity and yawrate which allow for a direct comparison to the bicycle model. This is a considerable improvement over the yawrate and lateral acceleration states used in [1].

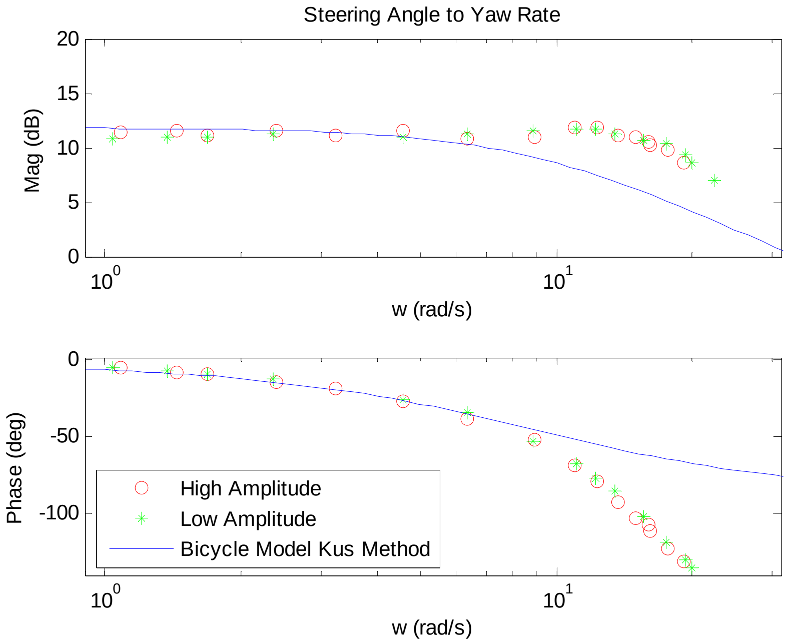

Figure 5.8: Yawrate Frequency Response – Kus Method

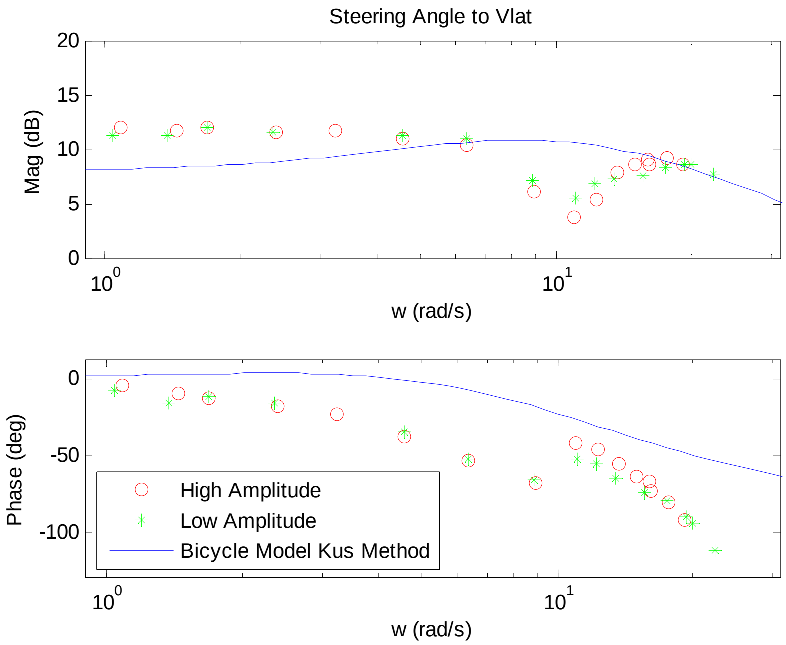

Figure 5.9: Lateral Velocity Frequency Response – Kus Method

Yet again, the bicycle model shows better matches to the yawrate data than the lateral velocity data. The yawrate prediction matches very well for both magnitude and phase for frequencies lower than 10 rad/s. However, the lateral velocity magnitude and phase plots do not match at all. This will be further discussed in the next section.

5.2.4 Bicycle Model Results Discussion

In the previous three sections, the bicycle model's accuracy was investigated in various situations. The overall poor data fits for each time domain maneuver, and the poor match in the frequency domain both suggests an error in the mode, the model parameters, or both. An initial comparison between cornering stiffness values determined in section 5.1, and those used other works [1],[4],[5], suggest that although the numbers used here are reasonable, they may be lower than the actual value.

Further investigation into the cornering stiffness method used in section 5.1 uncovered some interesting issues. This method is highly dependent on the understeer gradient determined in section 5.1.2 and although this value was the average of four data sets, the initial assumption of steady-state was violated. At the current testing facility, the skid pad used for both the understeer gradient calculation and zero sidelslip velocity measurement is not perfectly level. In fact, the elevation of varies 0.84 meters while traveling around the circle. This super-elevation leads to constant acceleration/deceleration of the vehicle in both the lateral and longitudinal directions as it travels around the path. These accelerations invalidate the steady-state assumption. Although this superelevation may seem small, it plays a large effect in the understeer gradient value which is only on the order of 10^{-2}. By simply increasing the magnitude of the cornering stiffness values an improvement can be seen in all of the plots presented in section 5.1. Because of this, an alternative method of determining cornering stiffness was developed.

5.3 Bicycle Model – Cornering Stiffness Correction

As demonstrated in [1], the effect of cornering stiffness variation can most easily be seen in the frequency domain. The figures presented in section 5.2.3 clearly show that the bicycle model with the current parameter values mismatches the data at nearly all frequencies. At the vehicles natural frequency and above, higher order dynamics which are not modeled by the planar bicycle model such as tire lag, roll and camber effects, will greatly affect the model matching. However at low frequencies, in particular at steady-state when higher-order model effects can be neglected, the bicycle model still does not match the data. In order to force a match at low frequencies, the bicycle model DC gain equations were investigated. The DC gain of the model was forced to match that of the data and this relationship was used to calculate front and rear cornering stiffness values which would be necessary for such a match. The frequency response method is particularly useful because the inherent averaging of the response tends to eliminate the undesired effects of super elevation and non-steady-state behavior. The DC gain method of determining cornering stiffness values is presented in the following sections.

5.3.1 Bicycle Model DC Gain Derivations

The bicycle model can be represented in standard state space form:

$$\dot{X} = AX + BU \tag*{5.12}$$

$$Y = CX + DU \tag*{5.13}$$

Where equation 5.12 was presented for the bicycle model previously in Chapter 3 as equation 3.14. Equation 5.13 will vary depending on which state (lateral velocity or yawrate) is desired as an output.

By presenting the bicycle model in state space form, the DC gain equations for yawrate or lateral velocity are easily written by:

$$G = D - CA^{-1}B \tag*{5.14}$$

The lateral velocity DC gain is computed with the A and B matrices presented in equation equation 3.14 and the following C and D matrices:

$$\begin{aligned} \mathrm{C} &= \begin{bmatrix} 1 & 0 \end{bmatrix} \\ D &= 0 \end{aligned} \tag*{5.15}$$

The lateral velocity DC gain is then directly written:

$$G_V = \frac{U \cdot \left((C_{\alpha f} C_{\alpha r}) \cdot (b^2 + ab) + C_{\alpha f}(a \cdot m \cdot U^2) \right)}{C_{\alpha f} C_{\alpha r} \cdot (b^2 + a^2 + 2ab) + m \cdot U^2 (C_{\alpha f} a - C_{\alpha r} b)} = \left. \frac{V}{\delta_f} \right|_{SteadyState} \tag*{5.16}$$

The same procedure follows for yawrate:

$$\mathrm{C} = \begin{bmatrix} 0 & 1 \end{bmatrix} \qquad \textbf{5.17}$$
$$D = 0$$

$$G_r = \frac{U \cdot (C_{\alpha f} C_{\alpha r}) \cdot (b + a)}{C_{\alpha f} C_{\alpha r} \cdot (b^2 + a^2 + 2ab) + m \cdot U^2 (C_{\alpha f} a - C_{\alpha r} b)} = \left. \frac{r}{\delta_f} \right|_{SteadyState} \qquad \textbf{5.18}$$

The lateral velocity and yawrate DC gain equations represent two equations, with four unknowns – G_v, G_r, $C_{\alpha f}$ and $C_{\alpha r}$. However by forcing the DC gains to be equal to the measured DC gains, the system of equations becomes solvable with only two equations and two unknowns.

5.3.2 Alternate DC Gain Derivation

Since the DC gain derived above is simply the ratio of lateral velocity or yawrate to steering input at steady-state, its validity was checked by computing this exact ratio from the bicycle model equations directly. The derivation is as follows:

The steady-state steering angle for a vehicle in a turn was shown in equations **3.15** and **3.20** to be:

$$\delta_f = \frac{L}{R} - \frac{1}{C_{\alpha f}} \left(\frac{b}{L} \cdot \frac{mU^2}{R} \right) + \frac{1}{C_{\alpha r}} \left(\frac{a}{L} \cdot \frac{mU^2}{R} \right) \qquad \textbf{5.19}$$

For a large radius turn, the steady-state yawrate can be expressed as:

$$r = \frac{U}{R} \qquad \textbf{5.20}$$

Therefore the yawrate DC gain should be the ratio of these two steady-state equations:

$$\left. \frac{r}{\delta_f} \right|_{ss} = \frac{\dfrac{U}{R}}{\dfrac{L}{R} - \dfrac{1}{C_{\alpha f}} \left(\dfrac{b}{L} \cdot \dfrac{mU^2}{R} \right) + \dfrac{1}{C_{\alpha r}} \left(\dfrac{a}{L} \cdot \dfrac{mU^2}{R} \right)} = G_r \qquad \textbf{5.21}$$

A similar expression can be derived for lateral velocity. This is most easily done by looking at the sideslip angle. As described in equation 5.6 the sideslip angle seen in a steady-state turn can be written:

$$\beta = \frac{b}{R} + \alpha_r \qquad 5.22$$

By definition this is the angle between the velocity vector and the vehicles heading. Therefore the total velocity vector can be broken down into it longitudinal and lateral components by looking at the velocity triangle as shown in Figure 5.10:

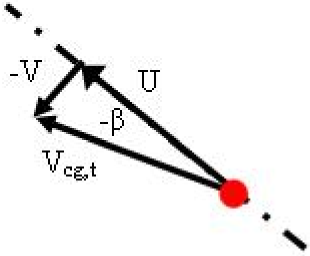

Figure 5.10: Sideslip Vector

$$\begin{aligned} U &= V_{total,cg}\cos(-\beta) \cong V_{total,cg} \\ -V &= V_{total,cg}\sin(-\beta) \cong -V_{total,cg}\beta \cong -U\cdot\beta \end{aligned} \qquad 5.23$$

Where the lateral velocity is shown in the negative direction in Figure 5.10 in accordance with the SAE sign convention. Equation 5.23 can be used with equation 5.22 to solve for the steady-state lateral velocity:

$$V = U\cdot\left(\frac{b}{R} + \alpha_r\right) \qquad 5.24$$

The lateral velocity DC gain can then be written:

$$\left.\frac{V}{\delta_f}\right|_{ss} = \frac{U\cdot\left(\frac{b}{R} + \alpha_r\right)}{\frac{L}{R} - \frac{1}{C_{\alpha f}}\left(\frac{b}{L}\cdot\frac{mU^2}{R}\right) + \frac{1}{C_{\alpha r}}\left(\frac{a}{L}\cdot\frac{mU^2}{R}\right)} = G_V \qquad 5.25$$

Equations 5.21 and 5.25 can be rearranged to check their equivalence to equations 5.18 and 5.16**.**

First, Equations 3.21 and 3.22 can be substituted for α_r in Equation 5.25:

$$G_V = \frac{U \cdot \left(\frac{b}{R} + \frac{m \cdot g \cdot a}{L \cdot C_{\alpha r}} \cdot \frac{U^2}{gR} \right)}{\frac{L}{R} - \frac{1}{C_{\alpha f}} \left(\frac{b}{L} \cdot \frac{mU^2}{R} \right) + \frac{1}{C_{\alpha r}} \left(\frac{a}{L} \cdot \frac{mU^2}{R} \right)} \qquad \textbf{5.26}$$

Next, L can be replaced by the sum of a and b and the Equation 5.25 can be multiplied by:

$$\frac{C_{\alpha f} C_{ar} (a+b)}{C_{\alpha f} C_{ar} (a+b)} \qquad \textbf{5.27}$$

After simplification:

$$G_V = \frac{U \cdot \left(\frac{b \cdot (a+b)^2 \cdot C_{\alpha r}{}^2 C_{af} \cdot g + a \cdot (a+b) \cdot mgU^2 \cdot C_{\alpha r} C_{af}}{(a+b) \cdot C_{\alpha r} g} \right)}{C_{\alpha r} C_{af} \cdot (a+b)^2 - C_{\alpha r} mU^2 b + C_{\alpha f} mU^2 a} \qquad \textbf{5.28}$$

Which can be further simplified to the expression obtained in section 5.3.1:

$$G_V = \frac{U \cdot \left((C_{\alpha f} C_{\alpha r}) \cdot (b^2 + ab) + C_{\alpha f} (a \cdot m \cdot U^2) \right)}{C_{\alpha f} C_{\alpha r} \cdot (b^2 + a^2 + 2ab) + m \cdot U^2 (C_{\alpha f} a - C_{\alpha r} b)} \qquad \textbf{5.29}$$

A similar procedure can be followed to show the equivalence of Equations 5.18 and 5.21. This will not be presented here.

5.3.3 Cornering Stiffness Values from DC Gains

In order to accurately model the DC gains and to confirm linearity of the system, a frequency response was performed for two different magnitudes of steering input. The system magnitude corresponding to the lowest frequency steering input, 0.15 Hz, was assumed to be the DC gain of the system. The frequency response plots for lateral velocity and yawrate are shown below in Figures 5.11 and 5.12.

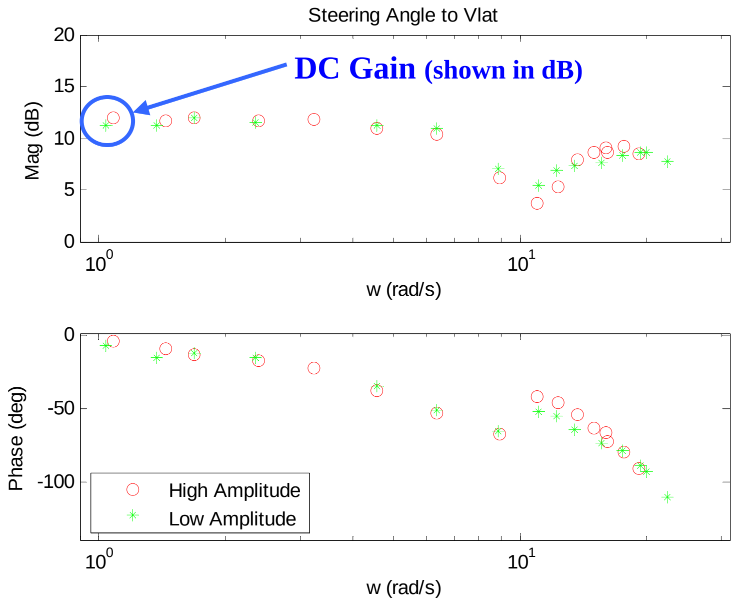

Figure 5.11: Lateral Velocity Frequency Response – DC Gain

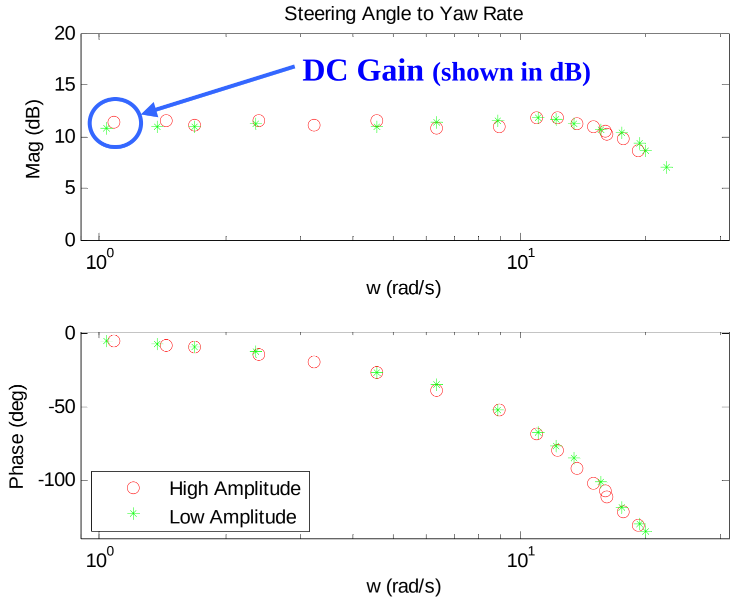

Figure 5.12: Yawrate Frequency Response – DC Gain

Since the DC gain varied for the low amplitude and high amplitude frequency responses, the values were averaged. Table 5.5 below summarizes the measured results:

Table 5.5: Measured DC Gains

Gain	Average Value
Gr	3.599 (rad/s)/rad
Gv	3.804 (m/s)/rad

The DC gain value for yawrate, *Gr*, shows that for one radian of steady-state steering input, vehicle's yawrate will be 3.599 rad/s. Similarly, *Gv* shows that for one radian of steady-state steering input, the vehicles lateral velocity will be 3.804 m/s. With the DC gains measured, equations 5.16 and 5.18 can be rearranged to solve for rear and front cornering stiffness values respectively:

$$C_{\alpha r} = \frac{(a \cdot m \cdot U^2 \cdot G_r)}{(G_v - b \cdot G_r) \cdot (a+b)} = \text{-89,411}\,\frac{\mathrm{N}}{\mathrm{rad}} \tag{5.30}$$

$$C_{\alpha f} = \frac{(-U^2 \cdot m \cdot G_r C_{\alpha r} b)}{(C_{\alpha r} U \cdot (a+b) - G_r C_{\alpha r} \cdot (a+b)^2 - U^2 m G_r a)} = \text{-82,450}\,\frac{\mathrm{N}}{\mathrm{rad}} \tag{5.31}$$

As expected, these values are significantly different than those obtained using the understeer gradient method. One should note that not only are the magnitudes of each cornering stiffness value different, but also that the rear cornering stiffness is now higher in magnitude than the front cornering stiffness. Using equation 3.24 with the cornering stiffness values solved for using the DC gain method, the understeer gradient can be solved to be:

$$K_{us} = 0.0345\frac{rad}{g} \tag{5.32}$$

This value is the same order of magnitude that calculated from the steady-state turning maneuvers; however it results in very different cornering stiffness values.

The effect of these new cornering stiffness values on the model matching is investigated in the next section.

5.4 Bicycle Model – Cornering Stiffness Correction Simulation Results

The time and frequency domain simulations were completed again with the only change being the cornering stiffness values. The results are plotted in the next three sections, and a discussion of the results is presented afterwards:

5.4.1 Chirp Response

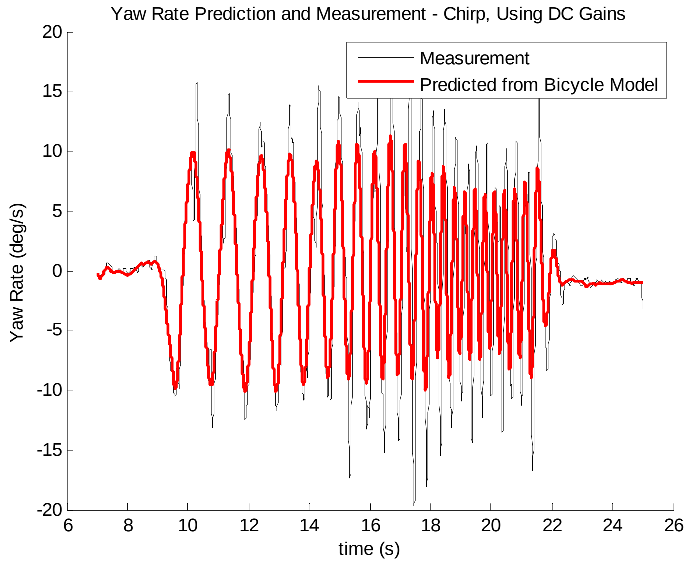

Figure 5.13: Yawrate Chirp Response – DC Gain Method

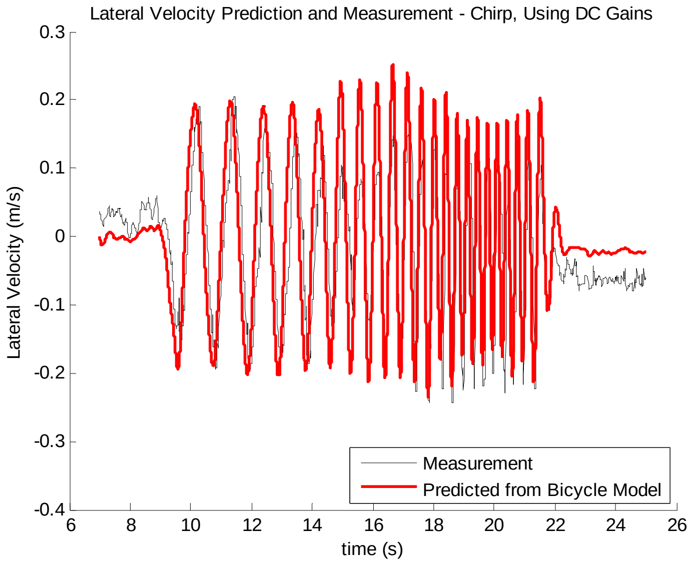

Figure 5.14: Lateral Velocity Chirp Response – DC Gain Method

5.4.2 Steady-state Circles

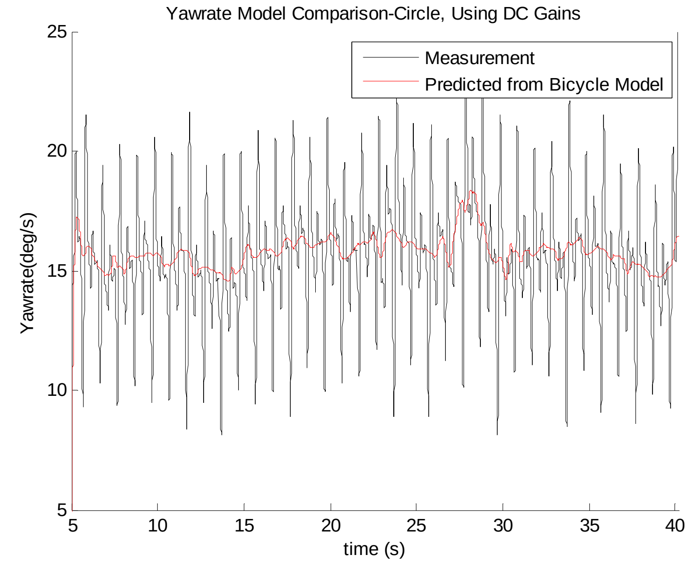

Figure 5.15: Yawrate Steady-State Circle Response – DC Gain Method

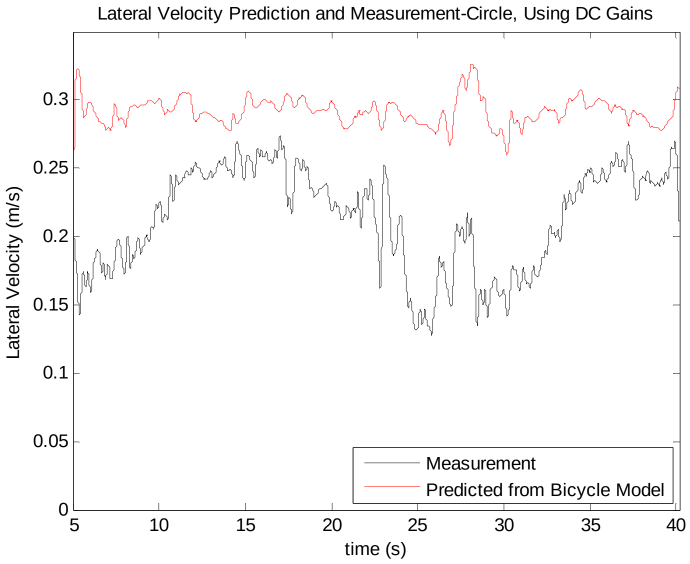

Figure 5.16: Lateral Velocity Steady-State Circle Response – DC Gain Method

5.4.3 Frequency Response

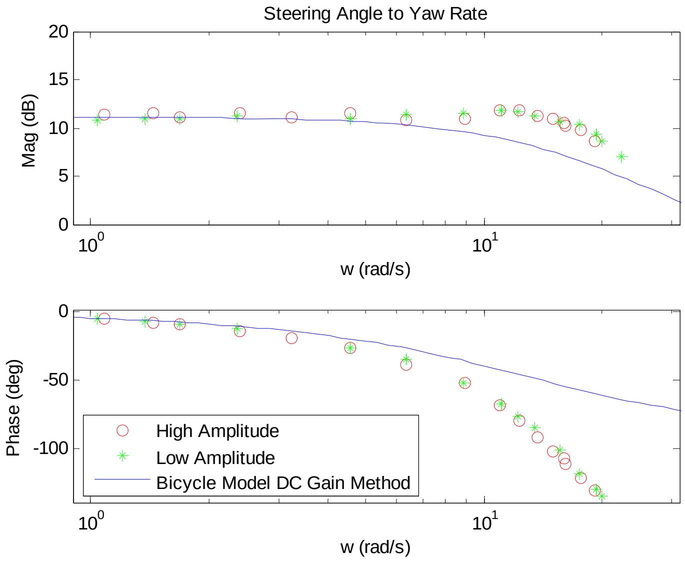

Figure 5.17: Yawrate Frequency Response – DC Gain Method

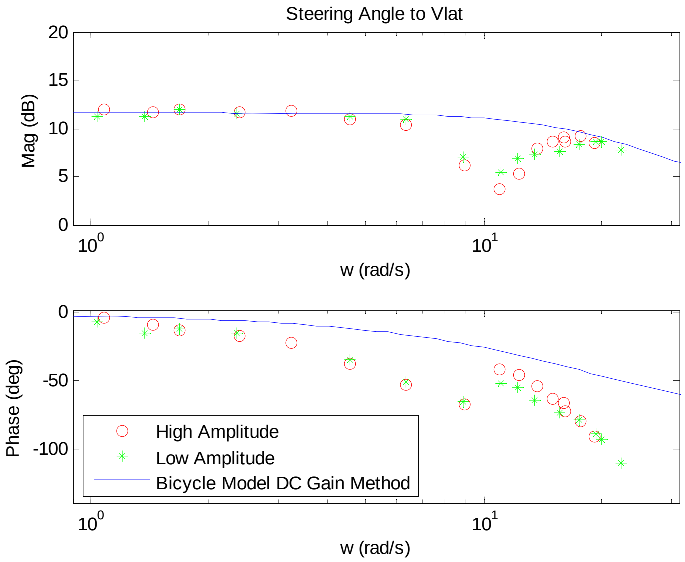

Figure 5.18: Lateral Velocity Frequency Response – DC Gain Method

5.4.4 Bicycle Model – Cornering Stiffness Correction Results Discussion

A comparison between the results presented in section 5.4 with those in section 5.2 shows a drastic improvement in the model matching for both yawrate and lateral velocity in the time and frequency domains when using the DC gain method to determine cornering stiffness values. Comments on each comparison are presented in this section

5.4.4.1 Chirp Response

When comparing the chirp response data, it is interesting to note that although yawrate matches improved with the DC gain method, the change is subtle compared that of the lateral velocity matches. This is especially apparent in the low frequency steering input portion of the chirp response. Below is a direct comparison between the two methods:

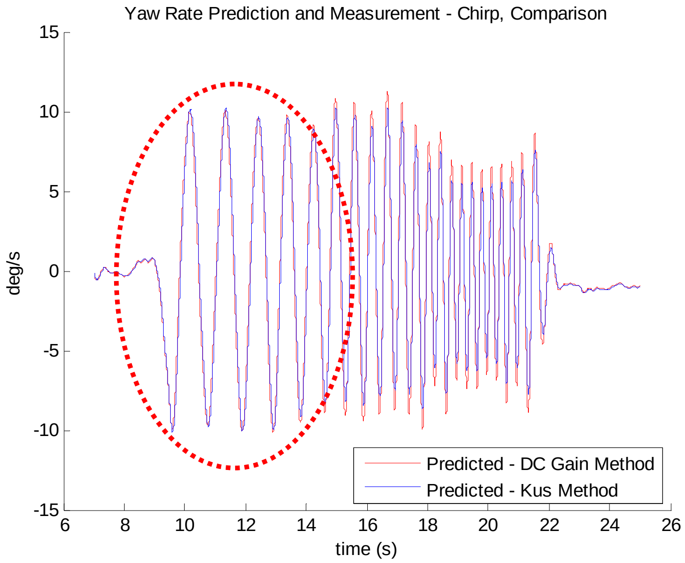

Figure 5.19: Yawrate Chirp Response – Method Comparison

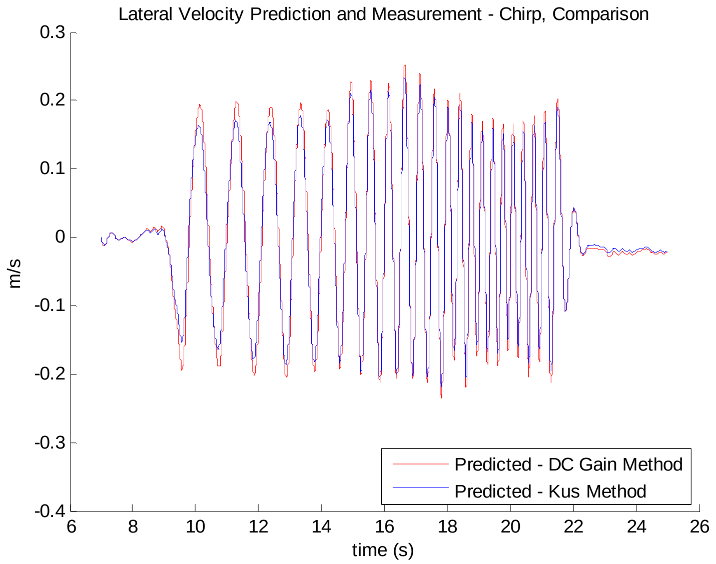

Figure 5.20: Lateral Velocity Chirp Response – Method Comparison

The circled area of Figure 5.19 suggests that time domain yawrate plots consisting of low frequency steering inputs should not be used to fine tune cornering stiffness values as the results of cornering stiffness variation cannot be seen. This is an interesting result that may not be apparent upon inspection of the model's equations.

5.4.4.2 Steady-state Circles

By comparing Figure 5.7 with Figure 5.16, the understeer gradient method presented in section 5.2 may seem better than the DC gain method when matching the lateral velocity measurements for the steady-state circle data. However by looking at the transient portions of the plots, one can see that the DC gain method more accurately represents the dynamics of the vehicle – even though it is offset by a constant value. The accurate match for low frequencies of the frequency response and chirp response data, and poor match for the steady-state circle maneuver suggests that there is a significant tire force generation mechanism that is dependent on whether or not the vehicle is in a steady turn. A possible explanation for this is that the tire model may be dependent on the vehicle roll angle – which is significantly greater in a steady-state turn than during low frequency sinusoidal steering inputs. The effects of roll angle and tire camber will be investigated later in chapter 7.

5.4.4.3 Frequency Response

By using the DC gain method, the bicycle model was forced to match yawrate and lateral velocity plots in the low frequency region of the frequency response. As expected both lateral velocity and yawrate frequency response magnitudes are now accurate at low frequencies. However, at frequencies of 6 rad/s and above the bicycle model is not able to accurately predict these states. Also, the frequency response phases contradict the data for both lateral velocity and yawrate for these frequencies. This mismatch is partially the result of tire lag, which will be introduced in chapter 6.

5.5 Conclusions

- The DC gain method should be used to determine front and rear cornering stiffness values
- Lateral velocity is more strongly coupled to cornering stiffness values than is yawrate
- Time domain yawrate plots are ill-suited to show the effects of varying cornering stiffness variation
- Model mismatch for steady-state circles using DC gain method must be investigated further
- High frequency dynamics and phase mismatch as seen in the frequency response plots should be examined in detail

1. Cameron, J.T., *Vehicle Dynamic Modeling for the Prediction and Prevention of Vehicle Rollover*. 2005: The Pennsylvania State University.
2. Gillespie, T.D., *Fundamentals of Vehicle Dynamics*. 1992: Society of Automotive Engineers (SAE). 495.
3. Mitschke, M., *Dynamik der Kraftfahrzeuge*. Vol. A, B, C. 1995, Berlin: Springer Verlag.
4. Bevly, D.M., R. Sheridan, and J.C. Gerdes. *Integrating INS Sensors with GPS Velocity Measurements for Continuous Estimation of Vehicle Sideslip and Tire Cornering Stiffness*. in *Proceedings of the 2001 American Control Conference*. 2001. Arlington, Virginia.
5. Borner, M., et al. *Detection of Lateral Vehicle Driving Conditions Based on the Characteristic Velocity*. in *Proceedings of the 15th Triennial World Congress of the Internation Federation of Automatic Control (IFAC)*. 2002. Ann Arbor, Michigan.

Chapter 6

Bicycle Model – Tire Lag

This chapter further investigates the high frequency mismatch of the bicycle model presented in chapter 5. It is known that there is a time lag between a sudden change in slip angles of a pneumatic tire and the build up of lateral force. This has been modeled through the use of the concept of a relaxation length, σ [1]. The relaxation length concept assumes that the force generated by a tire gradually approaches its steady state value as a first-order differential equation. In the sections to follow, the bicycle model is re-derived to incorporate tire lag due to the tire's relaxation length. The model is then simulated in the time and frequency domain to investigate its validity.

6.1 Bicycle Model with Tire Lag Derivation

The tire lag model is often represented as a first order system with zero DC gain [2].
In previous work [3], a first-order tire lag model was introduced only on the front steering input. After consultation with the authors of [4] and reviewing [5],[6], the following model of tire lag was used which considers tire lag as a function of tire slip on the front and rear tires.

The fundamental bicycle model equations as written in chapter 3 do not change:

$$m \cdot a_y = \sum F_y = F_f \cos(\delta) + F_r \cong F_f + F_r$$

$$I_{zz} \cdot \frac{dr}{dt} = \sum M_z = F_f \cos(\delta) \cdot a - F_r \cdot b \cong F_f \cdot a - F_r \cdot b \qquad \textbf{6.1}$$

Referring back to chapter 3, equation **3.11** can be combined with equation **6.1**:

$$\begin{aligned}\frac{dV}{dt} &= \left(\frac{1}{m}\right)\cdot F_f + \left(\frac{1}{m}\right)\cdot F_r - U\cdot r \\ \frac{dr}{dt} &= \left(\frac{a}{I_{zz}}\right)\cdot F_f + \left(-\frac{b}{I_{zz}}\right)\cdot F_r\end{aligned} \tag{6.2}$$

The lateral tire forces, F$_f$ and F$_r$ must be modeled differently in this derivation to incorporate tire lag. The force generated by the tire can be modeled as a first order differential equation increase to its steady state value. Therefore the force as a function of time can be written as:

$$F(t) = F_{ss}(1 - e^{\frac{-Ut}{\sigma}}) \tag{6.3}$$

Where F_{ss} is the force the tire will generate at steady state and σ is the tire's relaxation length.

Karnopp, [6], describes the differential equation relating the force generated by the tires, F, and the steady state force, $F_{ss,}$ based on the time behavior in equation 6.3 as:

$$F = F_{ss} - \left(\frac{\sigma}{U}\right)\cdot\frac{dF}{dt} \tag{6.4}$$

Also, the steady state force, F_{ss} has been described previously as:

$$\begin{aligned}F_{f,ss} &= C_{\alpha f}\alpha_{f,ss} = C_{\alpha f}\cdot\left(\frac{V + a\cdot r}{U} - \delta_f\right) \\ F_{r,ss} &= C_{\alpha r}\alpha_{r,ss} = C_{\alpha r}\cdot\left(\frac{V - b\cdot r}{U}\right)\end{aligned} \tag{6.5}$$

Combining equations 6.4 with 6.5 and rearranging for the time rate of change of the force generated:

$$\begin{aligned}\frac{dF_f}{dt} &= \frac{U}{\sigma_f}\cdot\left(\left(C_{\alpha f}\cdot\left(\frac{V + a\cdot r}{U} - \delta_f\right)\right) - F_f\right) \\ \frac{dF_f}{dt} &= \frac{U}{\sigma_f}\cdot\left(\left(C_{\alpha r}\cdot\left(\frac{V - b\cdot r}{U}\right)\right) - F_r\right)\end{aligned} \tag{6.6}$$

Where the front and rear tire relaxation lengths have been assumed to be the same and there is no rear steering input. Equation 6.6 can be further rearranged:

$$\begin{aligned}\frac{dF_f}{dt} &= \left(\frac{C_{\alpha f}}{\sigma}\right)\cdot V + \left(\frac{C_{\alpha f}a}{\sigma}\right)\cdot r + \left(-\frac{U}{\sigma}\right)\cdot F_f + \left(-\frac{C_{\alpha f}U}{\sigma}\right)\cdot \delta_f \\ \frac{dF_r}{dt} &= \left(\frac{C_{\alpha r}}{\sigma}\right)\cdot V + \left(-\frac{C_{\alpha r}b}{\sigma}\right)\cdot r + \left(-\frac{U}{\sigma}\right)\cdot F_r\end{aligned} \qquad 6.7$$

The model can be written in state space representation with the states being lateral velocity, yaw rate and the forces generated by the front and rear tires. This representation comes directly from equations 6.2 and 6.7:

$$\begin{bmatrix}\frac{dV}{dt} \\ \frac{dr}{dt} \\ \frac{dF_f}{dt} \\ \frac{dF_r}{dt}\end{bmatrix} = \begin{bmatrix} 0 & -U & \left(\frac{1}{m}\right) & \left(\frac{1}{m}\right) \\ 0 & 0 & \left(\frac{a}{I_{zz}}\right) & \left(-\frac{b}{I_{zz}}\right) \\ \left(\frac{C_{\alpha f}}{\sigma}\right) & \left(\frac{C_{\alpha f}a}{\sigma}\right) & \left(-\frac{U}{\sigma}\right) & 0 \\ \left(\frac{C_{\alpha r}}{\sigma}\right) & \left(-\frac{C_{\alpha r}b}{\sigma}\right) & 0 & \left(-\frac{U}{\sigma}\right)\end{bmatrix} \cdot \begin{bmatrix} V \\ r \\ F_f \\ F_r\end{bmatrix} + \begin{bmatrix} 0 \\ 0 \\ \left(-\frac{C_{\alpha f}U}{\sigma}\right) \\ 0\end{bmatrix} \cdot \delta_f \qquad 6.8$$

6.2 Tire Lag Model – Simulation Results

The time and frequency domain simulations performed in chapter 3 were repeated here for the new model which includes tire lag. Using the results from chapter 5, the cornering stiffness values obtained from the DC gain method were used in these simulations. With the cornering stiffness values solved for, the A matrix of the state space representation of equation 6.8 still has one unknown – σ, the tire relaxation lengths. In order to determine the value of the relaxation lengths, parametric variation was performed in the frequency domain. This method is similar to that performed in [3] for cornering stiffness variation. Because of this, parametric variation procedure, the frequency response results will be discussed first.

6.2.1 Frequency Response

In order to determine the tire relaxation length, the tire lag model was simulated with increasing values of σ, from 0.4 to 1.6 m in 0.15m increments, and the resulting plots were investigated in the frequency domain. The figure below shows the effect of tire lag for yawrate:

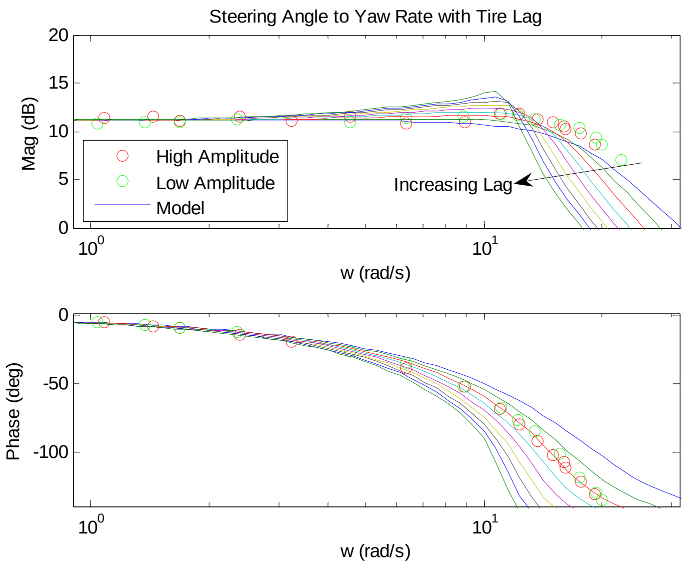

Figure 6.1: Yawrate – Frequency Response Varying Relaxation Length

It is interesting to note that the value of relaxation length which matches best in the magnitude plot does not correspond to the best match in the phase plot. Phase matches at higher values of lag than magnitude does.

In order to reconcile the differences between the two sigma values, the front and rear relaxation lengths were assumed to be independent of each other. The parametric variation was repeated with different values of front and rear relaxation lengths. After the simulations were complete, it was apparent that the rear relaxation length is primarily responsible for the higher-order dynamics found in the magnitude plot. However, by making the two values independent, the model matching routine becomes more complex. Also, the differences between the independent relaxation length model and the model which treats the relaxation length as one parameter were minor. Because of this, it will be assumed that the relaxation lengths are identical, and the model presented in this section will be used in the analysis.

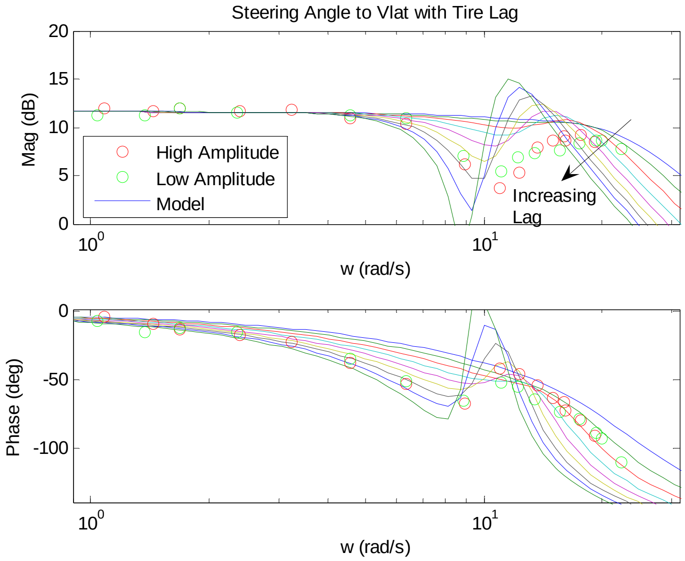

Figure 6.2: Lateral Velocity – Frequency Response Varying Relaxation Length

Figures 6.1 and 6.2 clearly show the effects of tire lag; most notably on high frequency inputs. The tire lag model captures some of the higher-order dynamics present at frequencies around 10 rad/s. After the above parametric variation, the value of the relaxation length which created the best match was extracted. However, the value which corresponded to the best match for the yawrate frequency response was different than that of the lateral velocity frequency response.

Table 6.1: Best Fit Relaxation Lengths

Freq Response	Sigma (m)
Yawrate	0.7
Lateral Velocity	1.2

Plots showing simulations with only these two values are shown below:

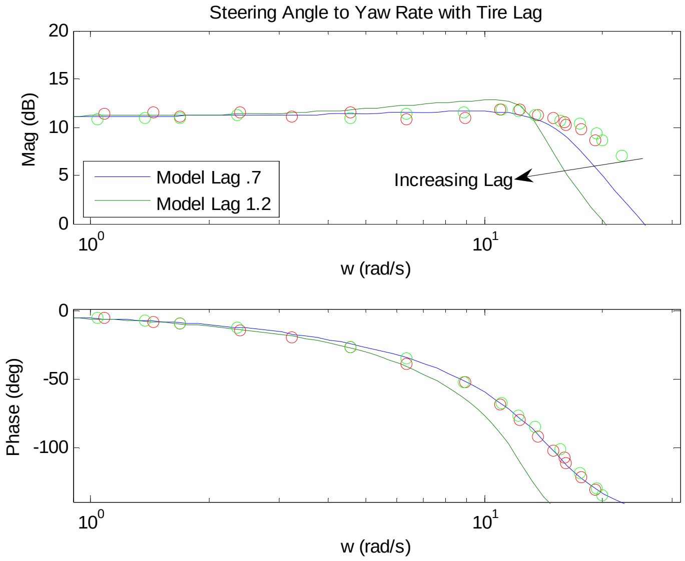

Figure 6.3: Yawrate – Frequency Response Best Fit Relaxation Lengths

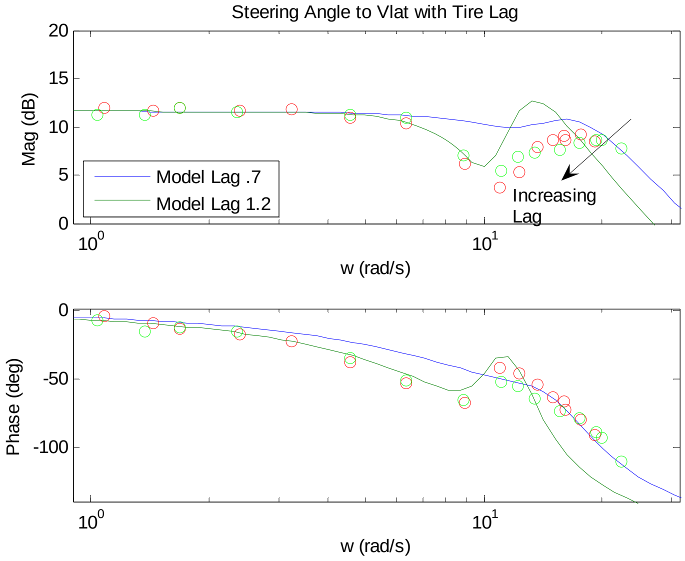

Figure 6.4: Lateral Velocity – Frequency Response Best Fit Relaxation Lengths

Since it is known the coupling between lateral velocity and roll is greater than that of yawrate and roll [7], and the bicycle model does not account for roll, it was decided that the relaxation length which corresponded to the best match of the yawrate frequency response would be used for further analysis – σ = 0.7m. With the relaxation length estimated from the frequency response, the time domain responses were repeated.

6.2.2 Chirp Response

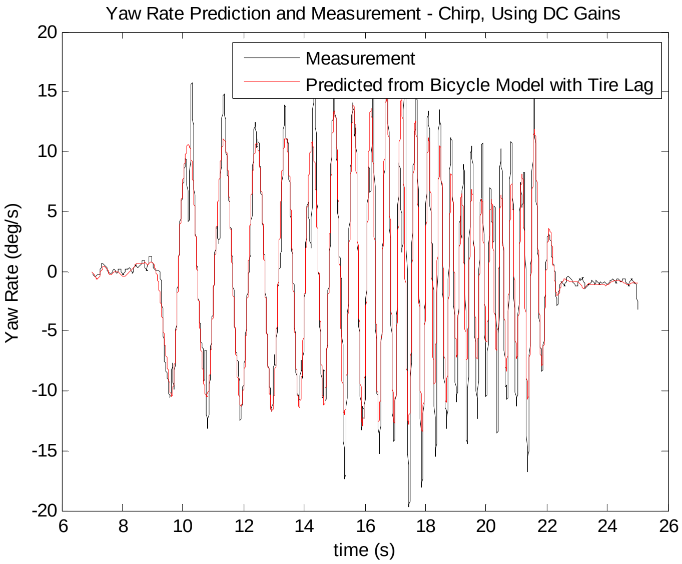

Figure 6.5: Yawrate – Chirp Response Lag Model

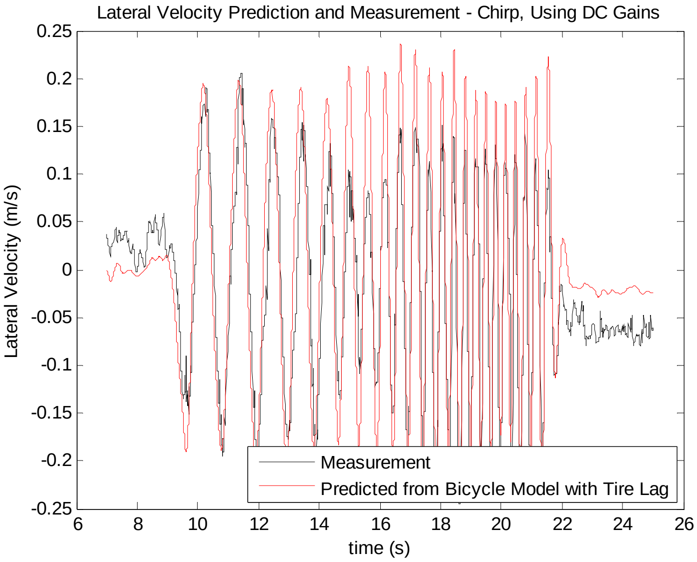

Figure 6.6: Lateral Velocity – Chirp Response: Lag Model

6.2.3 Steady State Circles

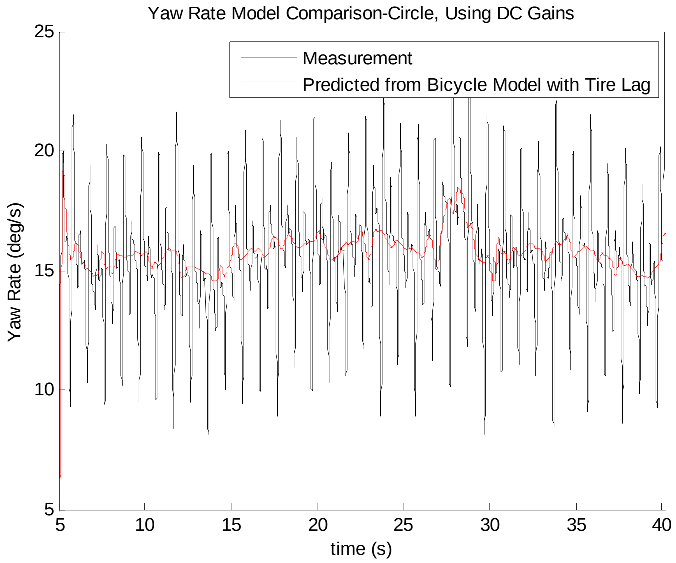

Figure 6.7: Yawrate – Steady State Circle: Lag Model

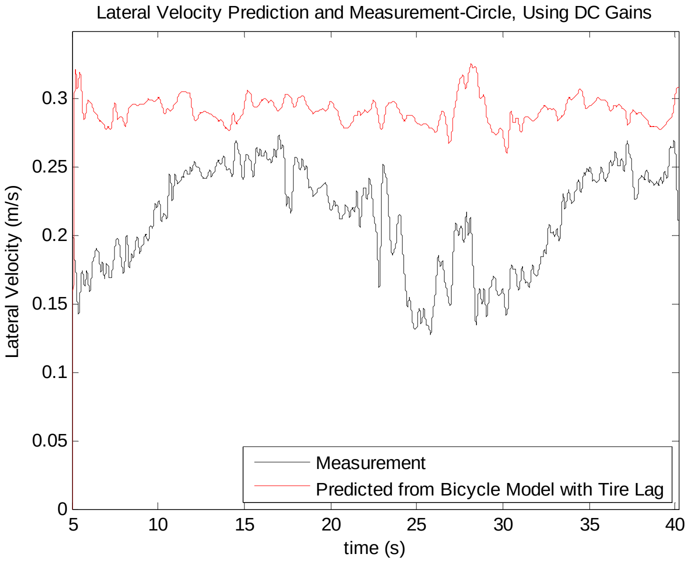

Figure 6.8: Lateral Velocity – Steady State Circle: Lag Model

6.3 Tire Lag Model – Results Discussion

6.3.1 Frequency Response

Figures 6.9 and 6.10 show a direct comparison between the Bicycle Model and the Lag Model in the frequency domain. As mentioned above, both models use the DC gain method to determine front and rear cornering stiffness values. The relaxation length which best fit the yawrate data was used for the simulation since lateral velocity is more strongly coupled to the un-modeled roll dynamics.

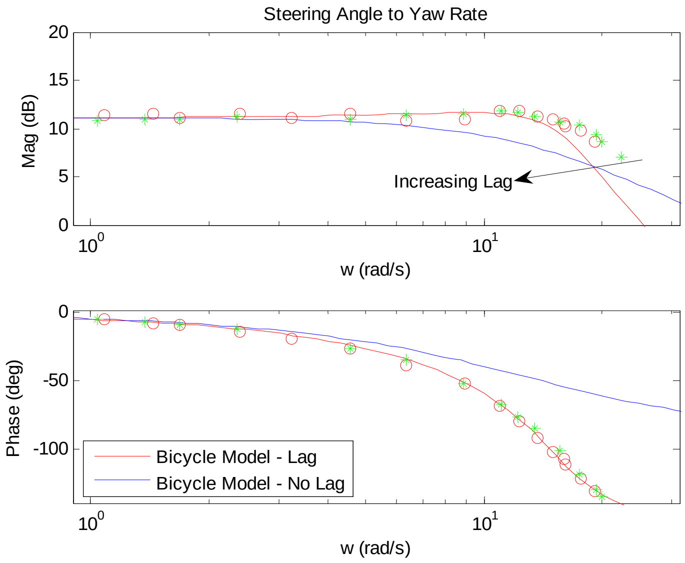

Figure 6.9: Yawrate – Lag Model and Bicycle Model Comparison – Freq Resp

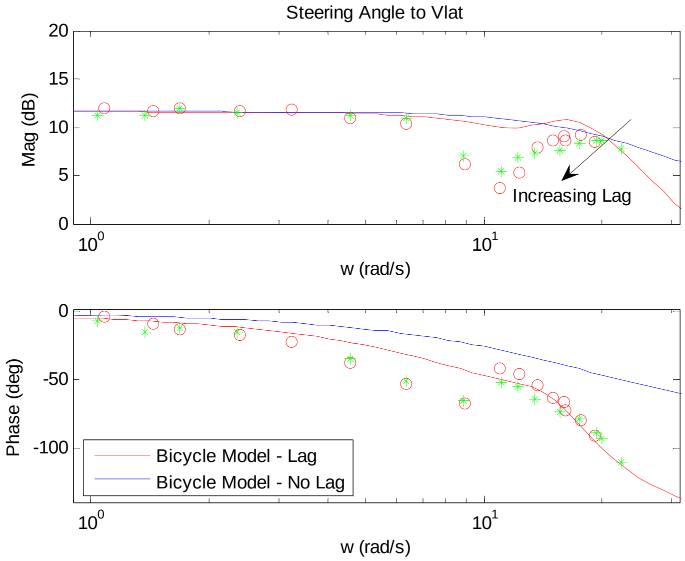

Figure **6.10**: Lateral Velocity – Lag Model and Bicycle Model Comparison – Freq Resp

The Lag Model is considerably more accurate in the frequency domain than the standard bicycle model. This is especially true at high frequencies – most notably in the phase plots. By modeling the tire force generation as an exponential rise to the steady state value, the models accuracy has greatly improved.

6.3.2 Chirp Response

Figures **6.11** and **6.12** show the comparison in the time domain for the chirp response:

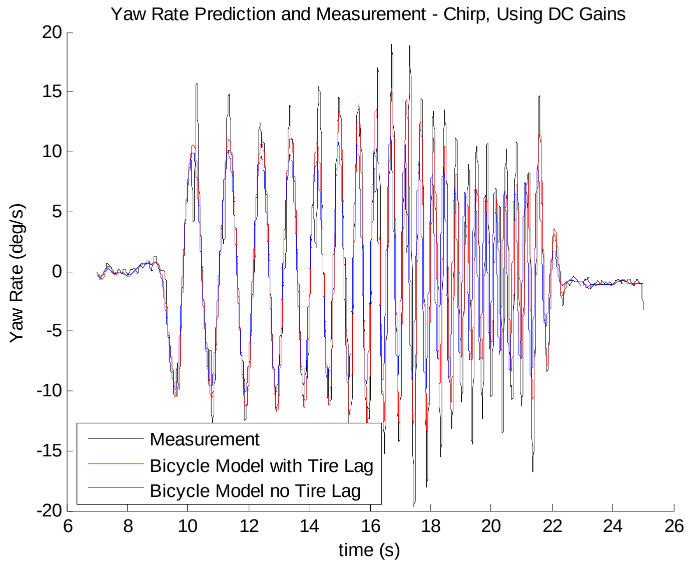

Figure 6.11: Yawrate – Lag Model and Bicycle Model Comparison – Chirp

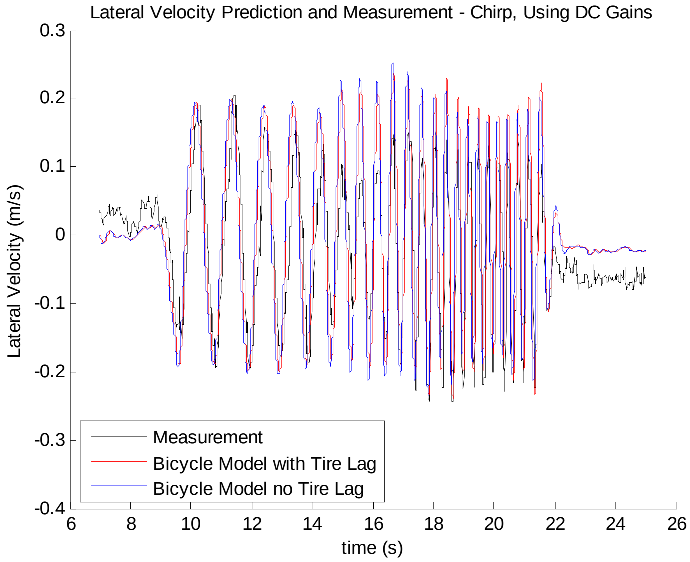

Figure 6.12: Lateral Velocity – Lag Model and Bicycle Model Comparison - Chirp

Once again the most drastic improvement is at the higher frequencies of the yawrate data. Both frequency and amplitude has improved by the addition of tire lag. The phase matched has been improved for lateral velocity; however the higher frequency amplitudes are still incorrect – as expected from the frequency response plots.

6.3.3 Steady State Circles

Perhaps the most interesting results come in the steady state circle comparison as shown in Figures 6.13 and 6.14:

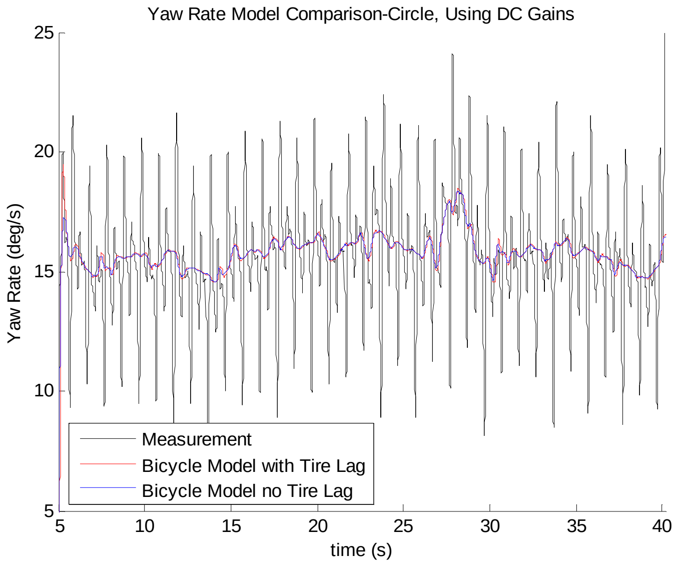

Figure 6.13: Yawrate – Lag Model and Bicycle Model Comparison – SS Circle

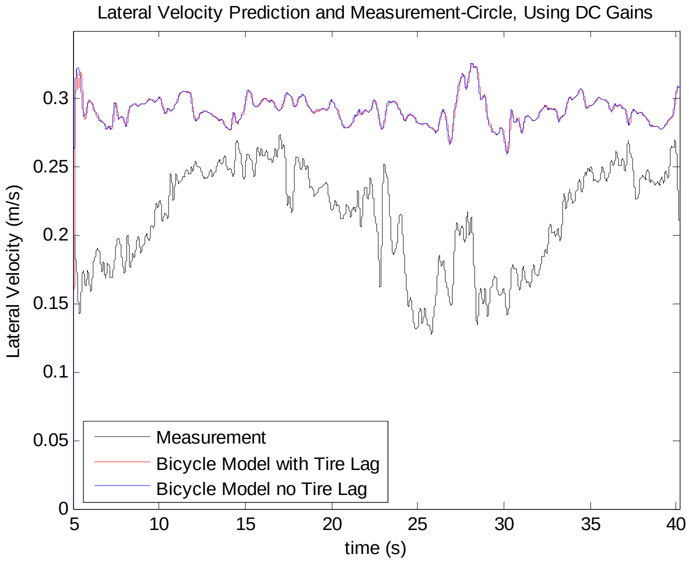

Figure 6.14: Lateral Velocity – Lag Model and Bicycle Model Comparison – SS Circle

It is nearly impossible to tell the two models apart in these cases. The Lag Model shows no real improvement over the standard bicycle model, and both still show poor model matching in the lateral velocity plots. There still exists a somewhat constant offset in the lateral velocity data in the steady state circle maneuver which is not present in the chirp or frequency response plots. As mentioned in chapter 5, this offset is believed to be due to the significant amount of body roll the vehicle sees in a steady state circle maneuver. The effect of vehicle roll angle on tire force generation has been supported and investigated by others, [8], and will be presented in detail in the next chapter.

6.4 Conclusions

- While tire relaxation length for the front and rear tires can be modeled independently, this significantly increases parametric variation difficulty and only has a minor effect on the model matching.

- The addition of rear relaxation length captures the higher order dynamics present at high frequencies. This was not apparent in previous work, [3],where the first order lag model was only introduced on the front steering input.
- Since lateral velocity is more strongly coupled with roll than yawrate, and the bicycle model does not model roll effects, the model is expected to fit yawrate data better than lateral velocity.
- The Lag Model does not improve the fit of steady state circle data. The constant offset on the lateral velocity plots should be investigated.

1. Gillespie, T.D., *Fundamentals of Vehicle Dynamics*. 1992: Society of Automotive Engineers (SAE). 495.
2. Heydinger, G.J., et al., *Dynamic Effects of Tire Lag on Simulation Yaw Predictions.* Journal of Dynamic Systems, Measurement and Control, Transactions of the ASME, 1994. **116**(2): p. 249-256.
3. Cameron, J.T., *Vehicle Dynamic Modeling for the Prediction and Prevention of Vehicle Rollover*. 2005: The Pennsylvania State University.
4. Carlson, C.R. and J.C. Gerdes. *Optimal Rollover Prevention with Steer-by-Wire and Differential Braking*. in *Proceedings of IMECHE*. 2003. Washington D.C.
5. Pacejka, H.B., *Tire and Vehicle Dynamics*. 2002, Warrendale, PA: SAE Press.
6. Karnopp, D., *Vehicle Stability*. 2004, New York: Marcel Dekker, Inc.
7. Laws, S. and J.C. Gerdes. *High-Frequency Vehicle Characteristics: Modeling and Experimental Validation of Yaw, Sideslip and Roll Modes. To be presented at: AVEC 2006 - 8th International Symposium on Advanced Vehicle Control*. 2006. Taipei, Taiwan.
8. Kim, H.-J. and Y.-P. Park, *Investigation of robust roll motion control considering varying speed and actuator dynamics.* Mechatronics, 2003.

Chapter 7

Bicycle Model – Camber Correction

In order to correct the model-data discrepancy in steady-state turns, a correction for roll camber was added into the two degree-of-freedom planar bicycle model. In a steady-state-state turn, a vehicle exhibits a significant amount of roll due to suspension dynamics. The roll of the vehicle can affect the forces generated by the tires through an effect known as camber thrust. Camber thrust represents the tilt induced on the tire due to the suspension. In the standard bicycle model these suspension effects are neglected which may result in poor model fits in high roll situations.

This chapter will present a camber correction for the bicycle model which is applicable for steady-state turns only. Simulations results and conclusions will then be presented.

7.1 Camber Correction Derivation

Camber is the inclination of a wheel outward from the vehicle body [1]. The effects of roll and tire camber on a tire's force generating abilities have been supported by the work of others. Kim and Park, [2], introduce an incremental change in force on the tire model in the form of:

$$\frac{\partial \alpha_f}{\partial \phi}\phi \qquad \textbf{7.1}$$

This effect is commonly known as "roll steer" and is usually assumed to be a constant value when the amount of tire slip is small. According to [2], the magnitude of the coefficient for the front tires was 0.2, and -0.2 for the rear tires.

In chapter 3 the equations of motion for a vehicle in a steady-state turn were used to derive the understeer gradient. The necessary front and rear lateral tire forces necessary to negotiate a turn or radius R at steady-state were written in equation 3.20 and are repeated here:

$$F_f = \frac{b}{L} \cdot \frac{mU^2}{R}$$
$$F_r = \frac{a}{L} \cdot \frac{mU^2}{R} \qquad 7.2$$

In the standard bicycle model derivation, the front and rear lateral forces produced by the tires were assumed to be equal to their slip angles multiplied by their cornering stiffnesses. In this derivation, the lateral forces produced also include camber thrust effect.

Figure 7.1 shows the rear view of a vehicle in a steady-state right hand turn.

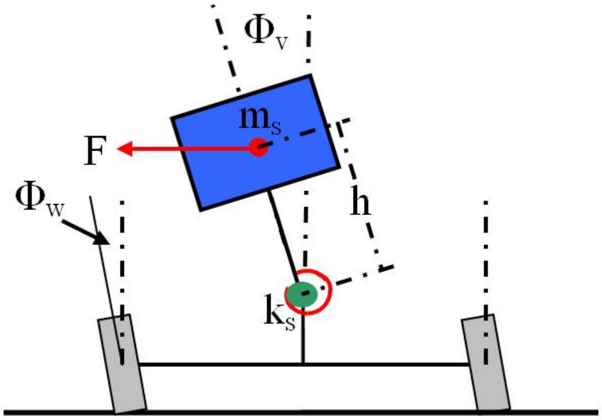

Figure 7.1: Vehicle Exhibiting Camber

In Figure 7.1 m$_s$ represents the sprung mass of the vehicle. When negotiating the turn, suspension dynamics will cause the mass will roll about its roll axis by an angle of Φ$_V$. At the same time, the wheels will roll from the vertical axis by an angle of Φ$_W$. This angle is known as the camber angle. Although the roll angle of the vehicle is not equal to the camber angle, the relationship between them can be assumed to be linear for small amounts of roll angle. Under this assumption the wheel angles can be modeled as:

$$\phi_w = S\phi_v \qquad 7.3$$

Where S is a constant to be referred to as the front or rear roll transfer constant.

It will be assumed that the vehicle suspension stiffness can be modeled as a rotational spring located on the roll axis with stiffness k_s as shown in Figure 7.2.

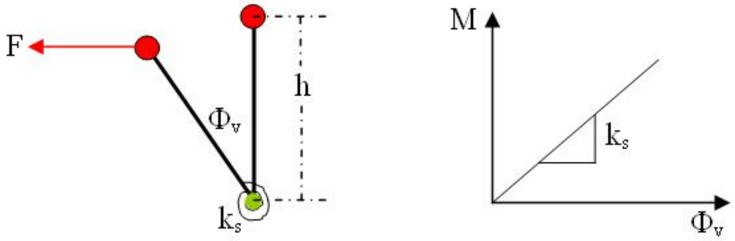

Figure 7.2: Rotation Spring Suspension Model

An expression relating the vehicle roll angle to the centripetal acceleration can be written by taking a force balance in the lateral direction and assuming small angles:

$$\frac{k_r \phi_v}{h} = \frac{m_s U^2}{R} \qquad 7.4$$

Combining and rearranging equations. 7.3 and 7.4 gives an equivalent expression for the camber angle:

$$\phi_w = S\phi_v = S\frac{m_s h}{k_r R}U^2 \qquad 7.5$$

Gillespie, [1], demonstrates that the lateral force generated by the tire, with camber effects accounted for can be modeled as

$$\begin{aligned} F_f &= C_{\alpha f}\alpha_f + C_{\phi f}\phi_{wf} \\ F_r &= C_{\alpha r}\alpha_r + C_{\phi r}\phi_{wr} \end{aligned} \qquad 7.6$$

Where C_Φ will be referred to the camber coefficient and the camber angles for the front and rear wheels have been assumed to be different.

Combining and rearranging equations 7.2, 7.5 and 7.6 to solve for the front and rear slip angles gives:

$$\begin{aligned} \alpha_f &= \frac{1}{C_{\alpha f}}\left[\frac{b}{L}\cdot\frac{mU^2}{R} - \frac{C_{\phi f} m_s h}{k_r} S_f \frac{U^2}{R}\right] \\ \alpha r &= \frac{1}{C_{\alpha r}}\left[\frac{a}{L}\cdot\frac{mU^2}{R} - \frac{C_{\phi r} m_s h}{k_r} S_r \frac{U^2}{R}\right] \end{aligned} \tag{7.7}$$

Since the camber coefficient (C_Φ), sprung mass (m_s), roll stiffness (k_r), CG to roll axis height (h), and camber transfer constant (S) are constant for both the front and rear equations, these terms can be lumped into new constants and equation 7.7 can be rewritten:

$$\begin{gathered} \alpha_f = \frac{1}{C_{\alpha f}}\left[\frac{b}{L}\cdot\frac{mU^2}{R} - C_f^* \frac{U^2}{R}\right] \\ \alpha r = \frac{1}{C_{\alpha r}}\left[\frac{a}{L}\cdot\frac{mU^2}{R} - C_r^* \frac{U^2}{R}\right] \\ \text{with} \\ C_f^* = \frac{C_{\phi f} m_s h}{k_s} S_f \\ C_r^* = \frac{C_{\phi r} m_s h}{k_s} S_r \end{gathered} \tag{7.8}$$

Equations 7.8 can be combined with the steady-state steering angle equation, equation. 3.15, to generate an expression for the steering input required to negotiate a turn at steady-state in terms of cornering stiffnesses and the lumped constants (which include the unknown camber transfer constants).

$$\delta_f = \frac{L}{R} - \frac{1}{C_{\alpha f}}\left[\frac{b}{L}\cdot\frac{mU^2}{R} - C_f^* \frac{U^2}{R}\right] + \frac{1}{C_{\alpha r}}\left[\frac{a}{L}\cdot\frac{mU^2}{R} - C_r^* \frac{U^2}{R}\right] \tag{7.9}$$

In its present form, equation. 7.9 has four parameters which are not easily measured – the front and rear cornering stiffnesses ($C_{\alpha f}$,$C_{\alpha r}$) and the lumped constants (C^*_f, C^*_r).

In order to quantify the effects of roll steer, the bicycle model needs to be modified. To fit the camber parameters, it is assumed that the effects of camber are negligible with low-roll maneuvers such as low frequency sinusoidal inputs used to determine the DC gains for the frequency responses. This assumption allows the cornering stiffness values obtained through the DC gains of the frequency response to be used in this derivation. The validity of this assumption can be shown by investigating the results from chapter 6. When the DC gains were used to solve for the front and rear cornering stiffnesses, and these values were used in the standard bicycle model (not accounting for camber) the model matches for low frequency portion of the chirp response were excellent. However, as the frequency of the steering input approaches the natural frequency of the vehicle, roll and therefore camber angle increases and the model match quality decreases. Also the high-roll steady-state turn maneuvers also show poor matching.

By using data collected from low frequency sine waves and the standard bicycle model equations, the four unknowns in equation. 7.9 can be solved.

The first two equations to be used in solving for the four unknowns are the standard bicycle model DC gain equations presented in chapter 5 for low frequency sinusoidal inputs. As in chapter 5, these equations can be used to solve for the front and rear cornering stiffnesses since these values were shown to be valid for these maneuvers. In addition to solving for cornering stiffnesses, the yawrate DC gain equation can help solve for the remaining two unknowns: C^*_f and C^*_r.

As discussed above, the effect of camber must be accounted for in a steady-state circle maneuver. The DC gain for the steady-state circle maneuver, accounting for camber, can be written by dividing the steady-state yawrate by the required steady-state steering input as described in equation 7.10 :

$$\left.\frac{r}{\delta_f}\right|_{circle} = \frac{\dfrac{U}{R}}{\dfrac{L}{R} - \dfrac{1}{C_{\alpha f}}\left[\dfrac{b}{L}\cdot\dfrac{mU^2}{R} - C_f^*\dfrac{U^2}{R}\right] + \dfrac{1}{C_{\alpha r}}\left[\dfrac{a}{L}\cdot\dfrac{mU^2}{R} - C_r^*\dfrac{U^2}{R}\right]} = G_{r,cricle} \qquad \mathbf{7.10}$$

Equation 7.10 can be rearranged to solve for C^*_f in terms of C^*r

$$C_f^* = \left(\frac{1}{G_{r,circle}\cdot U} - m\cdot\left(\frac{a}{L\cdot C_{ar}} - \frac{b}{L\cdot C_{af}}\right) - \frac{L}{U^2} + \frac{C_r^*}{C_{\alpha r}}\right)\cdot C_{\alpha f} \qquad \mathbf{7.11}$$

The above equation has only two unknowns (C^*_f, C^*_r), three measurable parameters (U,a,b,m), and the two cornering stiffness values which were determined using the DC gain method.

To get a final equation to solve for the remaining unknowns, the behavior of the rear of the vehicle in a steady-state turn must be revisited. As in equation **5.24**, the lateral velocity of a vehicle in a high speed turn can be expressed as:

$$V = U\left(\frac{b}{R} + \alpha_r\right) \tag{7.12}$$

Using equation **7.12** and **7.9** the equation for the lateral velocity gain for a steady-state circle can be written:

$$\left.\frac{V}{\delta_f}\right|_{circle} = \frac{U \cdot \left(\frac{b}{R} + \alpha_r\right)}{\frac{L}{R} - \frac{1}{C_{\alpha f}}\left[\frac{b}{L}\cdot\frac{mU^2}{R} - C_f^*\frac{U^2}{R}\right] + \frac{1}{C_{\alpha r}}\left[\frac{a}{L}\cdot\frac{mU^2}{R} - C_r^*\frac{U^2}{R}\right]} \tag{7.13}$$

$$\left.\frac{V}{\delta_f}\right|_{circle} = G_{v,circle}$$

Equation **7.13** is particularly useful when it combined in a ratio with equation **7.10**

$$\frac{G_{v,circle}}{G_{r,circle}} = \frac{U\left(\frac{b}{R} + \alpha_r\right)}{\frac{U}{R}} \tag{7.14}$$

By using the expression for the rear slip angle derived in equation **7.8**, equation **7.14** can be rewritten and simplified to:

$$\frac{G_{v,\, circle}}{G_{r,\, circle}} = \left(b + \frac{U^2}{C_{\alpha r}}\left(\frac{a}{L}\cdot m - C_r^*\right)\right) \tag{7.15}$$

Finally equation **7.15** can be solved for C^*_r in terms of measurable parameters:

$$C_r^* = \frac{a}{L}\cdot m - \frac{C_{\alpha r}}{U^2}\cdot\left(\frac{G_{v,circle}}{G_{r,circle}} - b\right) \tag{7.16}$$

Below is a summary of the four equations used to solve for the four unknowns $C_{\alpha f}, C_{ar}, C_f^*, C_r^*$:

$$C_{\alpha r} = \frac{\left(a \cdot m \cdot U^2 \cdot G_{r,\sin e}\right)}{\left(G_{v,\sin e} - b \cdot G_{r,\sin e}\right) \cdot (a+b)} \qquad 7.17$$

$$C_{af} = \frac{\left(-b \cdot m \cdot U^2 \cdot G_{r,\sin e} \cdot C_{\alpha r}\right)}{\left(C_{\alpha r} \cdot U \cdot (a+b) - G_{r,\sin e} \cdot C_{\alpha r} \cdot (a+b)^2\right)} \qquad 7.18$$

$$C_r^* = \frac{a}{L} \cdot m - \frac{C_{\alpha r}}{U^2} \cdot \left(\frac{G_{v,circle}}{G_{r,circle}} - b \right) \qquad 7.19$$

$$C_f^* = \left(\frac{1}{G_{r,circle} \cdot U} - m \cdot \left(\frac{a}{L \cdot C_{ar}} - \frac{b}{L \cdot C_{af}} \right) - \frac{L}{U^2} + \frac{C_r^*}{C_{\alpha r}} \right) \cdot C_{\alpha f} \qquad 7.20$$

Where equations 7.17 and 7.18 are repeated from chapter 5 equations 5.30 and 5.2 respectively and equations 7.19 and 7.20 are repeats of equations 7.15 and 7.11 respectively.

7.2 Camber Correction – Simulation Results

Since the relationship shown in equation 7.4 utilizes the centripetal force seen by a vehicle as it negotiates a steady-state turn, this derivation is only valid for steady-state turns. In order to incorporate all maneuvers, a full roll model must be derived however, such a model is not needed in this work, and therefore will not be presented. The impact of the roll steer derived above will therefore only be investigated in the steady-state turning maneuver.

7.2.1 Steady-state Circles

Figures 7.3 and 7.4 show the time domain model matching for steady-state circles for the model with and without the roll/camber correction:

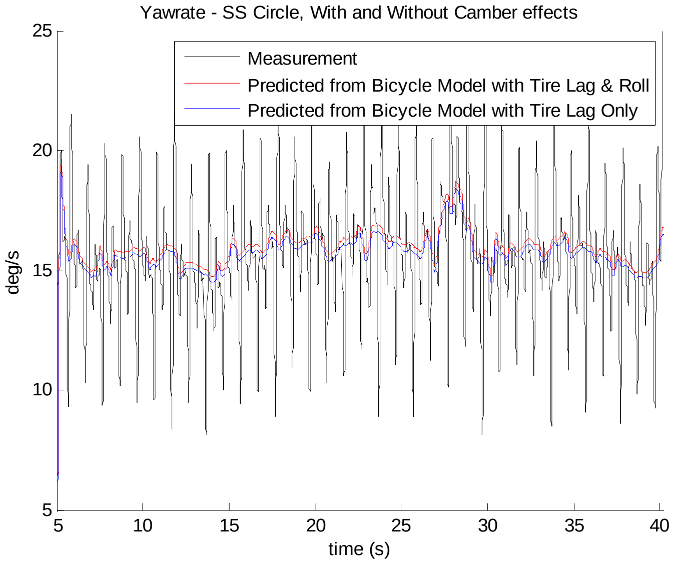

Figure 7.3: Yawrate – Camber Model – SS Circle

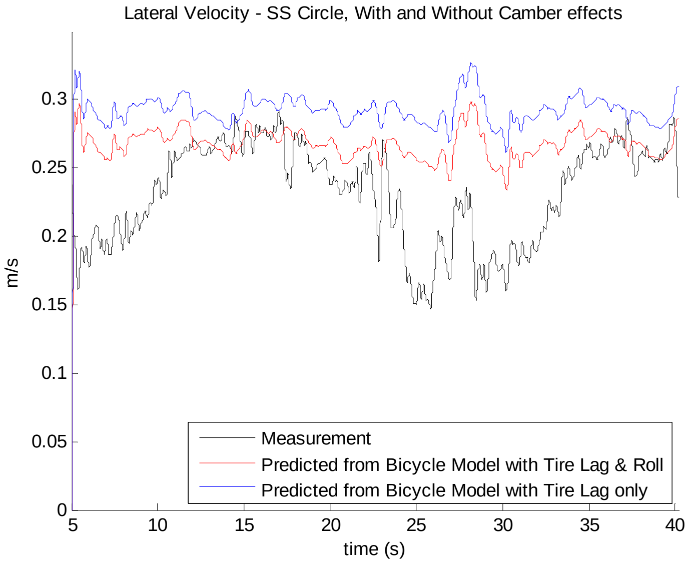

Figure 7.4: Lateral Velocity – Camber Model – SS Circle

As seen in Figure 7.3, the yawrate plot has not been significantly changed and the model still accurately predicts this state. In Figure 7.4 it is clear that the constant offset value in the lateral velocity plot has been decreased by the addition of a camber model. This confirms the theory that vehicle roll is affecting the tire force generation in steady-state turns. A full roll model can be used to further investigate the roll/camber effects in other driving situations.

7.3 Conclusions

- A method of incorporating roll steer/camber effects into the bicycle model has been presented
- Roll steer is clearly affecting the lateral velocity measurements in high roll maneuvers such as the steady-state turn.

1. Gillespie, T.D., *Fundamentals of Vehicle Dynamics*. 1992: Society of Automotive Engineers (SAE). 495.
2. Kim, H.-J. and Y.-P. Park, *Investigation of robust roll motion control considering varying speed and actuator dynamics.* Mechatronics, 2003.

Chapter 8

Terrain Disturbances for Longitudinal Positioning

While performing the state estimation described in the previous chapters, it became apparent that the terrain was greatly affecting the collected data. This was most obvious when viewing sideslip, roll and pitch data during the steady-state circle maneuvers which were used to experimentally determine understeer gradient. The repetitive, location-dependent nature of these terrain disturbances allows them to be used in a localization routine. This chapter will outline the theory of using road grade for longitudinal positioning.

8.1 Initial Terrain Disturbance Observations

The repetitive nature of the disturbances caused by the vehicle-terrain interaction was first observed during post-processing of steady-state circle data. This data was collected at various speeds, for two different circles traveling in two different directions. When the data was aligned to start at the same position, common trends became apparent as shown in Figure 8.1:

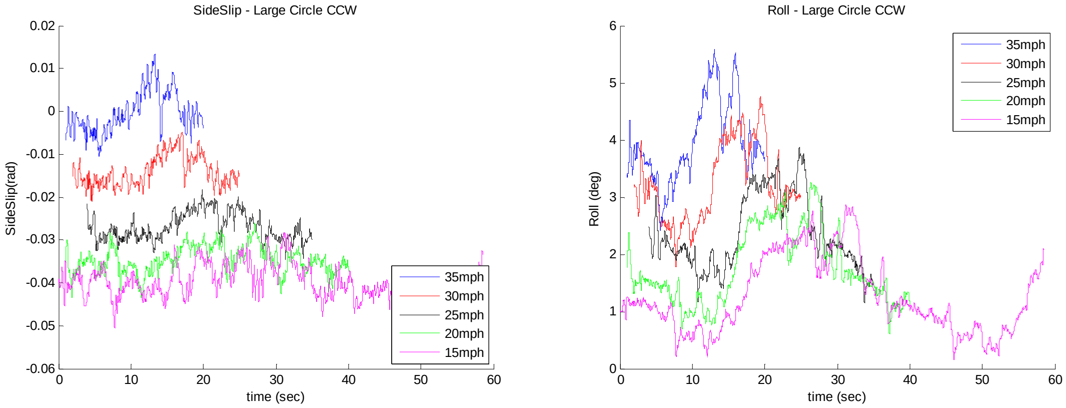

Figure 8.1: Initial Observation of Terrain Disturbance

Ideally the roll and sideslip angles for each constant velocity, steady-state circle would be constant. However, it is obvious that the measurements have been skewed by the terrain. This has also been observed elsewhere in literature, where attempts have been made to remove terrain effects from readings in order to improve their accuracy [1, 2].

This chapter will examine how to quantify and utilize these repetitive, location-dependent disturbances to obtain accurate position estimations by correlating current disturbances with those of a disturbance map.

8.2 Road Grade Estimation

For the purposes of this work, road grade is defined as the angle of the road with respect to the horizontal plane in the longitudinal direction. Road grade estimation has been performed extensively for heavy-vehicle applications to ensure safety and to appropriately distribute engine power to overcome steep inclines [3-5]. Two simple GPS-based methods of road grade estimation, presented by Bae et al, [5], were investigated in this work. A schematic showing the road grade angle is presented in Figure 8.2:

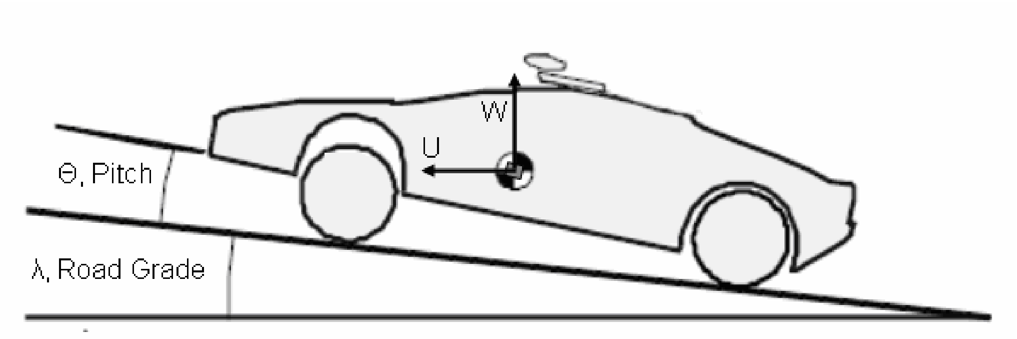

Figure 8.2: Pitch and Road Grade

Where W is the vehicle's vertical velocity, U is its longitudinal velocity, θ is the pitch angle and λ is the road grade.

In [5], a two-antenna GPS system mounted to the roof of the vehicle is used to measure the orientation of the vehicle in the X-Z plane at a 5 Hz rate. The angle measured is the sum of the pitch and road grade angle. It is influenced by the vehicle's acceleration as well as high-frequency road irregularities and will likely include a constant angle offset due to sensor mounting. Bae points out that since the road grade usually changes slower than the pitch motion of the vehicle, the low frequency portion of the pitch measurement can be used to estimate the road grade. In Bae's work, a 0.5 Hz low-pass filter is applied to the pitch signal to approximate road grade. One must note that in his work, the road grade was not used to assist with positioning, but to approximate the engine torque required to overcome an uphill climb. Therefore the distance resolution of the measurement was not critical and a low sampling frequency was sufficient.

In order to achieve an accurate position estimate from road grade, the road grade estimates must have high spatial resolution. In this work, the angle corresponding to the sum of the pitch and road grade is directly measured by the IMU at a 50 Hz rate with the capability of sampling at 100 Hz. The constant angle offset due to IMU mounting can then be subtracted out of the measurement in real-time since this offset was determined using the IMU calibration techniques outlined in section 4.1.1.2. The resulting measurement can then be low-pass filtered as in [5] to estimate the road grade.

A second method discussed by Bae, [5], uses GPS vertical and horizontal velocities to estimate road grade. In this work, the vertical and horizontal velocities are measured by the IMU at the CG. Therefore road grade can be estimated as:

$$\lambda = \tan^{-1}\left(\frac{W}{U}\right) \qquad 8.1$$

Once again a low-pass filter can be applied to the road grade estimation to help remove the higher frequency vehicle dynamics and road irregularities.

Bae's, [5], investigation into the differences between these two methods revealed that the pitch-based estimate shows oscillation during periods of rapid acceleration or deceleration, while the velocity-based estimation is less sensitive to accelerations. However outside the periods of acceleration, the velocity-based measurements show more variability and oscillation.

For comparison, both methods of estimation were compared in their approximation of road grade. Both methods were tested on a steady-state turn maneuver with a low-pass cutoff filter frequency of 1.5 Hz. This is shown in Figure 8.3.

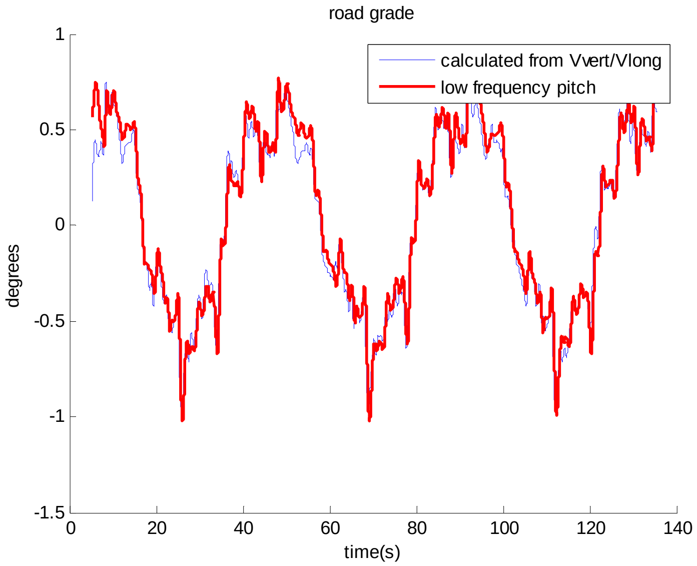

Figure 8.3: Road Grade Estimation – Method Comparison

It is obvious that the two methods give similar road grade estimates for the steady-state turning maneuver shown above.

For an initial investigation into using road grade for positioning, the low-frequency pitch method was used instead of the velocity-based method. Since the pitch measurement is already computed in real-time no extra computation is necessary. The oscillation effects of acceleration pointed out by Bae are eliminated from the pitch-method by assuming constant longitudinal velocity. The IMU mounting offset error is accounted for by utilizing the calibration routine as described previously. Utilizing the pitch method above also allows for a GPS-free positioning system which can use commercial grade sensors to measure pitch angle. If necessary, a more accurate solution may be obtained by applying a Kalman filter to blend the two estimation methods. This however will not be done here.

It should also be noted that the disturbances in other states such as roll, sideslip and yaw rate can also be analyzed. However these states are more dependent on vehicle parameters and road conditions which would make identifying disturbances in these measurements difficult. Therefore only the pitch-plane disturbances will be considered in this work.

8.3 Road Grade Repeatability and Location Dependence

In order to use the road grade estimation in a positioning routine, it must be highly repeatable as a function of position. This repeatability is most easily tested by driving over the same terrain and comparing road-grade measurements. The results of this experiment are shown below using steady-state circle data. Figure **8.4** shows the road grade estimate for several passes around the skid-pad turning circle. Plotted below the road grade is the yaw angle, measured in degrees from north to show the vehicle heading. Note that the skid pad is one of the flattest portions of the test rack and it is therefore likely that public roads would provide a much better signal-to-noise ratio.

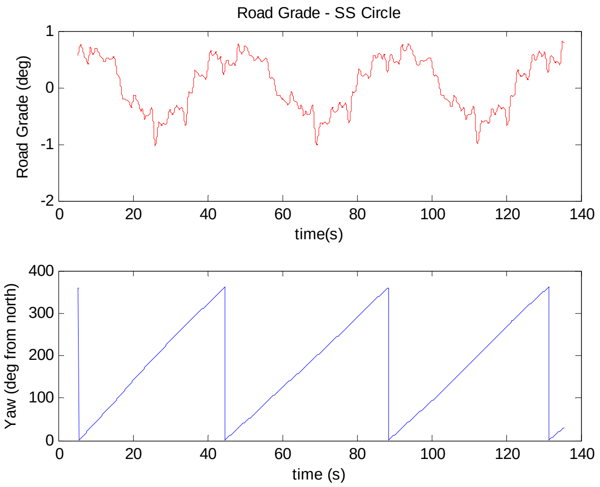

Figure 8.4: Road Grade Repeatability

In order to demonstrate the location dependence of the road grade estimate, steady-state circle data was collected starting at the same point but traveling at various speeds. Figure 8.5 shows two plots for the same data plotted as a function of time (left) and as a function of path distance (right) where path distance was calculated by integrating the longitudinal velocity measurements.

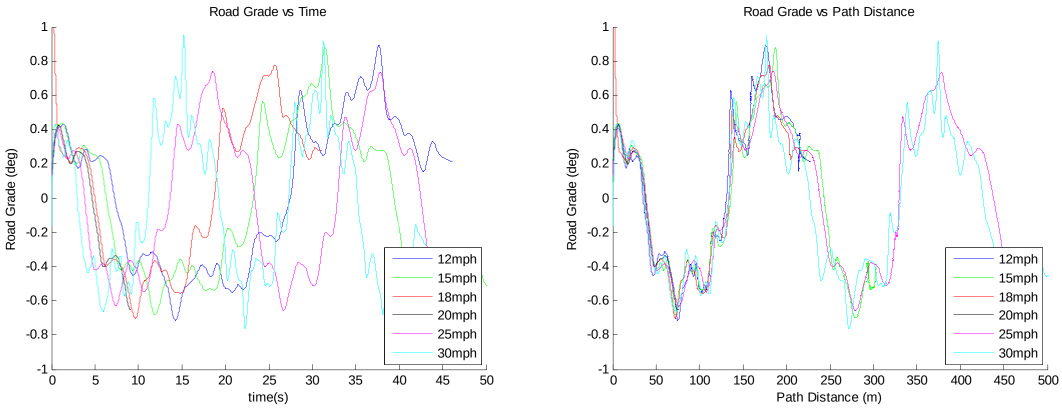

Figure 8.5: Road Grade

Figure 8.5 emphasizes not only the location dependence, but also the repeatability.

These results clearly show that the road grade measurement can be used for longitudinal positioning. If a road grade map template is created for a given path, a vehicle's position along that path can easily be determined by fitting onboard road grade measurements to those of the mapped template. This theory was tested by mapping the inside travel lane of the test track at the Pennsylvania Transportation Institute, with results described in the next section.

8.4 Road Grade Positioning

A road grade template of the entire inside travel lane of the test track at the Pennsylvania Transportation Institute was made by recording the vehicle's pitch, velocity and position while it was driven around the path. After the template data was recorded, the vehicle was driven around the same path and data was recorded over five random sections of track in 10-15 second intervals.

In post-processing, the sample and template pitch measurements were transformed to be a function of path length instead of time by integrating the vehicle velocity measurements with respect to time. In order to get an approximation of the positioning routine's error, the vehicle path and road grade measurements were decimated and interpolated to occur at 25 cm intervals to allow for a direct path-dependent comparison between the road grade estimates. The 25 cm interval was selected since the highest average velocity of any of the data sets was 12.5 m/s and the sampling frequency was 50 Hz. This corresponds to 25 cm between samples at the highest speed. The data was then passed through a 2 pole low-pass Butterworth filter to estimate road grade. It is important to note that the cutoff frequency of the filter was constant among each data set in the *spatial* (distance) domain as opposed to the time domain. This transformation to distance-dependent filtering is desirable because the data sets were collected at different speeds. With data at different speeds, a filter in with a cutoff frequency of f_c applied in the time domain will result in different levels of spatial smoothing for each data set when they are taken to the spatial domain. Therefore it is important to decimate and interpolate the data at specific and uniform distance increments *before* applying a constant cutoff frequency filter.

In order to compare the road grade estimates, the Pearson Product-Moment Correlation Coefficient was calculated for the sample road grade estimates and sections of the road grade template. The correlation coefficient is calculated by:

$$Cor = \frac{E[(Y_1(x) - \bar{Y}_1(x)) \cdot (Y_2(x) - \bar{Y}_2(x)]}{N \cdot \sigma_{Y1} \cdot \sigma_{Y2}} \qquad \mathbf{8.2}$$

Where: $Y_1(x), Y_2(x)$ are the road grade as a function of path distance covered for the template and the sample respectively.
$\bar{Y}_1, \bar{Y}_2$ are the mean of Y_1 and Y_2 respectively
σ_{Y1}, σ_{Y2} are the standard deviations of Y_1 and Y_2 respectively, and
$E[\ ]$ indicates the expected value, or mean.

This correlation coefficient is a measure of the strength of the relationship or association of two independent variables. Its value varies from -1 to 1 where -1 indicates variables which are opposites, and 1 indicates exact matches. A fast MATLAB function to calculate the Pearson correlation, prcorr2, is used for this application.

The steps used to position the vehicle along the template path using the Correlation Coefficient are described below. It should be noted that this method is used to position the vehicle offline; therefore these steps would have to be modified to work in a real-time routine.

1) Determine the approximate path distance covered by the sample data by integrating the vehicle's velocity with respect to time.
2) Section the track template to cover the same path distance as that covered by the sample data
3) Calculate the correlation coefficient between the road grade measurements of the sample data and the sectioned template
4) Shift the template section by one decimation length.
5) Repeat steps 2-4 until the end of the template has been reached
6) Determine maximum Correlation Coefficient calculated for the entire template

7) Find the path along the template corresponding to the location of the maximum Correlation Coefficient

To estimate the error associated with this positioning routine, the true positions of the vehicle were recorded by the DGPS system during the road-grade template construction and during the collection of the test samples. This allows the positioning error to be calculated by comparing positions from DGPS to those calculated via correlated road-grade. If the error were calculated directly from the DGPS readings, it would include both the road grade positioning routine's error as well as the lane keeping error associated with the driver's inability to exactly repeat the path traveled for the template generation. In order to isolate the error due to the positioning routine only errors in the direction of travel are considered. To estimate these errors, the path of the sample data must be projected onto the path traveled during template generation. This error estimation is computationally intensive and is only used for this proof of concept. The method presented pictorially in Figure 8.6 and is explained below:

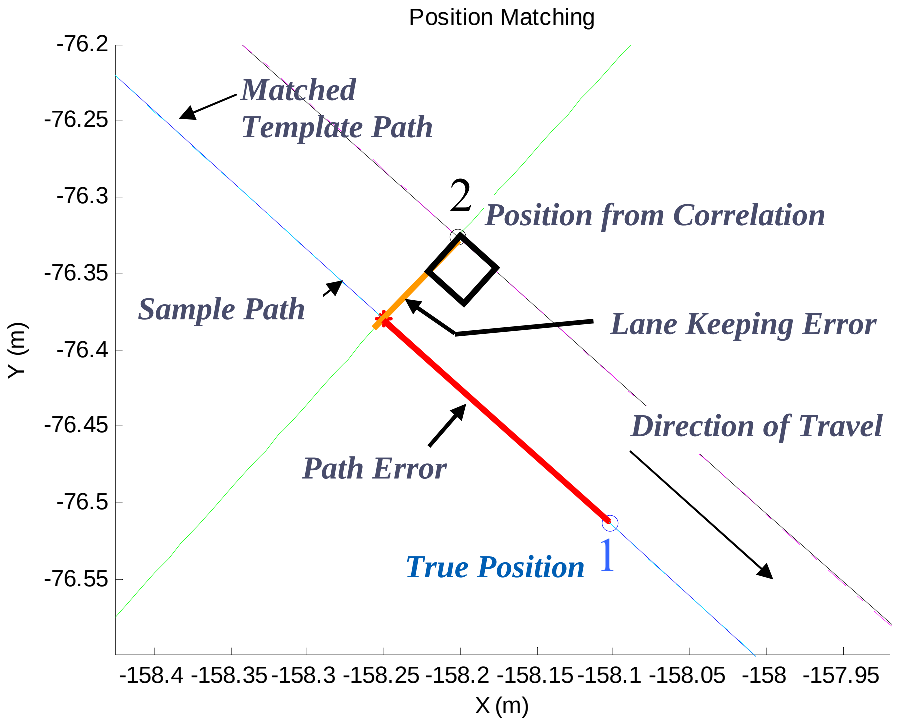

Figure 8.6: View of Error Calculation

First the road grade correlation is performed and the section of the template which best matches that of the sample data is extracted from the template. This section is the "Matched Template Path" in Figure 8.6 and it contains the same number of points as the "Sample Path." After the correlation, each data point along the "Sample Path" will have a corresponding data point on the "Matched Template Path". According to the road grade positioning routine, the point labeled ***1*** on the "Sample Path" corresponds to the point labeled ***2*** on the "Matched Template Path." Tangent lines are then drawn on both the "Sample Path" and the "Matched Template Path" at points ***1*** and ***2*** respectively. A line perpendicular to the "Track Tangent" is then drawn to intersect the "Sample Path." The error along the direction of travel is then determined to be the distance from point ***1*** on the "Sample Path" and the intersection of the "Sample Tangent" and "Track Perpendicular."

As mentioned previously, this error calculation is elementary and is not fit for real-time data processing; however it is sufficient as an initial estimate of the path error associated with the road grade positioning routine.

This error calculation was performed for every Template-Sample pair of points and the average error across all pairs was calculated. This was then repeated for all five data sets which were collected. This initial error estimate shows promising results. All but one data sample set collected show an average error of *less than one meter*. Table 8.1 below summarized the correlation values and average error estimates for the five samples:

Table **8.1**: Average Error Estimates and Correlation Values

Sample	Average |Error|	Standard Deviation	Average |Lane Keeping Error|	Correlation
1	134 cm	27 cm	48.6 cm	0.9105
2	15 cm	12 cm	11.5 cm	0.9898
3	9 cm	5 cm	9.7 cm	0.9893
4	66 cm	14 cm	16.7 cm	0.9610
5	13 cm	14 cm	9.1 cm	0.9889

The road grade matches corresponding to the highest correlation values for each of the five sample sets are shown below.

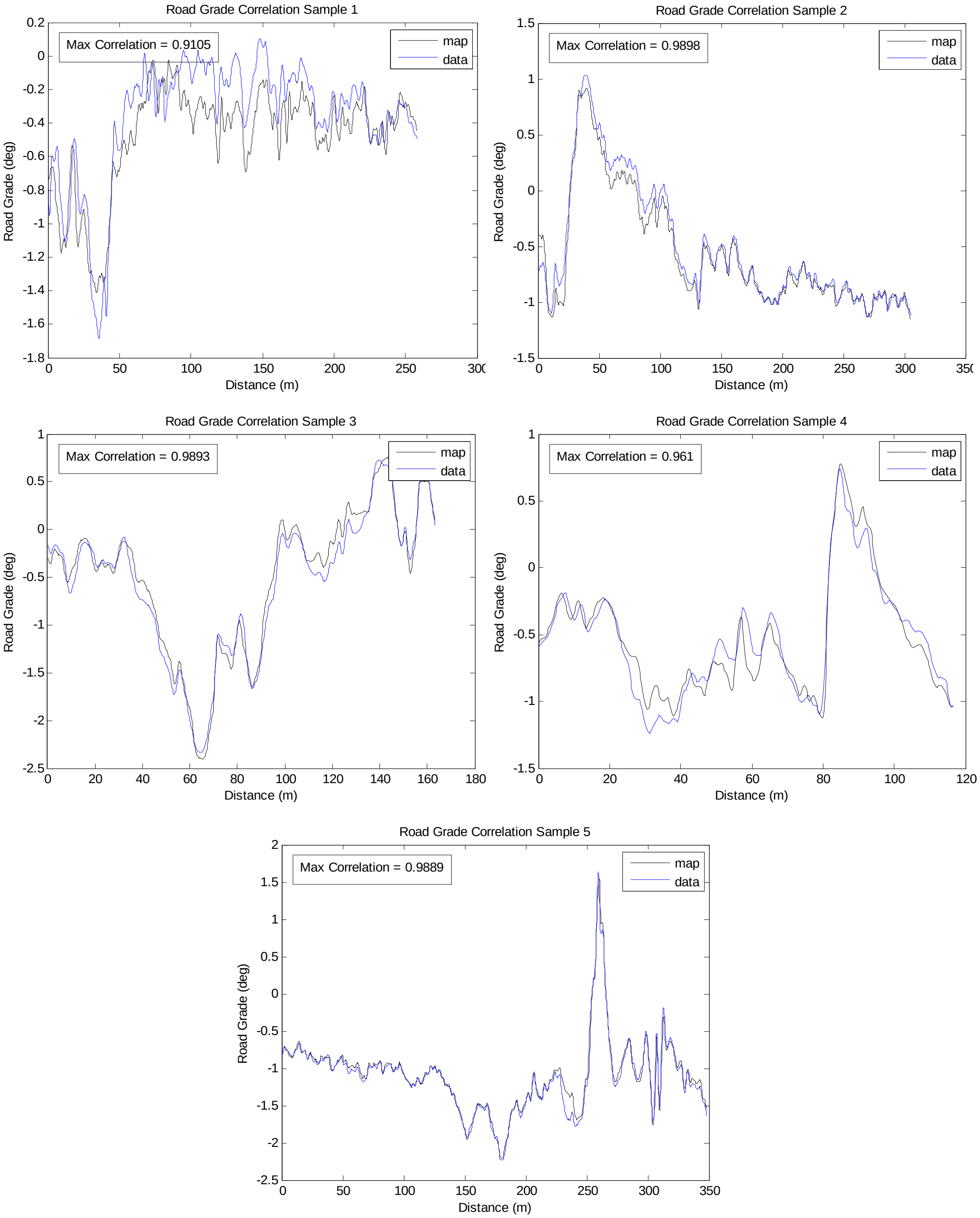
Road Grade Correlation Sample 1

Road Grade Correlation Sample 2

Road Grade Correlation Sample 3

Road Grade Correlation Sample 4

Road Grade Correlation Sample 5

Figure 8.7: Road Grade Matches

The position match for the third sample is presented in Figure 8.8:

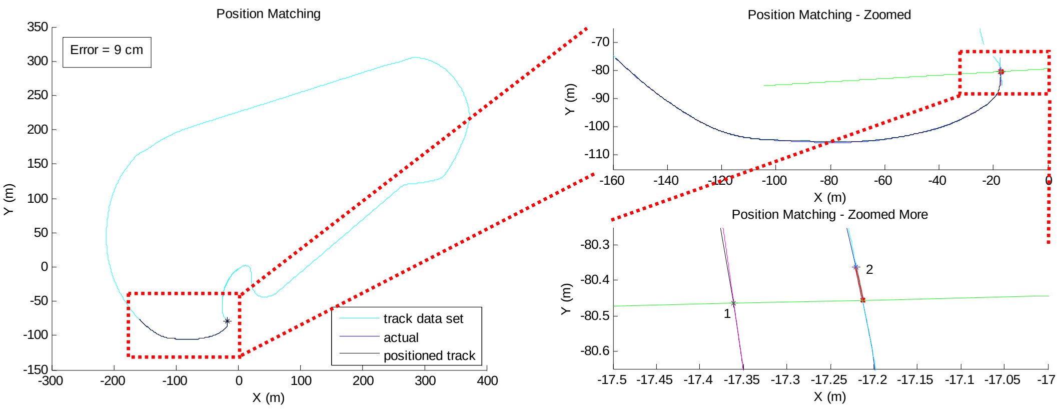

Figure 8.8: Position Match – Sample 3

The path error for each Template-Sample pair for the third sample is presented in the error histogram below:

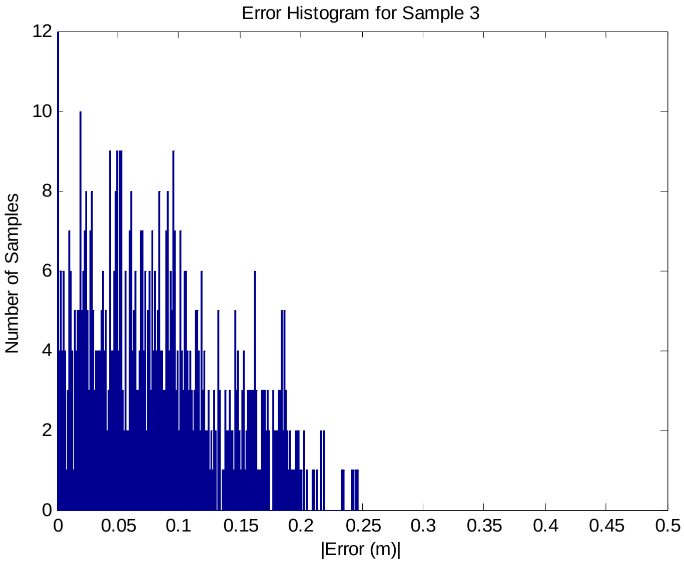

Figure 8.9: Error Histogram – Sample 3

As reported in Table 8.1 , the mean error for Sample 3 was calculated to be 9 cm, with a standard deviation of 5 cm.

It is interesting to note, that Sample 1 had both the highest path error and the highest lane keeping error. This shows that accuracy of this method of positioning is highly dependent on the vehicle's ability to keep the mapped path.

Although an improved method of error calculation is needed, the results obtained with this elementary method were sufficient enough to prove the validity of the road grade positioning concept.

8.5 Longitudinal Positioning

The first step in implementing this road grade positioning routine in practice is to accurately position a vehicle driving in a straight line. This would best represent a daily drive to work, where drivers are often driving on long stretches of interstate at relatively constant velocities. In order to emulate this scenario, a stretch of the test track was sectioned off with cones to simulate a highway lane. An image from the in-vehicle video camera system is shown below:

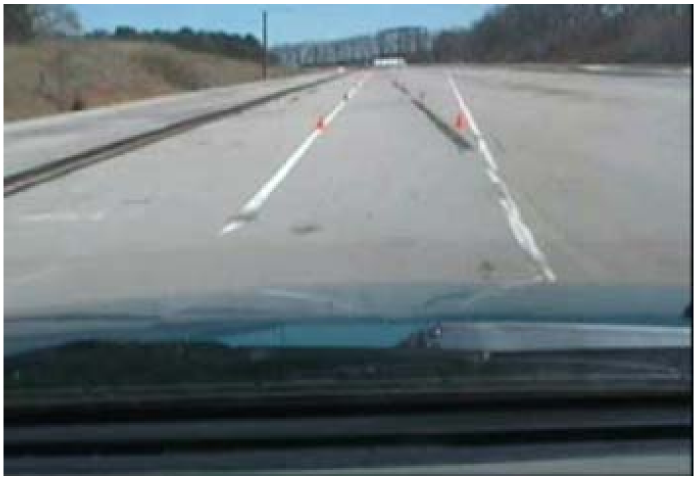

Figure 8.10: Single Lane Experiment

To increase the spatial resolution for this experiment, the pitch and velocity samples are taken at a 100Hz rate. An estimate of the path distance covered by the vehicle is calculated by integrating the velocity measurements with respect to time. The most accurate, highest resolution map is desired for the template generation and this can be obtained by driving the target lane at very low velocities. For this experiment, the map was generated at the near-idle speed of 5mph.

Several samples were then collected to investigate the effect of velocity on the positioning routine. To do this, the vehicle was driven over the same path at various speeds ranging from 5-65 mph while the vehicle states were recorded. The unfiltered pitch measurements recorded at various speeds have been aligned and plotted for comparison in Figure 8.11:

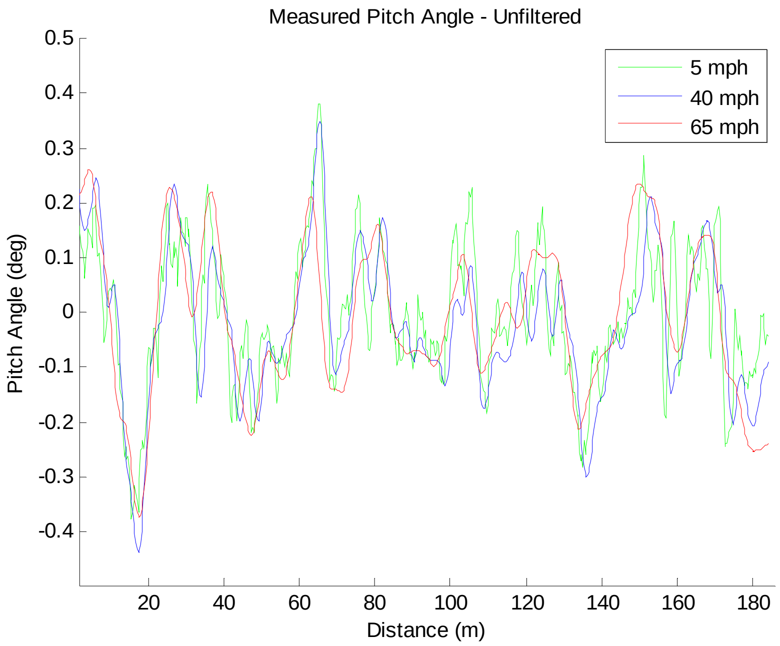

Figure 8.11: Road Grade Velocity Dependence

Figure 8.11 shows the measured pitch angle varies with speed. As the vehicle's speed increases, the frequency at which the position-dependent road disturbances will occur increases. Since the suspension acts as a low-pass filter, the vehicle's pitch measurements are filtered at high speeds. The frequency of this low-pass filtering effect is dependent on the vehicle's mass distribution and suspension characteristics. To directly see the low-pass filtering effect of the vehicles suspension, a Fourier Fast Transform (FFT) can be performed on the raw, unfiltered pitch measurements. The data used for the FFT must be a function of distance:

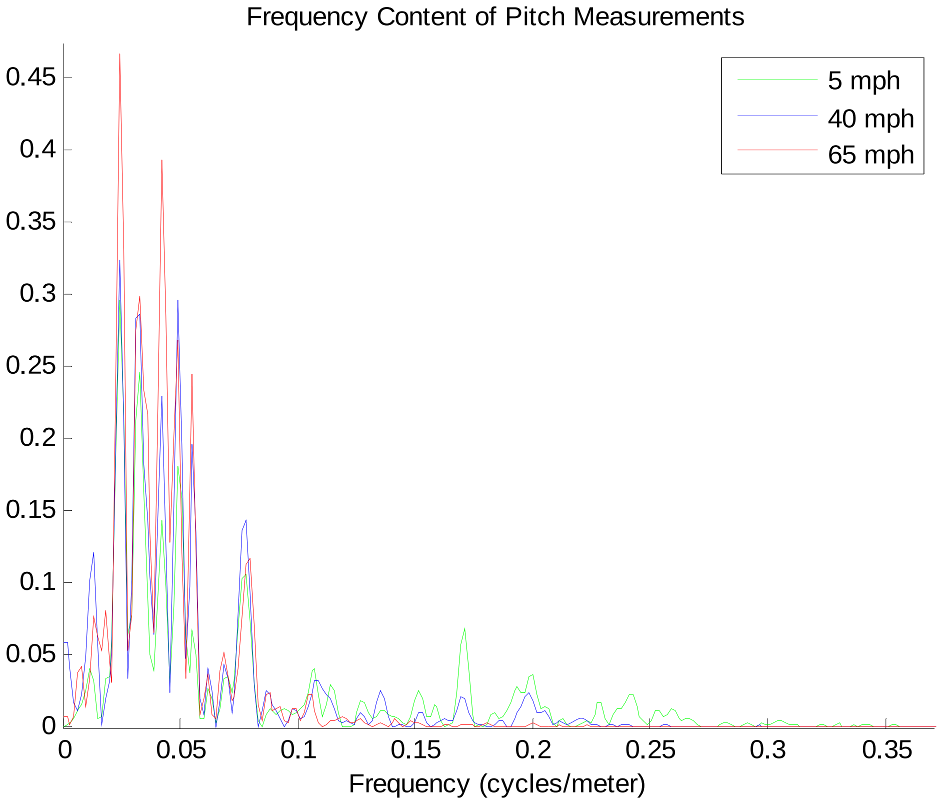

Figure 8.12: Unfiltered Pitch Measurement - FFT

The above figure shows that the low-speed data has a higher power density at high frequency than does the high-speed data. Conversely, the high speed data has higher power density at low frequencies than the low speed data. This division occurs at approximately 0.1 cycles/meter. This is shift in the signal's frequency content directly demonstrates the suspension's speed dependent low-pass filtering effects.

Another interesting observation from the above FFT is the obvious similarity between the low-frequency content of the signals. This low-frequency content is precisely what is sought after for the correlation routine. In order to remove the unwanted high frequencies, an additional low-pass spatial filter with a cutoff frequency of 0.1 cycles/meter is applied to the to the pitch measurements. The unfiltered and filtered pitch measurements are shown in Figure 8.13:

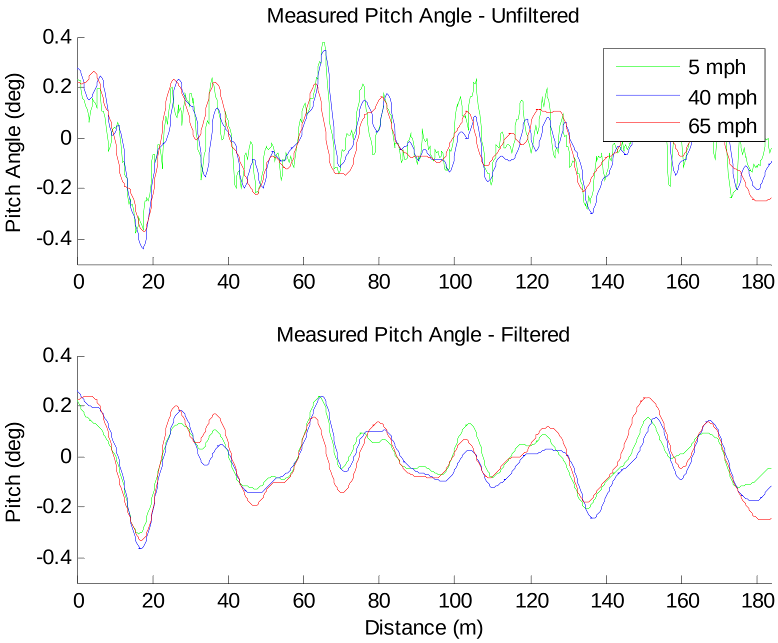

Figure 8.13: Unfiltered and Filtered Pitch Measurements

Figure 8.13 shows that the low-frequency portion of the vehicle's pitch measurements exhibits little variation with large variations of speed. This indicates that this signal is well suited for use in a localization routine for this vehicle.

8.6 Results Discussion

This chapter has shown that road grade estimates can be obtained from the low-frequency content of a vehicle's pitch measurement. These estimates can be correlated with a road grade map as a localization routine. For the test vehicle and data used in this study, the low-frequency portion of the pitch measurements did not vary significantly with speed when plotted against distance traveled. This indicates that the low-frequency content of the pitch measurements is caused by changes in terrain and therefore can be used as an estimate of road grade.

In order to implement this routine in practice, all vehicles should be able to use a single high-precision map for their correlation routines so that manufacturers do not have to generate a map for all major roads and for all vehicles. This type of positioning routine is demonstrated below:

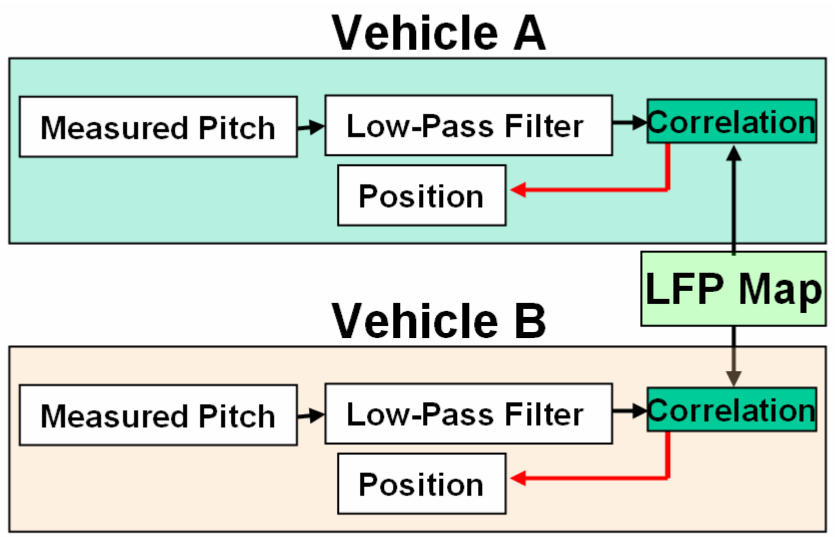

Figure 8.14: Implementation Diagram – Low Pass Filter

The routine presented in Figure 8.14 would only be appropriate if the low-frequency pitch content of all vehicles was the same for a given road profile. However, since the mass distribution and suspension parameters will vary from vehicle to vehicle, the same road profile will not cause the same pitch measurements across different vehicle models. Although the road grade estimates for the test vehicle in this work did not vary with speed, this will not be the case for all vehicles. In the next chapter this will be shown in simulation.

In order for a single map to be used for all vehicles, this positioning routine must include a vehicle model that accounts for pitch-plane dynamics. By inverting the pitch-plane model, the vehicle dynamics can be removed from the pitch readings and more accurate road grade estimations can be made that are independent of the vehicle and its velocity. A more realistic implementation routine is given in Figure 8.15.

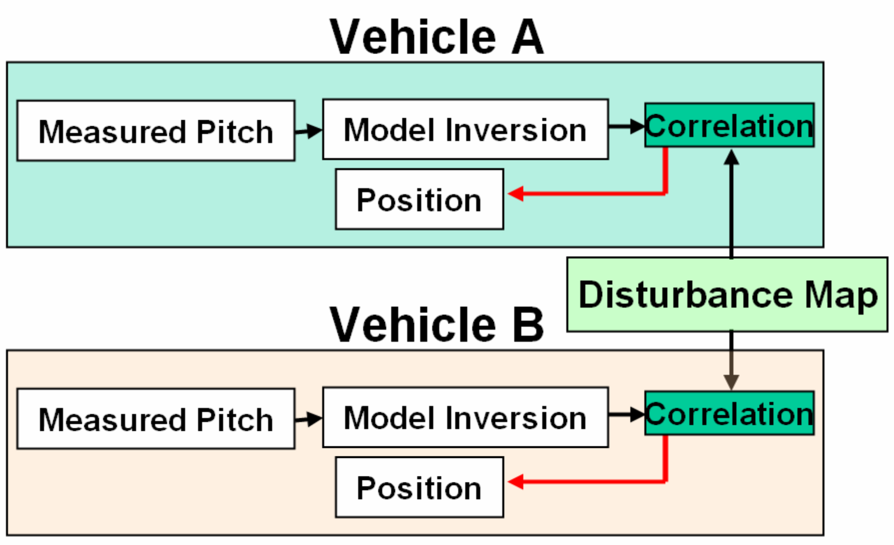

Figure 8.15: Implementation Diagram – Model Inversion

In the next chapter several pitch-plane models are derived. These models are then used in conjunction with an inversion technique for a better estimate of the true road grade, one which is independent of the vehicle setup and its speed.

8.7 Conclusions

- The repeatability and location based nature of road grade estimates has been shown
- Experimental results have been given to prove the concept of road grade based positioning
- For the test vehicle used here, the low frequency content of the pitch measurements showed only small variation with large variations of speed.
- In order to obtain road grade estimates which are independent of vehicle setup and speed, investigation an into pitch-plane model inversions is needed.

1. Ryu, J., E.J. Rossetter, and J.C. Gerdes. *Vehicle Sideslip and Roll Parameter Estimation using GPS*. in *AVEC 2002: 6th International Symposium on Advanced Vehicle Control*. 2002. Hiroshima, Japan.
2. Ryu, J. and J.C. Gerdes. *Estimation Of Vehicle Roll And Road Bank Angle*. 2004. Boston, Massachusetts.
3. Vahidi, A., A. Stefanopoulou, and H. Peng. *Experiments for Online Estimation of Heavy Vehicle's Mass and Time-Varying Road Grade*. in *Proceeding sof IMECE DSCD 2003*. 2003.
4. Vahidi, A., A. Stefanopoulou, and H. Peng, *Recursive Least Squares with Forgetting for Online Estimatoin of Vehicle Mass and Road Grade:Theory and Experiments.* Journal of Vehicle System Dynamics, 2005(43): p. 31-57.
5. Bae, H.S., J. Ryu, and J.C. Gerdes. *Road Grade and Vehicle Parameter Estimation for Longitudinal Control Using GPS*. in *Proceeings of IEEE Conference on Intelligent Transportation Systems*. 2001.
6. Sharp, R.S., *Wheelbase filtering and Automobiel Suspension Tuning for Minimising Motions in Pitch.* Journal of Automobiel Engineering, 2002. **216**(6): p. 933-946.

Chapter 9

Pitch Model Derivations and Implementation

In chapter 8, the concept of using road grade measurements for longitudinal positioning was introduced. The road grade was estimated by looking at the low frequency portion of the vehicle's pitch measurements. These measurements, however, will be dependent on the vehicle suspension characteristics and the vehicle's velocity. In order to extract the true road grade from the pitch measurements, a vehicle model must be included. If the model accurately represents the dynamics of the vehicle, then the calculated road grade measurements should be independent of both the vehicle speed as well as the vehicle recording the pitch measurements.

In this chapter several pitch plane models are developed. The models vary in complexity from a simple kinematic model to a full pitch-plane dynamic model. In order to test these models, vehicle parameters such as the front and rear spring stiffnesses and damping coefficients must be estimated. A method to perform this estimation is presented in this chapter.

The differences between these models are then investigated and an attempt is made to use each of these models to extract the true road grade from the pitch measurements. These are compared across different velocities to determine repeatability of the road grade estimate as a function of speed.

9.1 Free Body Diagram and Assumptions

Figure 9.1 shows the free-body-diagram of the pitch-plane model used in this chapter. Each version of model presented in this chapter will utilize the same base set of assumptions. These models will then vary in complexity by applying additional simplifying assumptions.

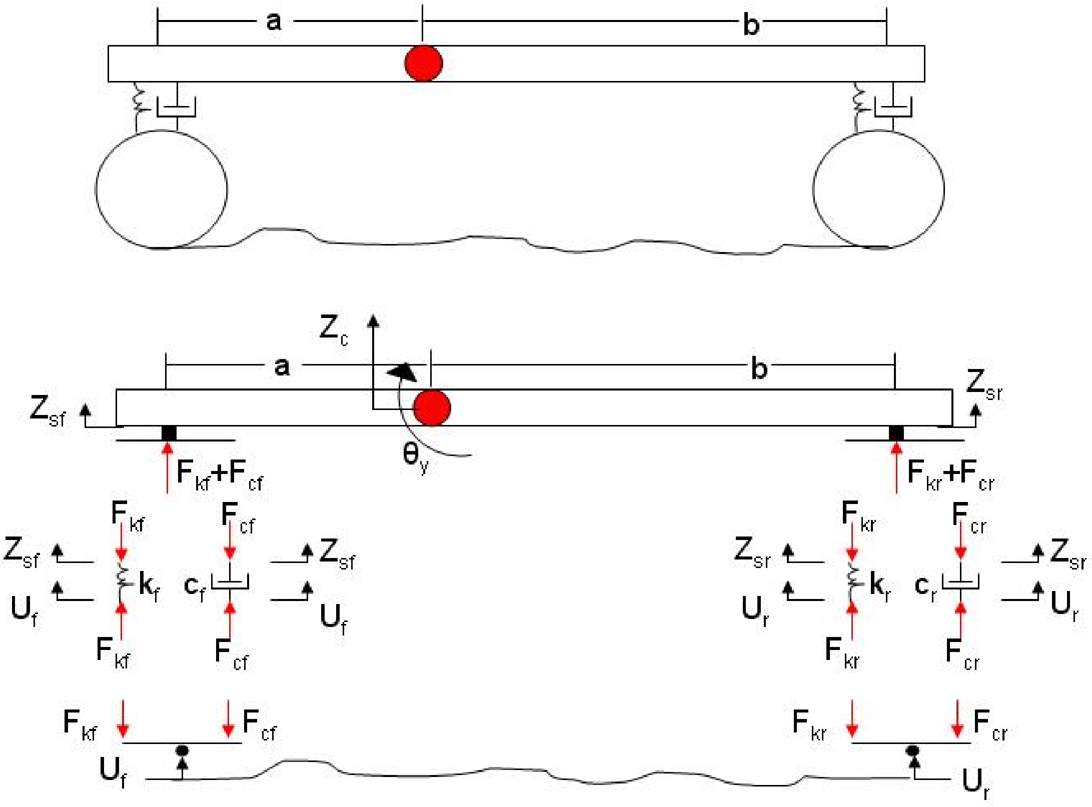

Figure 9.1: Pitch Plane Model – Free Body Diagram

The notation is as follows:

Table 9.1: Pitch Model Parameter Definitions

Symbol	Parameter	Symbol	Parameter
Z_{sf}	Vertical Displacement of Front Sprung Mass	F_{kf}	Force Due to Front Spring Deflection
Z_{sr}	Vertical Displacement of Rear Sprung Mass	F_{kr}	Force Due to Rear Spring Deflection
Z_c	Vertical Displacement of Center of Gravity	F_{cf}	Front Damping Force
θ	Vehicle Pitch Angle	F_{cr}	Rear Damping Force
U_f	Front Road Disturbance Input	a	CG to Front Axle Distance
U_r	Rear Road Disturbance Input	b	CG to Rear Axle Distance
k_f	Front Spring Stiffness		
k_r	Rear Spring Stiffness		
c_f	Front Damping Coefficient		
c_r	Rear Damping Coefficient		

Each model in this chapter will be derived with the following assumptions:

- The un-sprung mass (wheels, tires, etc) is neglected
- The vehicle pitch angle is measured at the center of gravity
- The suspension forces generated are due to the front and rear road disturbances U_f and U_r
- The front and rear suspension forces act on the vehicle body at locations a and b respectively Figure 9.1
- The road disturbance at the rear of the vehicle, U_r, is a time-delayed version of the disturbance acting at the front of the vehicle, U_f

9.2 Model 1 – Kinematic Model

The simplest version of pitch plane model neglects suspension forces altogether. The result is a kinematic model which implies that the road disturbance directly acts on the vehicle chassis. This system can be represented pictorially with the following block diagram:

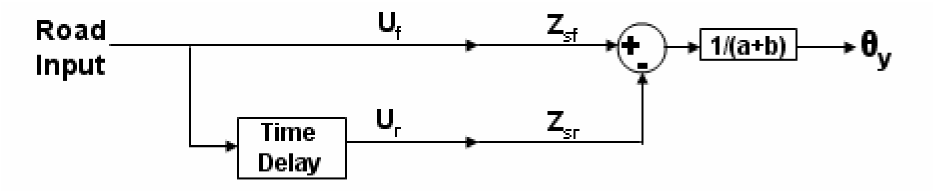

Figure 9.2: Kinematic Model – Block Diagram

As indicted in the figure, the front and rear sprung mass vertical displacements are equal to their respective road inputs.

$$Z_{sr} = U_r \qquad \textbf{9.1}$$
$$Z_{sf} = U_f$$

Expressions relating the front and rear sprung mass vertical displacements to the vertical displacement at the center of gravity can be written directly from the kinematics of the free-body-diagram of Figure 9.1.

$$Z_{sf} = Z_c + a\theta_y \qquad \textbf{9.2}$$
$$Z_{sr} = Z_c - b\theta_y$$

Solving for Z_c and rearranging these two equations leads to:

$$Z_{sf} - Z_{sr} = \theta_y \cdot (a+b) \qquad \textbf{9.3}$$

Combining Equations 9.3 and 9.1:

$$U_f - U_r = \theta_y \cdot (a+b) \qquad \textbf{9.4}$$

During forward motion, the sensor measuring the pitch angle is located behind the vehicle's front axle. Therefore the front road disturbance, U_f occurs before (in time) the sensor reaches the location of that disturbance. Since the initial rear disturbance is unknown, it is not possible to predict the road disturbance at the front with only the pitch measurement. The user can, however, measure and predict the rear road disturbance inputs because the same disturbance has acted on the front tires in an earlier time interval. Therefore, the goal of this mathematical analysis will be to extract an estimate of the rear displacement using current and past pitch measurements.

The base assumptions state that the rear input, U_r, is a time-delayed version of the front disturbance U_f, therefore:

$$U_r(t) = U_f(t+\tau) \qquad \textbf{9.5}$$

where τ is the time delay between front and rear inputs that can be estimated using the vehicle's length and assumption of constant velocity:

$$\tau \approx \frac{(a+b)}{U} \qquad \textbf{9.6}$$

In the Laplace domain, equation **9.4** can be expressed as:

$$U_r(s) = U_f(s) \cdot e^{-s\tau} \qquad \textbf{9.7}$$

For simulation purposes, it is convenient to replace the $e^{-s\tau}$ in the above equation with a rational polynomial which estimates the same time delay. This can be done through the Padé approximation. The n$^{\text{th}}$ order Padé approximation is shown in [1] as:

$$e^{-\tau s} \approx P_d(s) = \frac{N_d(s)}{D_d(s)} = \frac{\sum_{k=0}^{n} (-1)^k c_k h^k s^k}{\sum_{k=0}^{n} c_k h^k s^k} \qquad \textbf{9.8}$$

Where the coefficients are:

$$c_k = \frac{(2n-k)! \cdot n!}{2n! \cdot k! \cdot (n-k)!}, k = 0,1,\ldots,n \qquad \textbf{9.9}$$

For this work, a second order Padé approximation was used. The justification for this can be found in Appendix A. This approximation is given as:

$$P_d(s) = \frac{(\tau \cdot s)^2 - 6\tau \cdot s + 12}{(\tau \cdot s)^2 + 6\tau \cdot s + 12} \qquad \textbf{9.10}$$

To simplify the algebra, equation **9.10** will be replaced with:

$$P_d(s) = \frac{n_1 s^2 - n_2 s + n_3}{n_1 s^2 + n_2 s + n_3} \qquad \textbf{9.11}$$

Equation **9.7** can be solved for U_f and combined with **9.10**:

$$U_f(s) = U_r(s) \cdot P_d^{-1}(s) \tag{9.12}$$

Taking the Laplace transform of equation 9.4 and combining it with equation 9.12:

$$U_r(s) \cdot P_d^{-1}(s) - U_r(s) = \theta_y(s) \cdot (a+b) \tag{9.13}$$

Equation 9.13 can then be solved for the transfer function between θ_y and U_r:

$$\frac{\theta_y(s)}{U_r(s)} = \frac{(P_d^{-1}(s) - 1)}{(a+b)} \tag{9.14}$$

Combining equation 9.14 with equation 9.11 and simplifying leads to:

$$\frac{\theta_y(s)}{U_r(s)} = \frac{2 \cdot n_2 s}{(a+b) \cdot \left(n_1 s^2 - n_2 s + n_3\right)} \tag{9.15}$$

Equation 9.15 is the transfer function which relates the pitch angle measured at the center of gravity to the road disturbance input at the rear wheels for the Kinematic model.

In order to compare each of the models derived in this chapter once can look at each model's frequency response. The frequency response for the Kinematic Model given by equation 9.15 for a vehicle moving at 25 mph is shown below:

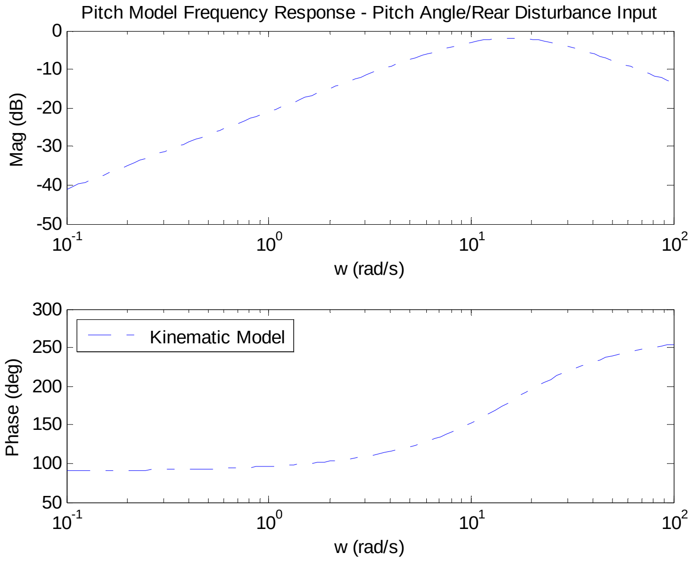

Figure 9.3: Kinematic Model – Frequency Response

Further insight into the inversion problem can be shown through inspection of equation 9.15. At low frequencies, the denominator of equation 9.15 will be dominated by the n_3 term. The resulting expression becomes:

$$\frac{\theta_y(s)}{U_r(s)} \approx \frac{2 \cdot n_2 s}{(a+b) \cdot n_3} \qquad 9.16$$

This shows that that θ_y is related to U_r through a derivative function. Intuitively this makes sense because in the limiting case where vehicle's wheel base decreases to zero, the pitch angle measured at the center of gravity converges to the angle of the line tangent to the road profile below the center of gravity. This is represented pictorially in Figure 9.4:

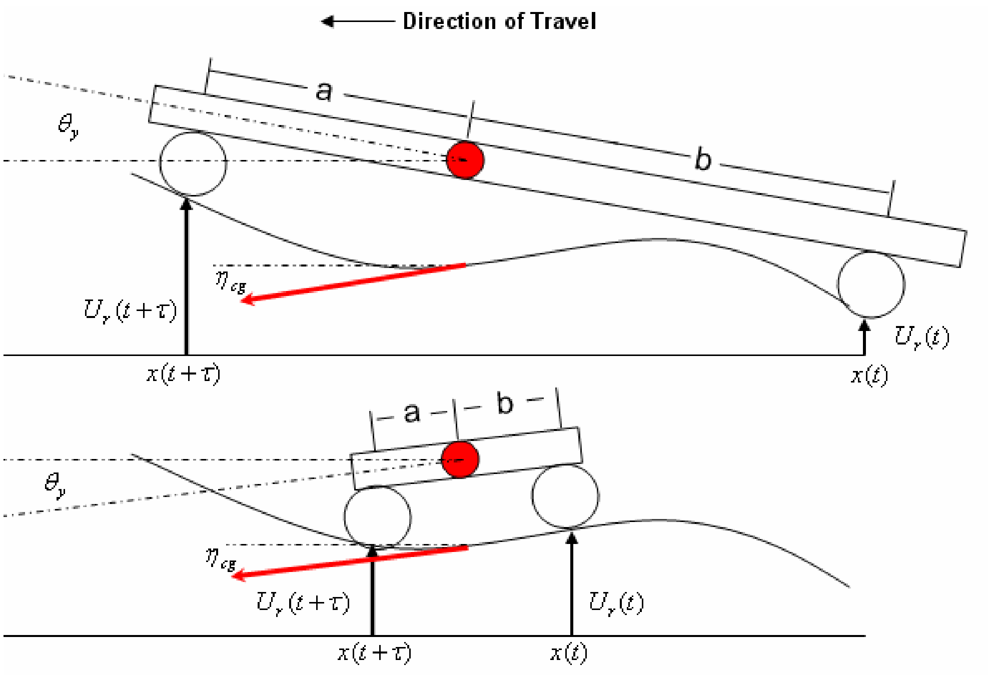

Figure 9.4: Effect of Decreasing Wheelbase

The slope of the angle of the tangent line below the CG, η_{cg}, is simply ratio of the change in profile height over distance covered:

$$\eta_{cg} = \frac{U_r(t+\tau) - U_r(t)}{x(t+\tau) - x(t)} = \frac{dU_r}{dx} \approx \theta_y \qquad 9.17$$

Since this angle is simply the derivative of the road disturbance with respect to distance, one would expect a similar derivative relationship to appear in the transfer function between the pitch angle and rear road disturbance.

In order to extract the rear road disturbance input from the vehicle's pitch measurements, equation 9.15 can be inverted:

$$\frac{U_r(s)}{\theta_y(s)} = \frac{(a+b)\cdot\left(n_1 s^2 - n_2 s + n_3\right)}{2\cdot n_2 s} \qquad 9.18$$

This transfer function is not causal, and therefore its behavior cannot be simulated in standard software such as MATLAB's Simulink. In order to correct this, a pole can be added to the transfer function. The added pole must be considerably faster than the poles of the current system so its dynamics will not greatly influence the system behavior. For this equation, only one pole is needed to make the function causal. This pole is added at p_1 by multiplying the denominator by $(s+p_1)$ and rescaling the numerator by a factor of p_1 as shown below:

$$\frac{U_r(s)}{\theta_y(s)} = (a+b)\cdot\frac{p_1\cdot\left(n_1s^2 - n_2s + n_3\right)}{(s+p_1)\cdot(2\cdot n_2s)} \qquad 9.19$$

When expanded this becomes:

$$\frac{U_r(s)}{\theta_y(s)} = (a+b)\cdot\frac{p_1n_1s^2 - p_1n_2s + p_1n_3}{2\cdot n_2s^2 + 2\cdot p_1n_2s} \qquad 9.20$$

This transfer function is now causal, and can be easily simulated in MATLAB. Care must be taken to ensure the pole at p_1 does not greatly affect the response.

9.3 Model 2 – Identical Suspensions, No Rotational Inertia

As an initial approximation of suspension behavior, the front and rear suspensions can be assumed to be identical. If the rotational inertia of the vehicle is neglected, the model in Figure 9.1 reduces to two identical quarter-car models. The pitch angle can then be calculated from the kinematic formulation in equation 9.15. This system can be seen pictorially in the following block diagram:

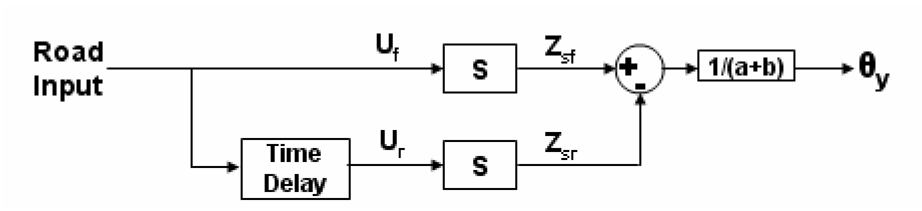

Figure 9.5: Identical Suspension Model – Block Diagram

Where the blocks labeled ***S*** represent the transfer function which relates the road disturbance to the vertical displacement of the sprung mass. These transfer functions can be derived from a simple mass-spring-damper system known as the quarter-car model. Its Free Body Diagram is given in Figure 9.6:

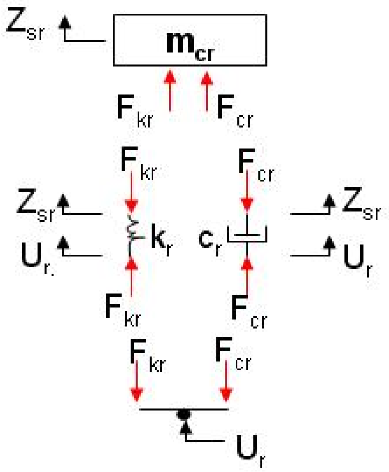

Figure 9.6: Quarter Car Model – Free Body Diagram

Using Newtonian mechanics, the equations of motion of the quarter car can be written. The spring and damper forces are:

$$F_{kr} = -k_r(z_{sr} - U_r)$$
$$F_{cr} = -c_r(\dot{z}_{sr} - \dot{U}_r) \qquad 9.21$$

Summing forces on the chassis in the vertical direction:

$$-k_r(z_{sr} - U_r) - c_r(\dot{z}_{sr} - \dot{U}_r) = m_{cr}\ddot{z}_{sr} \qquad 9.22$$

Taking the Laplace transform of equation 9.22

$$-k_r z_{sr}(s) + k_r U_r(s) - s \cdot c_r z_{sr}(s) + s \cdot c_r U_r(s) = s^2 \cdot m_{cr} z_{sr}(s) \qquad 9.23$$

Equation 9.23 can be rearranged to solve for the transfer function relating the vertical displacement of the sprung mass to the road disturbance:

$$\frac{Z_{sr}(s)}{U_r(s)} = \frac{c_r s + k_r}{m_{cr}s^2 + c_r s + k_r} \qquad 9.24$$

Equation 9.24 can be combined with the results of the Kinematic model to relate the pitch angle to the rear road disturbance for the Identical Suspension model:

$$\frac{\theta_y(s)}{U_r(s)} = \frac{\theta_y(s)}{Z_{sr}(s)} \cdot \frac{Z_{sr}(s)}{U_r(s)} = \frac{2 \cdot n_2 s}{(a+b) \cdot \left(n_1 s^2 - n_2 s + n_3\right)} \cdot \frac{c_r s + k_r}{m_{cr} s^2 + c_r s + k_r}$$

$$= \frac{2 \cdot n_2 c_f s^2 + 2 \cdot n_2 k_r s}{(a+b) \cdot \left((n_1 m_{cr}) \cdot s^4 + \left(n_1 c_r - n_2 m_{cr}\right) \cdot s^3 + (n_1 k_r - n_2 c_r + n_3 m_{cr}) \cdot s^2 + (n_3 c_r - n_2 k_r) \cdot s + n_3 k_r\right)} \qquad 9.25$$

Again, a comparison between models can be made by looking at the frequency response of each system. For a vehicle traveling at 25 mph, the frequency response is as follows:

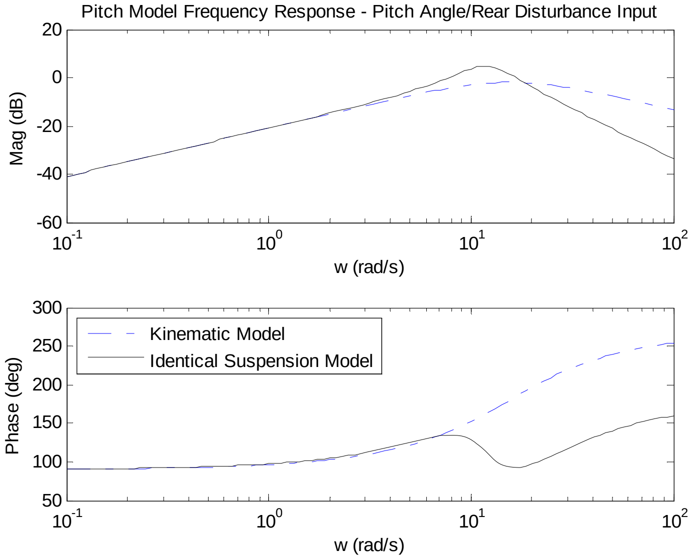

Figure 9.7: Identical Suspension Model – Frequency Response

(NOTE: To generate this frequency response an estimation of the vehicle's suspension parameters was made. This is discussed further in section 9.5.)

By examining Figure 9.7, it can be seen that at very low frequencies, the Identical Suspension Model reduces to the Kinematic Model. At frequencies higher than 3 rad/s, the effects of suspension dynamics become apparent.

As before equation 9.25 can be inverted to extract U_r from θ_y:

$$\frac{U_r(s)}{\theta_y(s)} = \frac{(a+b)\cdot\left((n_1 m_{cr})\cdot s^4 + \left(n_1 c_r - n_2 m_{cr}\right)\cdot s^3\right)}{2\cdot n_2 c_f s^2 + 2\cdot n_2 k_r s} + \frac{(a+b)\cdot\left((n_1 k_r - n_2 c_r + n_3 m_{cr})\cdot s^2 + (n_3 c_r - n_2 k_r)\cdot s + n_3 k_r\right)}{2\cdot n_2 c_f s^2 + 2\cdot n_2 k_r s} \quad 9.26$$

Once again the transfer function is not causal. In the single suspension model, two poles must be added. The details of this will not be presented here, but can be found in Appendix A.

9.4 Additional Suspension Models

In addition to Models 1 and 2 presented in the previous two sections, two more complex suspension models have also been derived for this work. The third model, Model 3, is similar to Model 2 in that treats the vehicle as two quarter car models, however Model 3 allows each of the front and rear suspensions to have different parameters. The fourth model is a “Full Pitch Plane” model. This model accounts for different suspension dynamics in the front and rear, and also considers the rotational inertia of the vehicle.

After the suspension parameters were determined, it was found that the inverted versions of Model 3 and 4 had unstable poles in the denominator. Because of this, they were not used in simulation, and therefore will not be presented in this chapter. However, the full derivations of each of these models along with discussions of each are given in Appendix A.

9.5 Suspension Parameter Estimation

In order to test the models presented in the previous sections, the vehicle’s suspension characteristics must be determined. Since the Tracer’s spring stiffnesses and damping coefficients are not readily available in literature, a method of estimating these parameters is presented here.

9.5.1 Spring Stiffness Estimation

In order to estimate the spring stiffnesses, the following procedure was followed:

1. Place a scale under each of the front tires
2. Position a floor jack to the center of the front axle
3. Raise the vehicle until the scales read 100 lbs less than the current reading
4. Measure and record the distance from the hub center to the fender
5. Repeat Steps 3-4 until a sufficient number of data points have been collected
6. Plot the additional force (from the initial value at rest) versus the spring displacement from rest.
7. The slope of the best fit line of the force versus displacement curve corresponds to the spring stiffness constant.

The measurements have been summarized in Table 9.2.

Table 9.2: Spring Deflection Measurements

Drivers Front		Passenger Front	
Force (N)	Distance (m)	Force (N)	Distance (m)
3113	0.371	3114	0.362
2669	0.385	2669	0.379
2224	0.403	2224	0.397
1668	0.423	1779	0.414
889	0.441	890	0.438
Drivers Rear		Passenger Rear	
Force (N)	Distance (m)	Force (N)	Distance (m)
2002	0.349	2002	0.351
1334	0.368	1446	0.368
667	0.408	778	0.403
0	0.424	0	0.425

With the hub center to fender distances and the corresponding force readings of the scales, the spring constants can be determined by:

$$k = -\frac{F}{dx} \qquad 9.27$$

Where *k* is the spring constant and *dx* is the spring deflection. This process was performed for both the front and rear springs. Figure 9.8 shows the resulting plots of the additional force (from the initial value at rest) versus the spring displacement from rest.

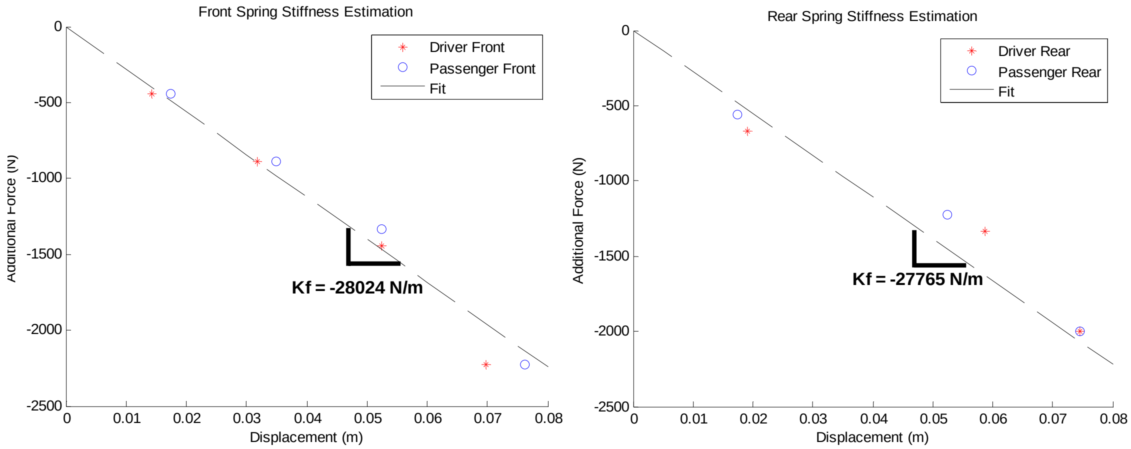

Figure 9.8: Spring Stiffness Fits

The average per-axle spring stiffness values were determined to be:

$$k_f = -56048 \frac{N}{m}$$
$$k_r = -55530 \frac{N}{m} \qquad 9.28$$

9.5.2 Damping Coefficient Estimation

The front and rear spring stiffness values determined in the previous section were then used in a model fitting routine to determine the front and rear damping coefficients. The procedure was similar to that used in [2] to determine the roll stiffness and damping. The procedure is outlined here:

1. Start the vehicle on a flat surface with the GPS/INS system measuring pitch angle
2. Forcibly oscillate the vehicle in the vertical direction at the front axle. Continue the forced oscillation until the system reaches an approximate steady state response to the sinusoidal input.
3. Terminate force input and allow the vehicle to come to rest.

4. Plot the vertical displacements at axle with the free response of the quarter car model.
5. Vary the damping coefficient value until the best model match is achieved
6. Repeat steps 1-4 for rear axle.

For the experiment outlined above, it can be assumed that the vehicle rotates about the axle which is not being oscillated, e.g. for the front suspension oscillation, the vehicle rotates about the rear axle. It is also assumed that the forced oscillations cause no vertical motion at the opposing suspension. This is shown for the front oscillation in Figure 9.9

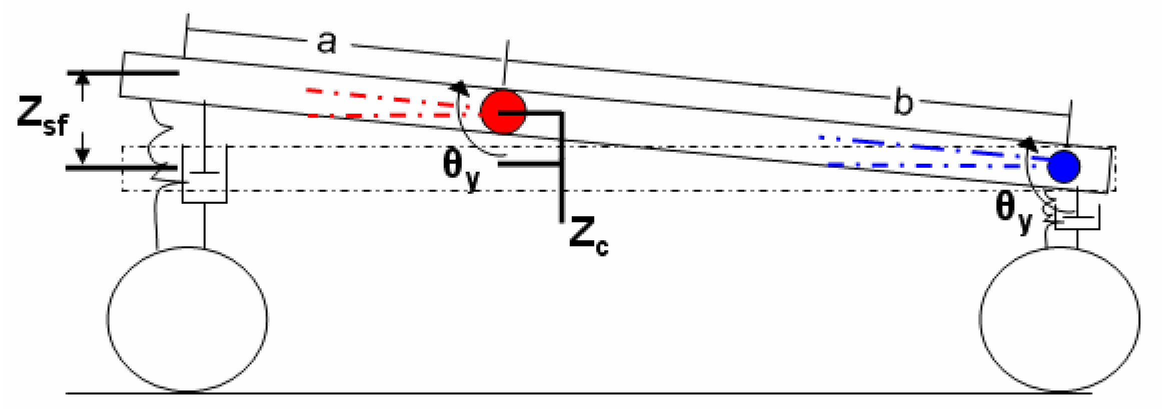

Figure 9.9: Front Oscillation Diagram

With the assumptions listed above, the pitch angle which is measured at the center of gravity is equal to the angle the vehicle makes with respect to the horizontal measured at the rear rotation point. Therefore from inspection of the figure, and by assuming small angles the equation relating Z_{sf} to the pitch angle can be written

$$Z_{sf} = (a+b)\cdot\theta_y \qquad 9.29$$

Similarly for the rear:

$$Z_{sr} = -(a+b)\cdot\theta_y \qquad 9.30$$

To ensure the above assumptions are valid, the vertical displacement at the CG was also recorded during the experiment using the DGPS system. With the previously mentioned assumptions, this vertical displacement is related to the pitch angle by:

$$Z_{cg} = b \cdot \theta_y \qquad \mathbf{9.31}$$

The measured vertical displacement at the CG and the estimated displacement from equation 9.31 are plotted together in Figure 9.10:

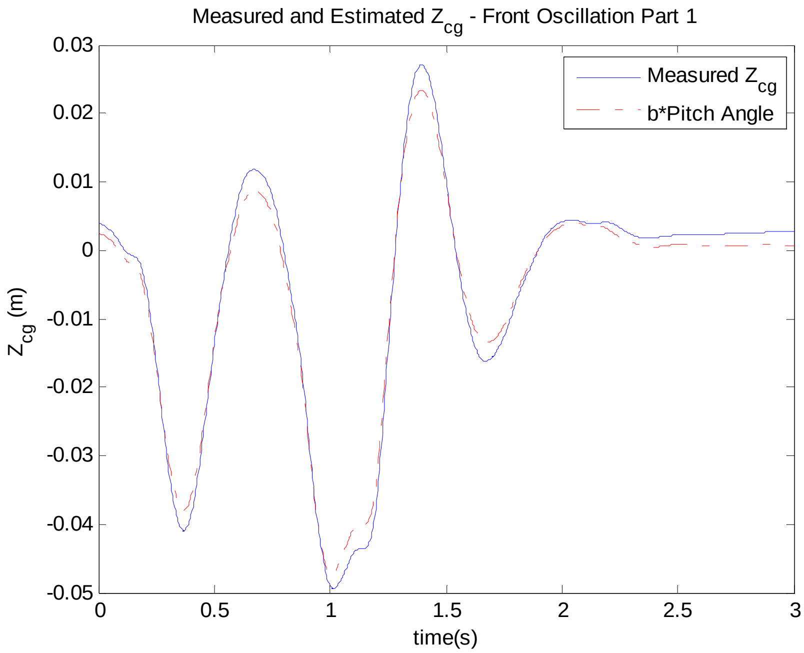

Figure 9.10: Measured and Estimated Vertical Displacement at CG

This figure shows that the assumptions used for this experiment are valid.

The front and rear vertical displacement values calculated from equations 9.29 and 9.30 were compared to those predicted by the free response of the quarter car model. The free-body-diagram for the quarter car model with a road disturbance input was given in Figure 9.6. The free response of the system at the front axle is determined by:

$$m_{cf}\ddot{z}_{sf} + c_f\dot{z}_{sf} + k_f z_{sf} = 0 \qquad \mathbf{9.32}$$

This system was simulated in MATLAB's Simlink using the following block diagram:

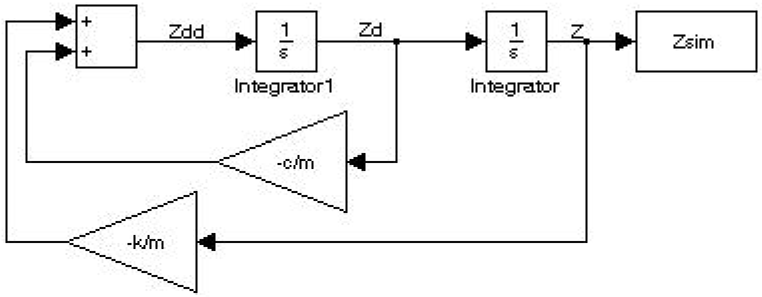

Figure 9.11: Quarter Car Model – Simulink Diagram

Where the initial conditions for the vertical velocity, $\dot{z}_{sf}$, and vertical position, z_{sf} , were extracted from the collected data. An example of the sample data collection and model matching is shown below in Figure 9.12

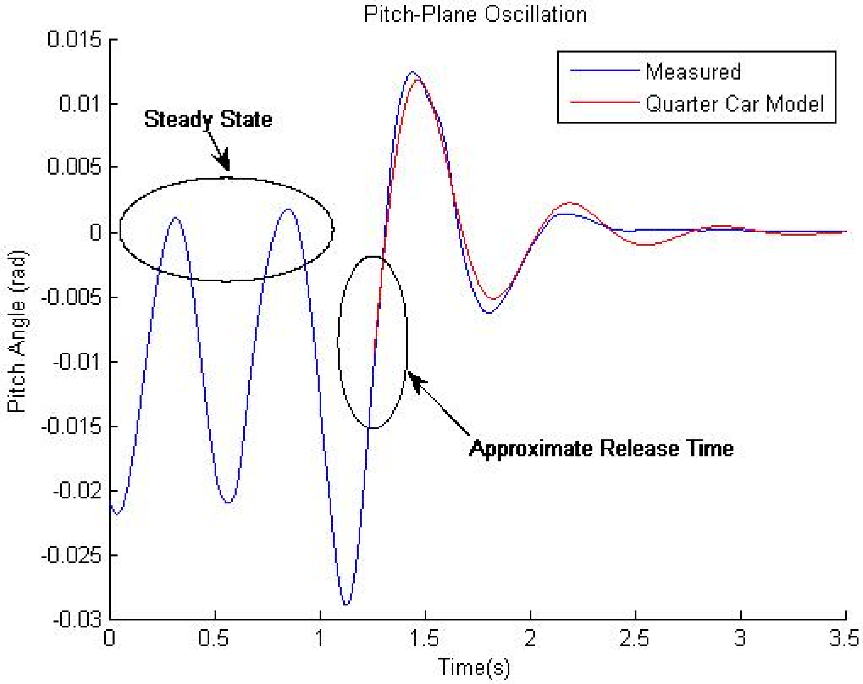

Figure 9.12: Example Pitch-Plane Excitation

In the model fitting routine the damping value was allowed to vary while the spring stiffness values remained constant. The fit which minimized the root-mean-square error between the simulated and measured displacements was chosen to be the best fit. The best model fits for the three data sets for the front and rear are shown in Figure 9.13

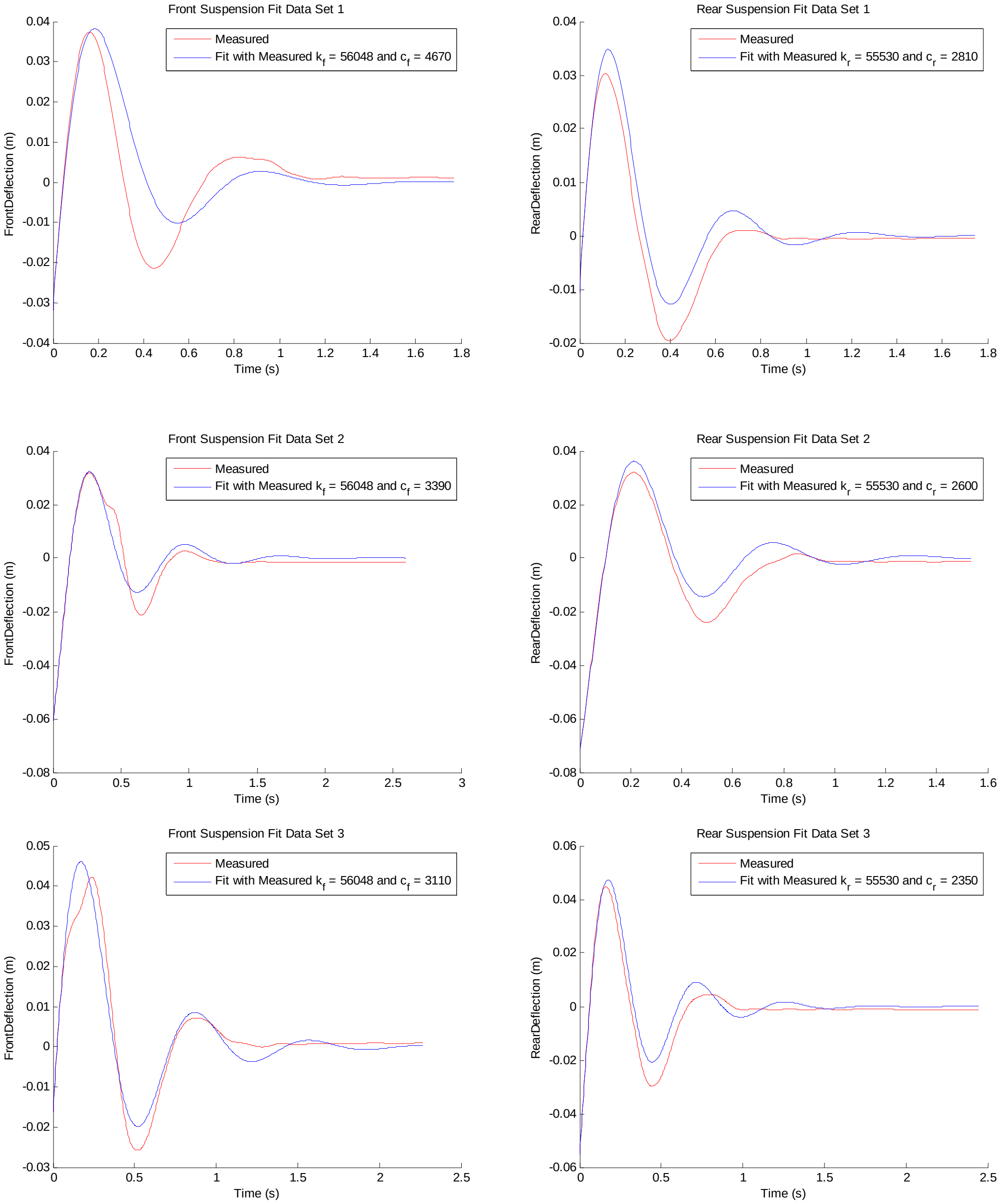

Figure 9.13: Quarter Car Model Fits

The final per-axle damping values for the front and rear were determined to be:

$$c_f = 3723 \frac{N \cdot s}{m}$$
$$c_r = 2586 \frac{N \cdot s}{m} \quad 9.33$$

After reviewing the suspension parameters presented in 9.28 and 9.33, it can be seen that the front and rear suspension coefficients are similar, but not identical. There is also a considerable difference in the sprung mass that rests on each of these suspensions. However, for a first approximation, the Identical Suspension Model presented in Section 9.3 will be used to represent the test vehicle.

9.6 Effect of Forward Velocity on Pitch Measurements and Model Inversion

As a vehicle travels over a particular road profile, the frequency of the road disturbance input into the system will vary with the vehicle's forward velocity. Since the vehicle's suspension acts a low-pass filter, the vertical displacement of the sprung mass above the front and rear suspensions will also be a function of vehicle speed. Because the pitch angle is assumed to be kinematically related to the front and rear sprung mass displacements, the pitch angle measurements can also be expected to change as the vehicle velocity increases. This velocity-dependent change in pitch measurements will be determined directly from the vehicle's mass distribution and suspension characteristics.

With an accurate vehicle model and well known suspension parameters, the velocity *independent* road disturbance profile could be extracted from the velocity *dependent* pitch measurements. It should also be noted that if multiple vehicles had highly accurate suspension models, their road grade estimations would be identical after extraction of the dynamic influence of the suspension. Therefore, a single, high-accuracy road grade map could be used for all vehicles in their localization estimation.

These effects can easily be seen through simulation, shown in the next section.

9.6.1 Model 1 - Kinematic Model

Since the Kinematic Model does not account for the vehicle's suspension dynamics and the road disturbance is directly acting on the sprung mass, the pitch measurements should not vary as vehicle speed increases.

To simulate this, a signal was used as an example road profile which covered 200 meters with a spacing of 2.5 cm. This signal was then added to a time delayed version of itself where the time delay was proportional to the vehicle speed. By multiplying the resulting signal by *1/(a+b)* a pitch angle measurement was generated for a vehicle with no suspension. The block diagram for this can be seen in the figure below:

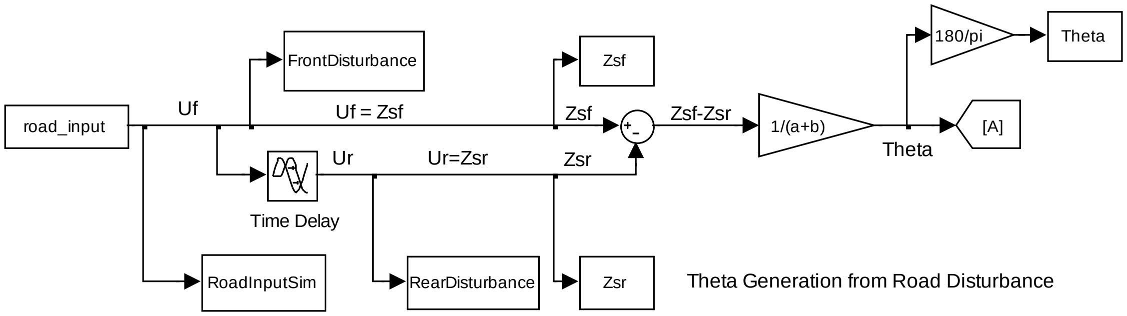

Figure 9.14: Kinematic Model Simulink Diagram - Pitch Generation

The simulated pitch angle can be viewed at different speeds by adjusting the simulation time parameters, step size and delay size. Figure 9.15 is a plot of the simulated road disturbance and sprung mass displacements for speeds of 5, 45 and 80 mph plotted against time.

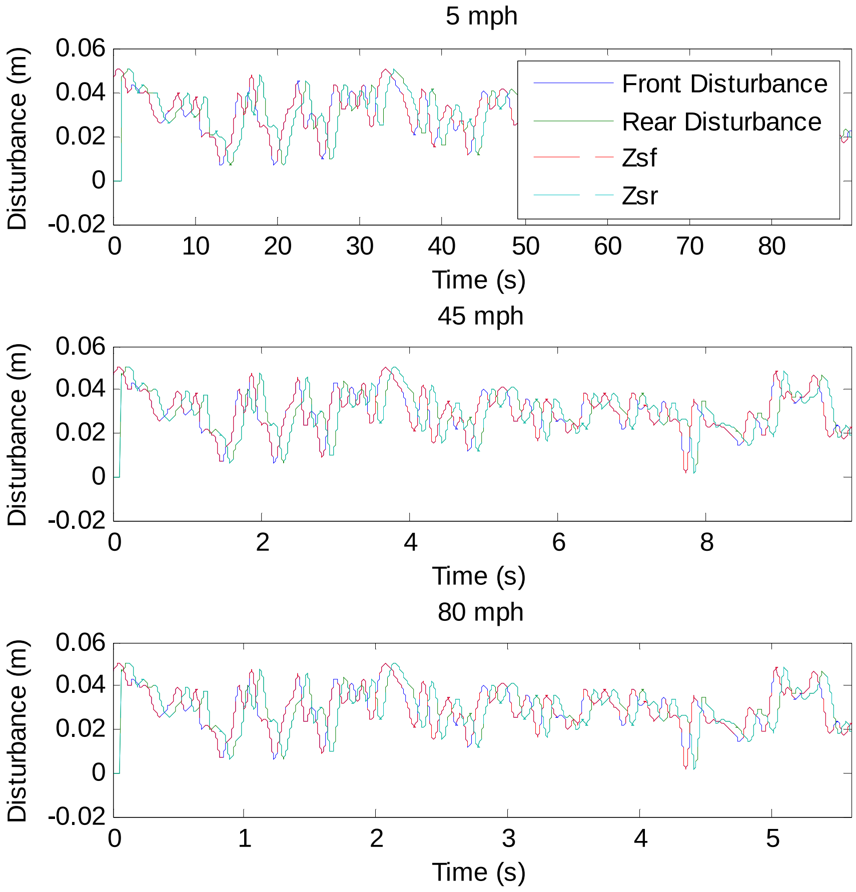

Figure 9.15: Kinematic Model Disturbance Plots

As expected, since there is no suspension the road disturbances in the front and rear are identical to the vertical displacement of the sprung mass at the front and rear.

Figure 9.16 is the plot of the resulting pitch angles as a function of distance traveled where the distance traveled was approximated by integrating the vehicle longitudinal velocity as a function of time.

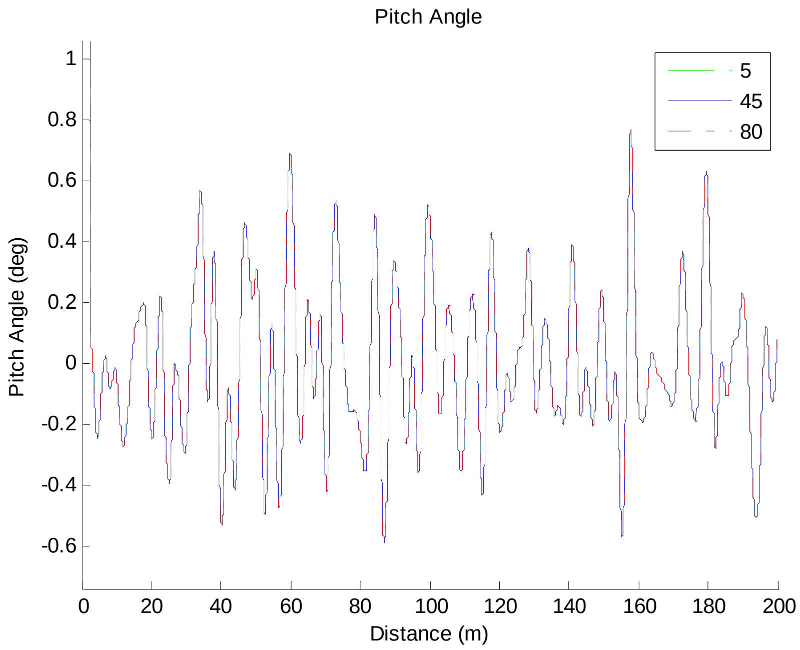

Figure 9.16: Kinematic Model – Generated Pitch

Figure 9.16 shows that the suspension-less vehicle will have the same pitch measurements (as a function of distance) regardless of forward velocity.

As a proof of concept, the inverted kinematic model given in equation 9.25 was simulated to ensure it correctly extracted the known rear input disturbance, U_r. The coefficients of the Padé approximation, *n1, n2,* and *n3*, were calculated for each vehicle speed. The inversion block diagram is shown in Figure 9.17:

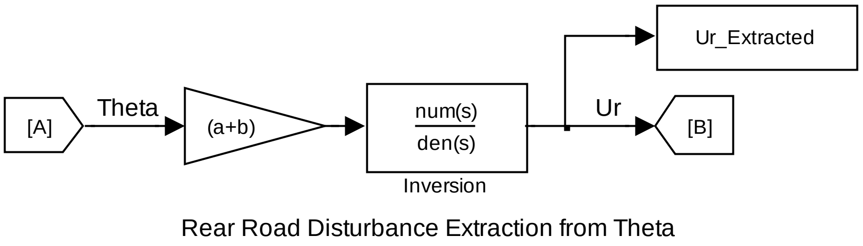

Figure 9.17: Kinematic Model Simulink Diagram – U_r Recovery

The U_r values recovered from the inversion are plotted with the original rear input disturbances in Figure **9.18**:

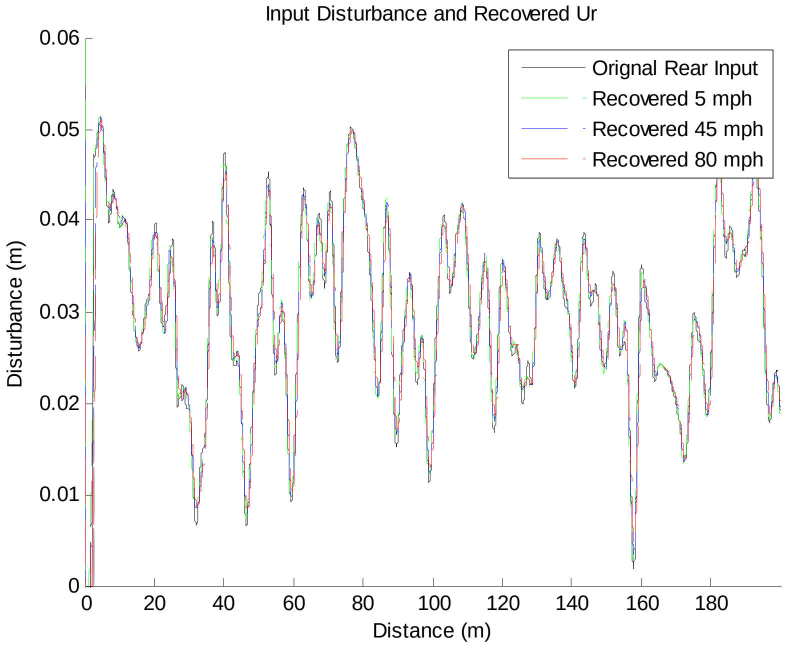

Figure **9.18**: Kinematic Model – Original Rear Input and Recovered U_r

Figure **9.18** clearly shows the success of the inversion process; however, this simple kinematic inversion does not represent the true behavior of the vehicle.

9.6.2 Model 2 - Identical Suspension Model

In the second model, the suspensions have been included; however, identical suspension parameters have been assumed for the front and rear. As discussed at the end of section **9.5.2**, this seems to be a reasonable initial approximation for the suspension current test vehicle. However it must be noted that the test vehicle's uneven mass distribution over the front and rear suspensions is in disagreement with this model.

The simulation of the Identical Suspension Model was similar to that of the Kinematic model. The same road input was used in the Kinematic model was used here. The

Simulink diagram for the generation of the pitch measurement is presented in Figure 9.19

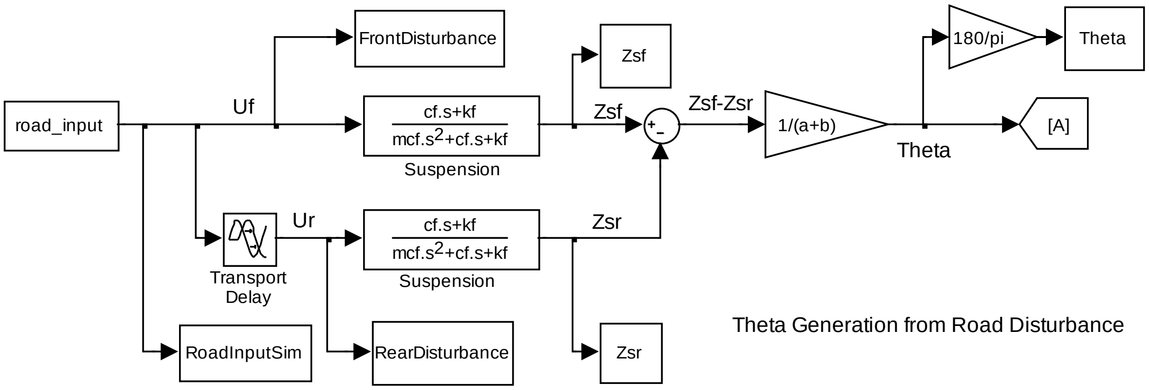

Figure 9.19: Identical Suspension Model Simulink Diagram – Pitch Generation

With the suspension blocks in place, the simulations performed for the Kinematic Model were repeated. Figure 9.20 shows a portion of the simulated vehicle pitch angles.

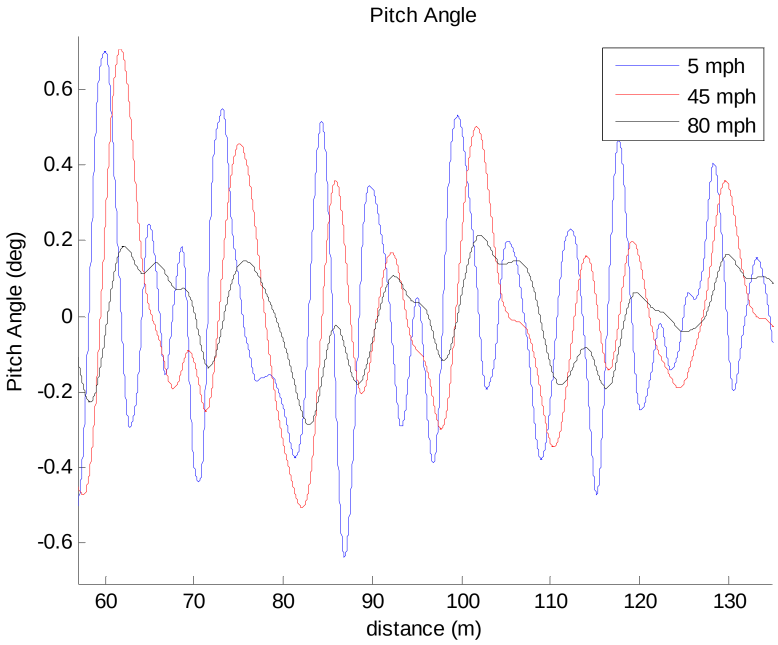

Figure 9.20: Identical Suspension Model – Generated Pitch

The previous plot shows that the vehicle's pitch angle for a given road profile will vary with speed. As the vehicle speed increases, the frequency of the input disturbance signal also increases. Since the suspension acts as a low-pass filter, the high frequencies of the road disturbance are filtered out which results in changes in the vehicle's pitch angle.

In Chapter 8, a low-pass spatial filter was applied to the raw pitch measurements to remove high frequency content of the signal. The cutoff frequency was chosen by looking at the FFT of the vehicle's pitch measurements. On the experimental data used in that chapter, there was a relatively obvious distinction between the high and low frequency content, and the cutoff frequency was chosen accordingly. When the FFT of the simulated pitch measurements is performed, the results are quite different:

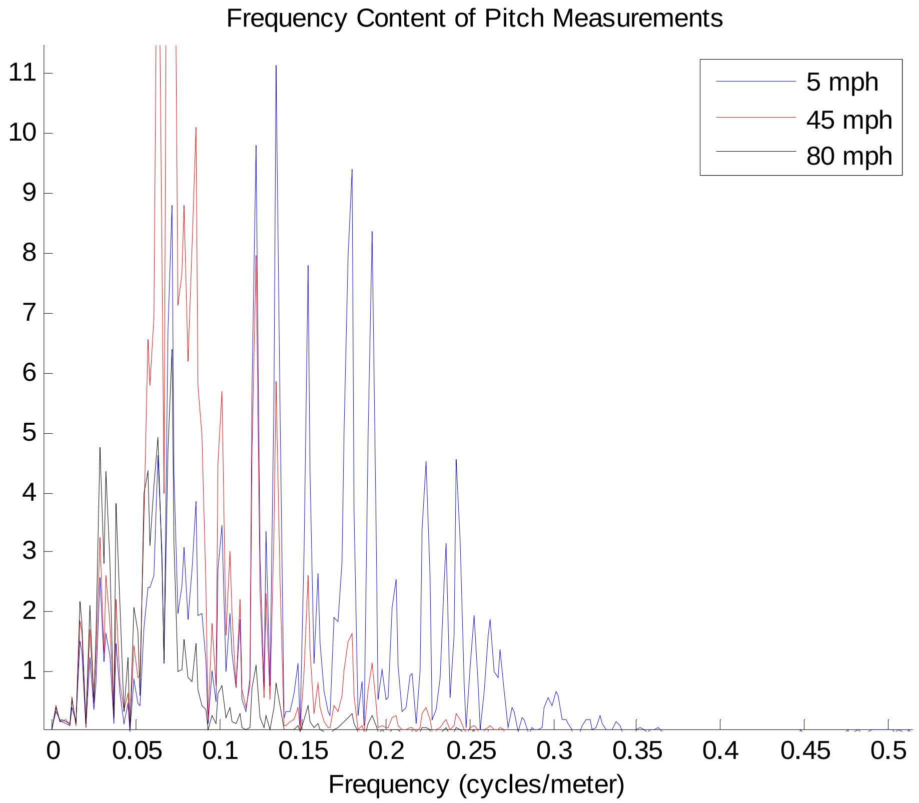

Figure 9.21: Simulated Pitch Measurements - FFT

In Figure 9.21 there no obvious frequency that can be used in a low-pass filter to make the low pitch measurements at different speeds fit for correlation. Because of this, the cutoff frequency was varied to see its effect on the data:

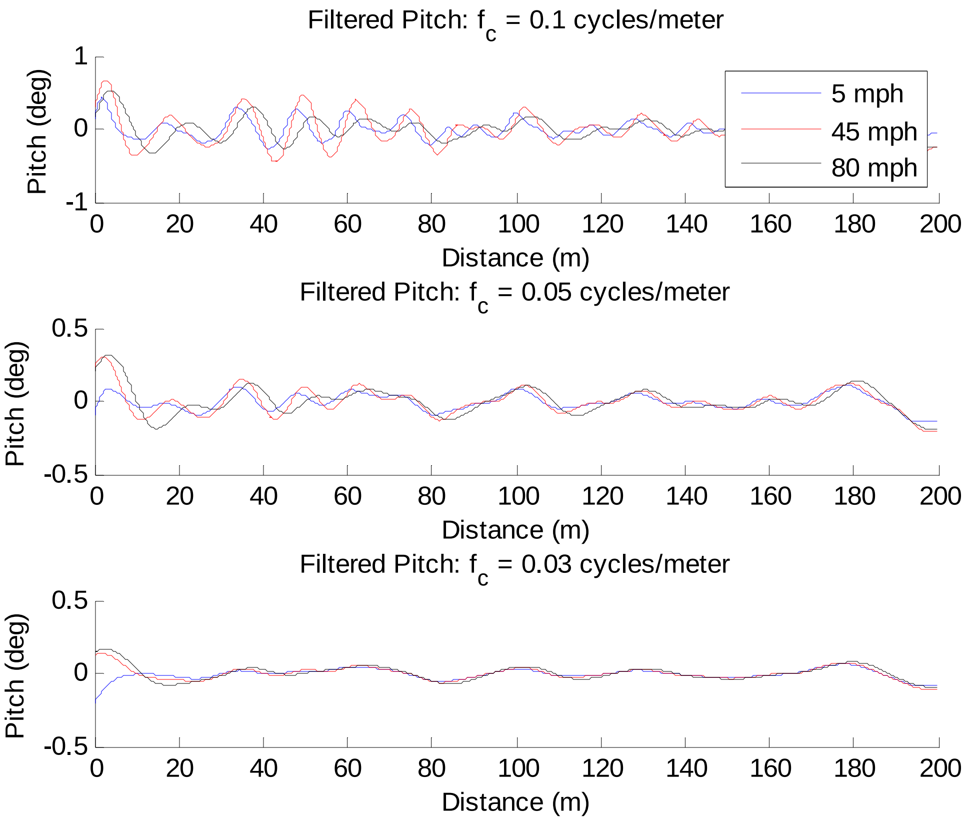

Figure 9.22: Identical Suspension Model – Low Frequency Pitch

The plot above shows that the filtering frequency required to successfully remove the vehicle's suspension dynamics from the pitch measurements also removes a large portion of the information contained within the signal. Also, it can be seen that the filtered signal in Figure 9.22 does not match the known road disturbances shown in Figure 9.15. Therefore it cannot be assumed that this method will correctly estimate the road profile for all vehicles. This also suggests that this method of road grade estimation is ill-suited for an accurate correlation routine.

However, it can be shown that *true* road profile can be extracted from the velocity dependent pitch measurements through the use of model inversion. This inversion results in an accurate, velocity independent measurement without excessive filtering. To show this, the Identical Suspension Model inversion is used. The block diagram is identical to that given for the Kinematic Inversion in Figure 9.17, however, the equation within the inversion block is replaced with that of the given in equation 9.25. Figure 9.23 shows a plot of the pitch angles and road disturbances extracted from the pitch angles at various speeds.

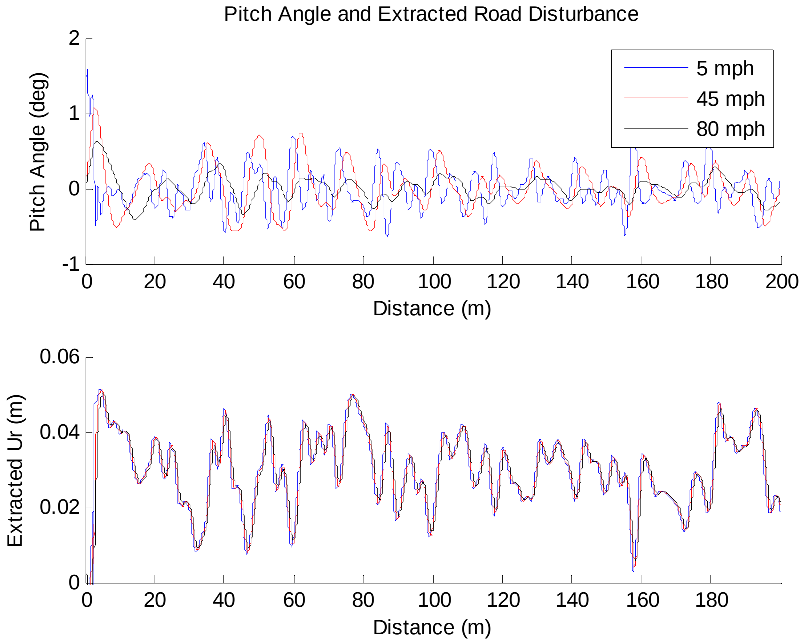

Figure 9.23: Pitch Angle and Extracted Rear Road Disturbance

Figure 9.23 clearly shows that the extracted rear road disturbance remains relatively constant over a wide range of vehicle speeds. In contrast to the low-frequency pitch method presented earlier; this disturbance estimation requires no additional filtering. Therefore this signal will allow for a better correlation than the low frequency content of the pitch measurement. It is also important to note that the extracted road disturbance, U_r, matches the actual sample disturbance input. This is shown in Figure 9.24

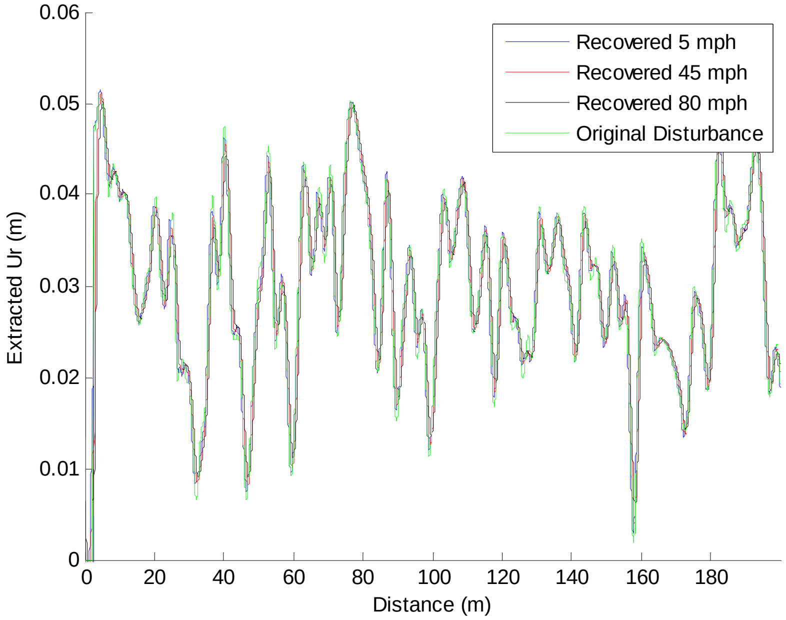

Figure 9.24: Identical Suspension Model – Extracted and Actual Rear Disturbance

From the road disturbance measurements, it is also possible to generate a road grade angle, λ, as defined in Chapter 8. This is done combining the U_r measurements at the current time with those of a future time and taking into account the vehicle length. The diagram in Figure 9.25 clarifies this:

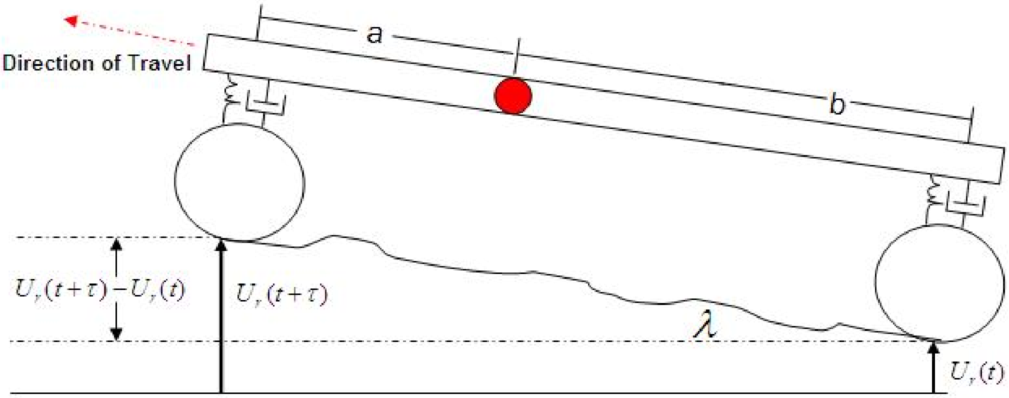

Figure 9.25: Road Grade from Road Disturbance Estimations Diagram

From geometry using the small angle approximation:

$$\sin(\lambda)=\frac{U_r(t+\tau)-U_r(t)}{(a+b)}\cong\lambda \qquad 9.34$$

The resulting Road Grade, λ, from the extracted road disturbance, U_r, is presented in Figure 9.26:

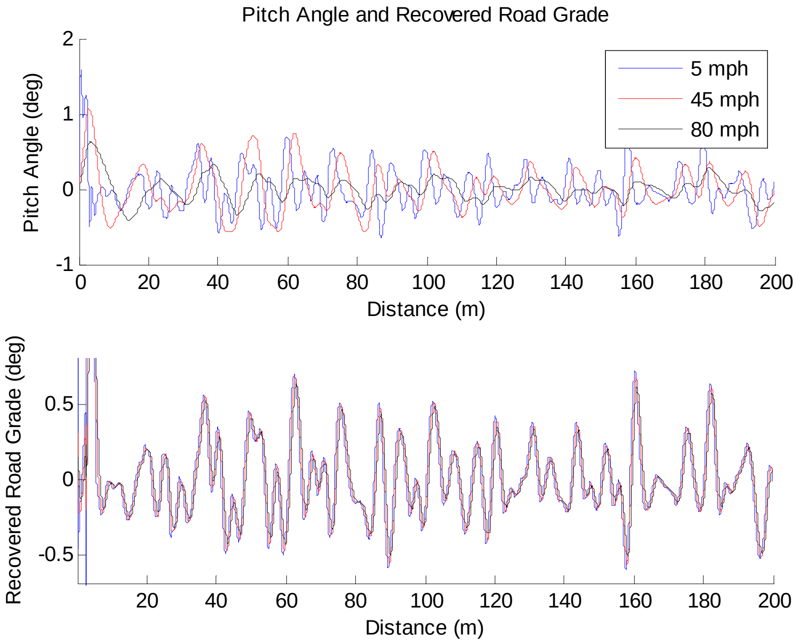

Figure 9.26: Road Grade from Road Disturbance Estimations Plot

Once again, no additional filtering was required for this road grade estimate.

The simulations presented in this section show that, with a proper model inversion, accurate road disturbance and road grade estimations can be made independent of vehicle velocity. The accuracy of the inversion is dependent on several factors such as the accuracy of the time delay estimate and how accurately the pitch-plane model can predict the vehicle's behavior. In the above simulations, these parameters were known exactly so the best possible inversion was achieved.

A brief simulation was performed to investigate the quality of the inversion process when the model does not exactly match that of the vehicle. To do this, the Identical Suspension inversion was performed on pitch measurements that were generated using different suspension parameters in the front and rear. The results are show in Figure 9.27:

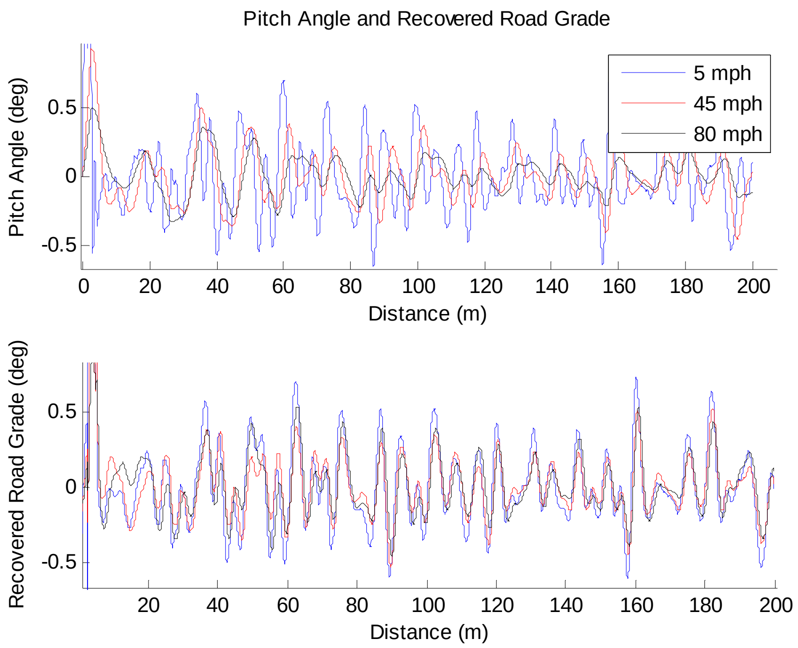

Figure 9.27: Model Inversion – Incorrect Model

The above figure shows that even though the model did not exactly match that of the vehicle, the extracted road grade is still more consistent with varying velocities than the pitch measurements. It should be noted that the parameters used in this simulation were the estimates of test vehicle parameters. As mentioned previously, for this car the estimated spring stiffness and damping values for the front and rear suspensions are very close, however the sprung mass over each suspension is considerably different.

In the next section, this process is repeated with experimental data and estimated suspension parameters.

9.7 Model Inversion on Experimental Data

In this section, the inversions described earlier are applied to in-vehicle pitch measurements. To perform this test, the vehicle was driven over the same straight line path for speeds varying from 5 to 65 mph as discussed in chapter 8. To view measurements over this velocity range, the pitch measurements were aligned using the GPS data recorded during the experiment. The experimental data was then decimated in 30 cm increments. As in chapter 8, the vehicle's suspension dynamics are removed from the pitch measurement by applying a low-pass filter with a cutoff frequency of 0.1 cycles/meter. The resulting raw and filtered pitch measurements are displayed in Figure 9.28

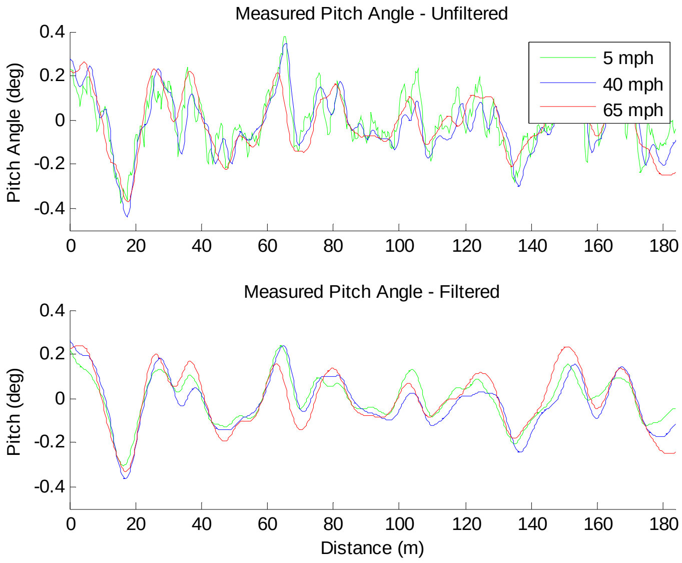

Figure 9.28: Aligned Experimental Pitch Measurements

As discussed previously, the road grade estimation from the low-frequency pitch measurements on this particular vehicle does not change drastically with increasing speed. Therefore the inclusion of a model on this vehicle would not be as beneficial as the one shown in simulation. Regardless, the Identical Suspension Model was used in an inversion process. The resulting road grade estimate from the model inversion and the road grade estimate from the low frequency content of the pitch measurements are displayed in Figure 9.29

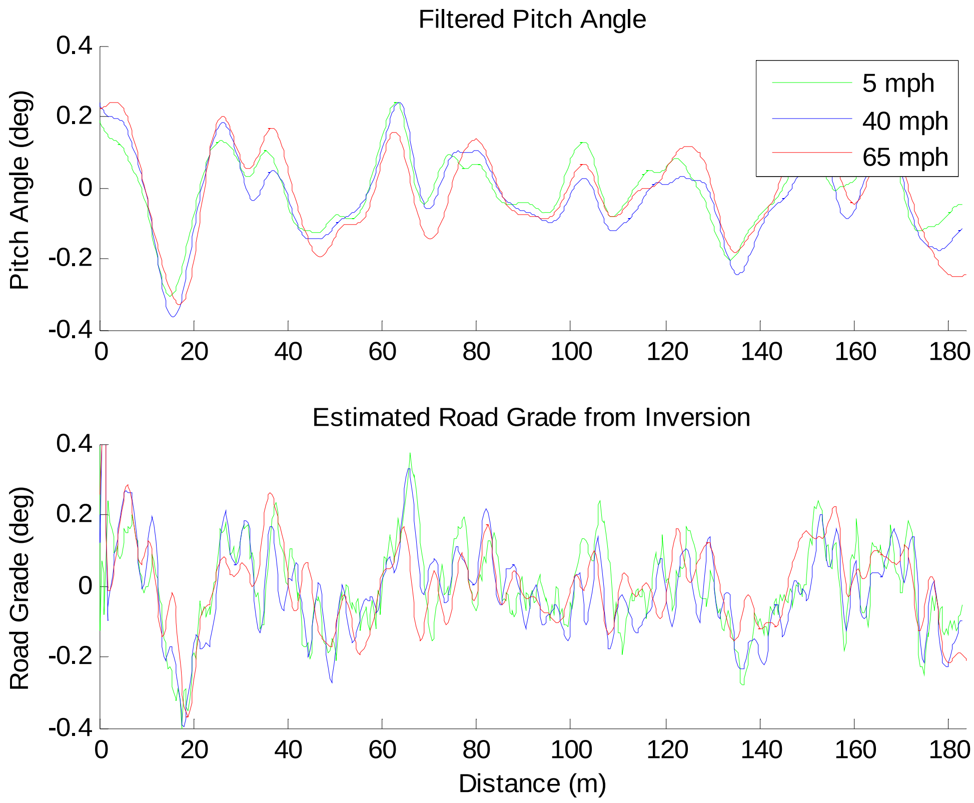

Figure 9.29: Road Grade Estimation Method Comparison – Experimental Data

Since the model inversion accounts for the vehicle dynamics, no additional low-pass filter has been applied to the inverted data. For this particular data set, the correlation for the road grade data is lower than that of the low-frequency pitch measurements. These correlations are:

$$\begin{aligned} Corr\_LowFreqPitch &= 0.7150 \\ Corr\_Inversion &= 0.6349 \end{aligned} \quad 9.35$$

Although the correlation between data sets has not improved, it is interesting to note the recovered trends which were not present in the raw pitch data due to the suspension's filtering. This is shown in Figure 9.30

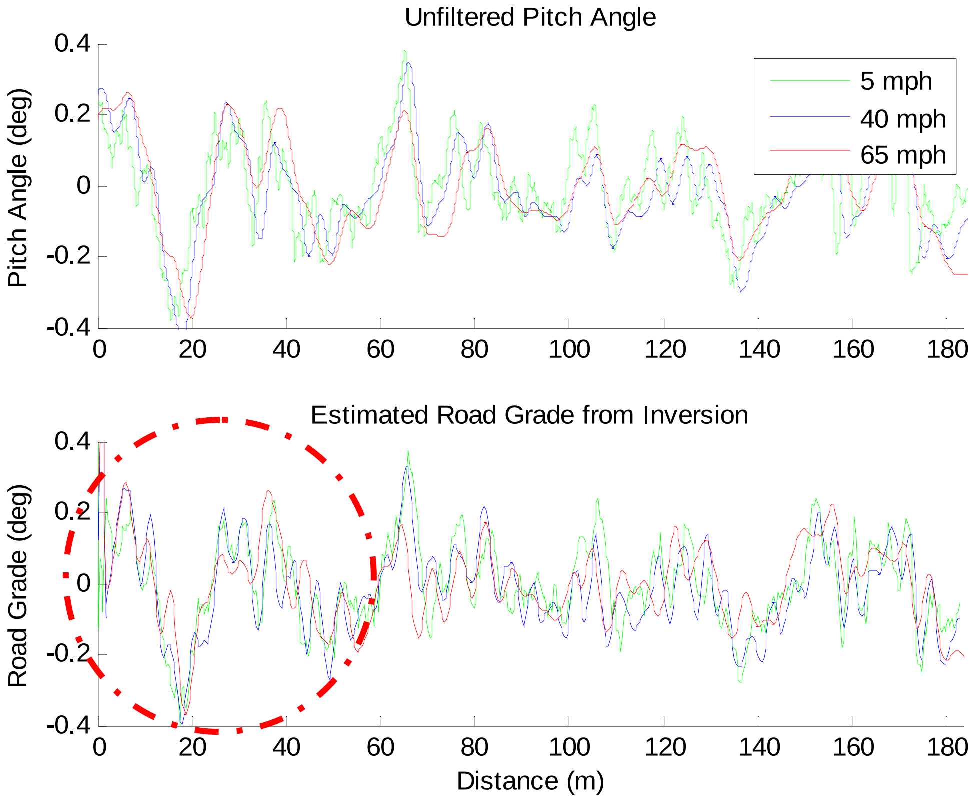

Figure **9.30**: Model Inversion Trend Recovery

In the circled portion of the lower figure, the inversion has recovered some of the road grade peaks which the vehicle suspension filtered out of the high speed pitch data. These peaks can be assumed to be true road grade measurements because they are also present in the 5 mph data. The pitch measurements at low speed can be assumed to be the true representation of the Road Grade since the vehicle's suspension dynamics will not be excited at these speeds. Although the correlation has not improved, this figure re-iterates the inversion technique's ability to estimate true road grade.

The model's inability to generate consistent road grade estimations for the same vehicle at various speeds is likely due to it un-modeled parameters such as rotational inertia. Although more complex models were derived in Appendix A, the inversion of these models fails due to unstable poles in the denominator of the inverted transfer functions.

These inversions can only be used for vehicles with specific suspension configurations and mass distributions.

Even though it has not been shown with experimental data, simulations have shown that with a more accurate model and model parameters, the inversion method can accurately estimate road profile when the low-frequency pitch method cannot. The model inversion method results in velocity and vehicle independent estimations of road grade.

9.8 Conclusions

- Several pitch-plane models were derived and inverted to estimate road grade from vehicle pitch measurements
- A method of estimating vehicle suspension parameters such as spring stiffness and damping has been presented
- Simulation results show that the low frequency portion of the pitch angle measurements will not always be consistent with increasing vehicle speed
- The model inversion process successfully recovers known road disturbances in simulation where the model parameters are exactly known
- The model inversion was not completely successful in experiment. This failure is likely due to model uncertainties and un-modeled parameters.

1. Ozbay, H., *Introduction to Feedback Control Theory*. 1999, Boca Raton, FL: CRC Press, Inc. 232.
2. Cameron, J.T., *Vehicle Dynamic Modeling for the Prediction and Prevention of Vehicle Rollover*. 2005: The Pennsylvania State University.

Chapter 10

Conclusions

The conclusions of this thesis will be separated into three sections: Systems Integration, Planar Model State Identification and Road Grade Positioning. Following a discussion of the conclusions, the future work will be presented.

10.1 System Integration

In this study a military grade DGPS/INS sensing system was integrated into a DSP-based real-time data acquisition system for vehicle state identification. The system is capabable of collecting centimeter level accurate data at 100 Hz. It has a user friendly interface to allow users to capture data directly into MATLAB and to run simulations in teal-time for model matching in the field. The system can also be expanded to allow for actuation control and future automation requirements.

When the system used in this work is compared to that used in previous works, [1], several conclusions can be made. First, the measurements of the current military grade system can be considered much more accurate than that of the previous comercial grade system. Also, the system used in this work give the user the important ability to directly measure vehicle attitude angles. This not only allows the user directly analzye things like vehicle roll, pitch, yaw and sideslip, but also allows the user to accurately account for constant angle offsets due to sensor mounting.

At the end of Cameron's work, the signal-to-noise ratio was brought into question. This is a non-issue with the current system because of both the sensor quality and the built-in 15 state Kalman filter which to smooth the IMU readings – resulting in virtually noise-free measurements.

10.2 Planar Model State Identification

A series of experiments were described which allow a user to accurately estimate vehicle states and hard-to-measure parameters such as cornering stiffness and tire lag. A new method of cornering stiffness estimation was developed which combines the DC gains of experimental data with equations derived from the Bicycle Model. This new method was shown to be more accurate than previous methods for model-matching responses produced by low-frequency steering inputs in both the time and frequency domain.

Another interesting result of this work, is that large variations in cornering stiffness values result in only small variations in the time-domain yaw rate plots. This indicates that time-domain yaw rate plots should not be used to fine-tune cornering stiffness estimations.

High-frequency model matches were obtained by incorporating tire lag into the bicycle model. It was noted that while tire relaxation length for the front and rear tires can be modeled independently, this significantly increases difficulty in parametric matching and only has a minor effect on the model output. This work also showed that the most accurate matches for yaw rate occurred with different tire lag values than the most accurate matches of lateral velocity. Since lateral velocity is more strongly coupled with roll, and roll was left un-modeled in the planar model, the tire lag value which corresponded to the best yaw rate match was assumed to be the most accurate estimation to the true value.

Although the addition of tire lag improved the model matches at high frequencies, it did not improve the fit of steady state circle data. Analysis of the steady state circle data indicated that an additional tire force generation mechanism was present for these maneuvers. A hypothesis was made that the additional force generation was due to camber effects. By assuming camber effects were only present in high roll maneuvers, such as steady state circles, an estimation of these effects was made. An improvement in the steady-state circle lateral velocity model matches was shown by accounting for these effects.

10.3 Road Grade Positioning

Throughout the analysis of the experimental data it became apparent that the terrain was greatly affecting the integrity of the data. An investigation into the nature of these terrain disturbances showed that they were both repeatable and location dependent. These two characteristics allow the terrain disturbances to be used in a localization routine.

Depending on the vehicle, it has been shown that the road grade can be estimated by observing the low-frequency content of the vehicle's pitch measurements. In order for this localization routine to be consistent between vehicles, a pitch plane model must be used to remove the vehicle's suspension dynamics and velocity effects from the pitch measurements. Four pitch plane models of varying complexity were derived in this work. A method of estimating suspension parameters such as spring stiffness and damping was also presented. In simulation it has been shown that with an accurate model in place, the inversion method extracts consistent road grade estimations over a wide range of speeds when the pitch measurements vary greatly.

When the inversion technique was performed on experimental data it was not as successful as in the simulation. Although it recovered portions of the signal which were lost due to suspension filtering, the resulting road grade estimation showed lower correlations than the low frequency pitch measurements. It is believed that the inversion would be more successful when implemented on a vehicle which measures varying pitch measurements with increasing speed as was the case in the simulation.

As mentioned previously, the model inversion is also dependent on how accurately the model represents the actual vehicle. The Identical Suspension Model used in the inversions neglects rotational inertia and treats the vehicle as two separate, but identical quarter car models. Although the vehicle in this study had suspension parameters which were approximately equal, there was a significant difference in the mass distribution above the front and rear suspensions. The uneven mass distribution combined with the rotational inertia make the actual vehicle considerably different from that used in the inversion.

Even though more complex vehicle models were derived in this work, they were not used due to the presence of unstable poles in the denominators of each of the model inversions. These unstable poles will appear with certain combinations of suspension and mass distribution parameters. Additional modeling efforts are needed to find a model which accounts for rotational inertia but does not have unstable poles.

10.4 Future Work

There are several parts of this thesis which require further investigation. These are presented below

10.4.1 System Integration

During system development, many precautions were taken to increase the sytems resistance to the vehicles electrical noise. Although care was taken, the current system is still susceptible noise. On occasion during data collection the Interface DSP needs to be restarted. It is believed that this problem is due to noise which interferes with the transmission on the CAN bus. One possible solution is to optically isolate the tranmission chips on this board. Another easily implemented solution would be to program a simple microprocessor such as the PIC or ATOM to constantly monitor the DSP and to strobe the reset pin when necessary. Either solution would greatly improve the reliability of the system.

The current programming on the both the Master and Interface DSP does not include any error checking. Although certain error messages are transmitted from the reciever to the DSP, these messages are not decoded and therefore are not processed. The Interface DSP should be programmed to accept these messages, and to warn the user if any problems occur. The DSP can be programmed to warn the user of dropped communication with the base station or of insufficient satellite observations. These simple code additions will help make the system fail-safe.

10.4.2 Planar Model State Identification

The planar model presented in this work shows excellent matches in yaw rate with experimental data. There is, however, room for improvement on the lateral velocity matches. As discussed previously, lateral velocity is strongly coulped with roll, so the planar models ability to match lateral velocity may be limited.

One possible way to improve the matching of lateral velocity would be to account for the sprung mass. In the planar model, the lateral velocity is defined for the vehicle chassis – the unsprung mass. In the current vehicle system, the IMU is mounted in the vehicle cabin which is a sprung mass. Therefore the lateral velocity match may improve if this difference is taken into account. To do this a full roll model would be necessary. This is currently be investigated by other students in the research group.

10.4.3 Road Grade Positioning

The next step needed in the investigation of road grade positioning would be to repeat the correlation algorithm on several new vehicles. If each vehicle measures the same low-frequency pitch measurements, then it can be assumed that this method is sufficient to determine road grade. This would be the ideal case and would make this positioning routine relatively simple to implement since no model inversion would be necessary.

However, it is the belief of the author that each vehicle will show considerably different low-frequency pitch measurements. In this case, accurate models of each of the vehicles would be needed. After each of the models were inverted a comparison between the extracted road grade estimates would be needed. The model inversion method would be deemed appropriate if each of the vehicles' extracted road grade estimates show higher correlation than the low-frequency pitch measurements.

After the proper road grade estimation method is determined, a routine for implementing this localization method must be written. This must include a recursive, real-time correlation method which correlates past and current road grade estimations with those of a road grade map. The structure of this algorithm would depend on whether this routine was being used to assist a commercial grade GPS system, or to replace the GPS system. Finally, this routine must be tested and debugged.

In order to achieve additional accuracy in the positioning routine the terrain effects seen in the roll measurements may also be investigated. The position obtained through roll disturbance analysis can then be blended with that of the road grade analysis through a Kalman filter to achieve an optimal solution.

1. Cameron, J.T., *Vehicle Dynamic Modeling for the Prediction and Prevention of Vehicle Rollover*. 2005: The Pennsylvania State University.

Appendix A

Pitch Model Derivation Details

This appendix includes the details of the pitch model derivations not presented in Chapter 9.

A.1 Padé Approximation Discussion

As discussed in Section 9.2, in this work the time delay between the front and rear road inputs has been approximated by a second order Padé approximation. To choose the appropriate order of this approximation, a simple simulation comparing the error associated with different approximation orders was performed. Figure A.1 shows a simulated rear road disturbance and the first four Padé approximations of this disturbance.

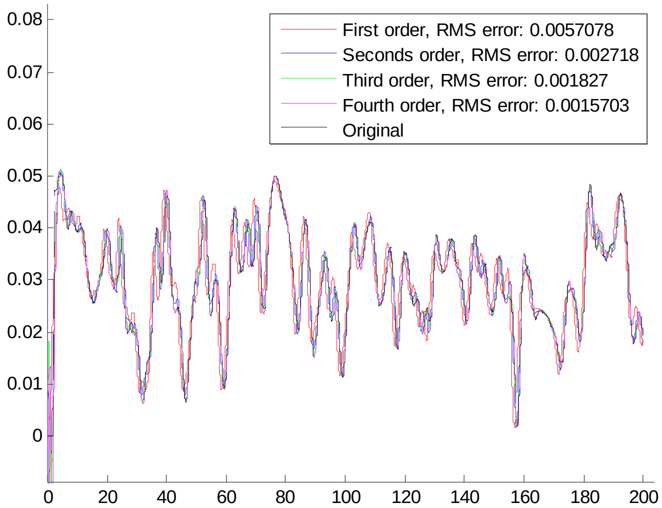

Figure A.1: Padé Approximations – Rear Road Disturbance

Figure A.2 shows only portion of the previous figure so the differences between approximations can be seen more clearly. The legend shows the calculated root-mean-square error between the original disturbance input and each order of the approximation.

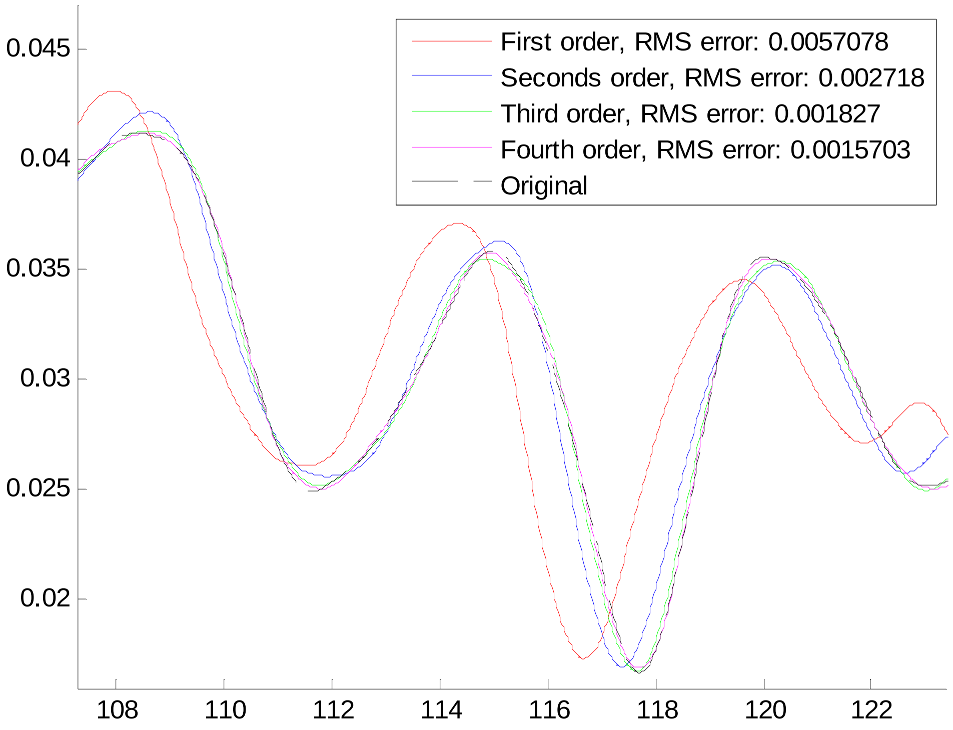

Figure A.2: Padé Approximations – Rear Road Disturbance Zoomed

The above plot clearly shows that the accuracy of the approximation increases with increasing order. Ideally, the highest order approximation would be used to obtain the most accurate results. However, it is obvious from the model derivations in Chapter 9 that a high-order approximation would also lead to significantly more complicated models. Therefore for this work, the second order approximation was used as it was found to be less complex than the third and fourth order approximations while still being considerably more accurate than the simple first order approximation.

A.2 Model 2 – Identical Suspensions, No Rotational Inertia

In order to make equation 9.25 causal poles must be added to the denominator.

Continuing from 9.25 with the coefficients of the numerator replaced with A_n and the coefficients of the denominator replaced with B_n:

$$\frac{U_r(s)}{\theta_y(s)} = (a+b)\cdot\frac{\left(A_4 s^4 + A_3\cdot s^3 + A_2\cdot s^2 + A_1\cdot s + A\right)}{B_2 s^2 + B_{1_r} s} \qquad \textbf{A.1}$$

Two poles must be added to this transfer function in order to make it causal. Both poles will be added at p_1. Therefore the numerator will be scaled by a factor of p_1^2 and the denominator must be multiplied by $(s+p_1)^2$. The resulting transfer function is of the form:

$$\frac{U_r(s)}{\theta_y(s)} = (a+b)\cdot\frac{p_1^2\cdot\left(A_4 s^4 + A_3\cdot s^3 + A_2\cdot s^2 + A_1\cdot s + A\right)}{B_4 s^4 + B_3 s^3 + B_2 s^2 + B_{1_r} s} \qquad \textbf{A.2}$$

Where the A coefficients are:

$$A = n_3 k_r \qquad \textbf{A.3}$$

$$A_1 = n_3 c_r - n_2 k_r \qquad \textbf{A.4}$$

$$A_2 = n_1 k_r - n_2 c_r + n_3 m_{cr} \qquad \textbf{A.5}$$

$$A_3 = n_1 c_r - n_2 m_{cr} \qquad \textbf{A.6}$$

$$A_4 = n_1 m_{cr} \qquad \textbf{A.7}$$

And the B coefficients are:

$$B_1 = 2 \cdot k_r n_2 p_1^2 \qquad \textbf{A.8}$$

$$B_2 = 4 \cdot k_r n_2 \cdot p_1 + 2 \cdot c_r n_2 p_1{}^2 \qquad \textbf{A.9}$$

$$B_{.3} = 2 \cdot k_r n_2 + 4 \cdot c_r n_2 p_1 \qquad \textbf{A.10}$$

$$B_4 = 2 \cdot c_r n_2 \qquad \textbf{A.11}$$

A.3 Model 3 – Different Suspensions, No Rotational Inertia

The next level of difficulty is the model which allows the front and rear suspensions and mass distributions to be different. In this case, the kinematics derived section **9.2** will no longer hold since it treats the rear sprung mass vertical displacement to be a delayed version of the front sprung mass vertical displacement. This derivation starts from equation **9.3**:

$$Z_{sf} - Z_{sr} = \theta_y \cdot (a + b) \qquad \textbf{A.12}$$

The front and rear sprung mass displacements can be written in terms of their respective road input disturbances as in equation **9.24**

$$\frac{Z_{sr}(s)}{U_r(s)} = \frac{c_r s + k_r}{m_{cr} s^2 + c_r s + k_r} = H_r(s)$$
$$\frac{Z_{sf}(s)}{U_f(s)} = \frac{c_f s + k_f}{m_{cf} s^2 + c_f s + k_f} = H_f(s) \qquad \textbf{A.13}$$

Which gives:

$$U_f(s) \cdot H_f(s) - U_r(s) \cdot H_r(s) = \theta_y(s) \cdot (a + b) \qquad \textbf{A.14}$$

Once again utilizing the expressions in equations **9.12** and **9.13**:

$$U_r(s) \cdot \left(P_d^{-1} \cdot H_f - H_r\right) = \theta_y(s) \cdot (a + b) \qquad \textbf{A.15}$$

Substituting equations A.13 and 9.11 into equation equation A.15:

$$(a+b)\cdot\frac{\theta_y(s)}{U_r(s)}=\left(\left(\frac{n_1s^2+n_2s+n_3}{n_1s^2-n_2s+n_3}\right)\cdot\left(\frac{c_fs+k_f}{m_{cf}s^2+c_fs+k_f}\right)-\left(\frac{c_rs+k_r}{m_{cr}s^2+c_rs+k_r}\right)\right)\qquad \textbf{A.16}$$

As with the previous models, the frequency response of this transfer function can be viewed for a direct comparison.

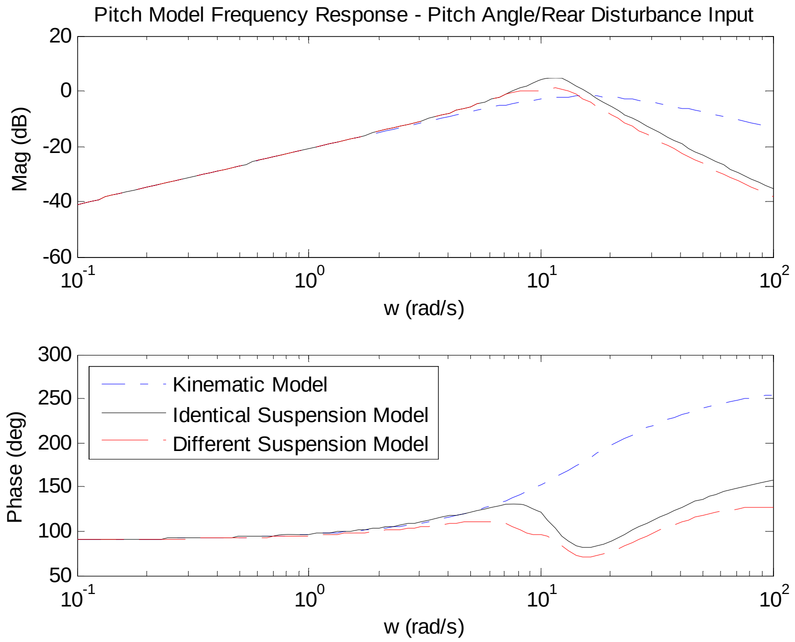

Figure A.3: Different Suspension Model – Frequency Response

As expected, the Different Suspension Model exhibits the same low-frequency behavior as the previous two models. This model only changes slightly in phase and magnitude at high frequencies. This is expected since the front and rear suspension parameters of the vehicle are similar.

As a check, it necessary to confirm that the Different Susepension Model reduces to the Identical Suspension Model when the suspension paramters are the same. This can be easily confirmed by looking at the frequency response:

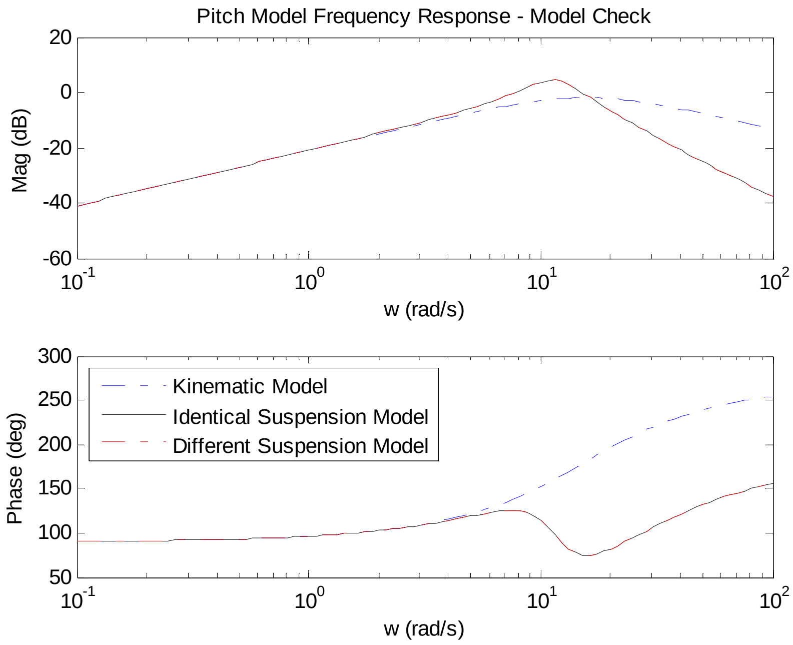

Figure A.4: Different Suspension Model – Model Check

This expression given in A.16 can be expanded and inverted to obtain the transfer function from U_r to θ_y. The result is a lengthy, non-causal transfer function of power s^6 in the numerator and s^5 in the denominator. A single pole must be added for this to be simulated.

Expanding and inverting equation equation A.16 gives the following:

$$\frac{U_r(s)}{\theta_y(s)} = (a+b)\cdot\frac{C_6 s^6 + C_5 s^5 + C_4 s^4 + C_3 s^3 + C_2 s^2 + C_1 s + C}{D_5 s^5 + D_4 s^4 + D_3 s^3 + D_2 s^2 + D_1 s} \qquad \text{A.17}$$

Where the *C* coefficients are:

$$C = (k_f k_r n_3) \tag{A.18}$$

$$C_1 = (-k_f k_r n_2 + c_r k_f n_3 + c_f k_r n_3) \tag{A.19}$$

$$C_2 = (k_f k_r n_1 - c_r k_f n_2 - c_f k_r n_2 + c_f c_r n_3 + k_r m_f n_3 + k_f m_r n_3) \tag{A.20}$$

$$C_3 = (c_r k_f n_1 + c_f k_r n_1 - c_f c_r n_2 - k_r m_f n_2 - k_f m_r n_2 + c_r m_f n_3 + c_f m_r n_3) \tag{A.21}$$

$$C_4 = (c_f c_r n_1 + k_r m_f n_1 + k_f m_r n_1 - c_r m_f n_2 - c_f m_r n_2 + m_f m_r n_3) \tag{A.22}$$

$$C_5 = (c_r m_f n_1 + c_f m_r n_1 - m_f m_r n_2) \tag{A.23}$$

$$C_6 = (m_f m_r n_1) \tag{A.24}$$

And the *D* coefficients are:

$$D_1 = (2 \cdot k_f k_r n_2) \tag{A.25}$$

$$D_2 = (2 \cdot c_r k_f n_2 + 2 \cdot c_f k_r n_2 - k_r m_f n_3 + k_f m_r n_3) \tag{A.26}$$

$$D_3 = (2 \cdot c_f c_r n_2 + k_r m_f n_2 + k_f m_r n_2 - c_r m_f n_3 + c_f m_r n_3) \tag{A.27}$$

$$D_4 = (-k_r m_f n_1 + k_f m_r n_1 + c_r m_f n_2 + c_f m_r n_2) \tag{A.28}$$

$$D_5 = (-c_r m_f n_1 + c_f m_r n_1) \tag{A.29}$$

Equation A.17 is not causal, so as before a pole will be added at p_1:

$$\frac{U_r(s)}{\theta_y(s)} = (a+b) \cdot \frac{p_1 \cdot \left(C_6 s^6 + C_5 s^5 + C_4 s^4 + C_3 s^3 + C_2 s^2 + C_1 s + C\right)}{\left(s + p_1\right) \cdot \left(D_5 s^5 + D_4 s^4 + D_3 s^3 + D_2 s^2 + D_1 s\right)} \tag{A.30}$$

Which results in:

$$\frac{U_r(s)}{\theta_y(s)} = (a+b) \cdot \frac{p_1 \cdot \left(C_6 s^6 + C_5 s^5 + C_4 s^4 + C_3 s^3 + C_2 s^2 + C_1 s + C\right)}{\left(D_6 s^6 + D_5 s^5 + D_4 s^4 + D_3 s^3 + D_2 s^2 + D_1 s\right)} \tag{A.31}$$

Where the *D* coefficients remain the same as before and the *C* coefficients are as follows:

$$D_1 = (2 \cdot k_f k_r n_2 p_1) \qquad \text{A.32}$$

$$D_2 = (2 \cdot k_f k_r n_2 + 2 \cdot c_r k_f n_2 p_1 + 2 \cdot c_f k_r n_2 p_1 - k_r m_f n_3 p_1 + k_f m_r n_3 p_1) \qquad \text{A.33}$$

$$\begin{gathered} D_3 = (2 \cdot c_r k_f n_2 + 2 \cdot c_f k_r n_2 - k_r m_f n_3 + k_f m_r n_3 + \ldots \\ + \; 2 \cdot c_f c_r n_2 p_1 \; + \; k_r m_f n_2 p_1 \; + \; k_f m_r n_2 p_1 - c_r m_f n_3 p_1 \; + \; c_f m_r n_3 p_1) \end{gathered} \qquad \text{A.34}$$

$$\begin{gathered} D_4 = (2 \cdot c_f c_r n_2 + k_r m_f n_2 + k_f m_r n_2 - c_r m_f n_3 + c_f m_r n_3 + \ldots \\ - k_r m_f n_1 p_1 + k_f m_r n_1 p_1 + c_r m_f n_2 p_1 + c_f m_r n_2 p_1) \end{gathered} \qquad \text{A.35}$$

$$D_5 = (-k_r m_f n_1 + k_f m_r n_1 + c_r m_f n_2 + c_f m_r n_2 - c_r m_f n_1 p_1 + c_f m_r n_1 p_1) \qquad \text{A.36}$$

$$D_6 = \left(-c_r m_f n_1 + c_f m_r n_1\right) \qquad \text{A.37}$$

A.4 Model 4 – Full Pitch Plane Model

The most complex model derived in this work will be referred to as the “Full Pitch Plane Model”. This model allows for different suspension dynamics in the front and rear, and also accounts for the roational inertia of the vehicle. No additional assumptions are made beyond the base assumptions presented in Section 9.1. The derivation will use Newtonian mechanics similar to Models 2 and 3.

The front and rear spring and damper forces can be written as in equation 9.21 and the kinematic expressions presented in equation 9.2 can be substituted into each equation:

$$F_{kf} = -k_f (z_{sf} - U_f) = -k_f (z_c + a\theta_y - U_f) \qquad \text{A.38}$$

$$F_{kr} = -k_r (z_{sr} - U_r) = -k_r (z_c - b\theta_y - U_r) \qquad \text{A.39}$$

$$F_{cr} = -c_r (\dot{z}_{sr} - \dot{U}_r) = -c_r (\dot{z}_c - b\dot{\theta}_y - \dot{U}_r) \qquad \text{A.40}$$

$$F_{cf} = -c_f (\dot{z}_{sf} - \dot{U}_f) = -c_f (\dot{z}_c + a\dot{\theta}_y - \dot{U}_f) \qquad \text{A.41}$$

Then by summing moments about the center of gravity:

$$\begin{gathered}(F_{kf}+F_{cf})a-(F_{kr}+F_{cr})b=J_y\ddot{\theta}_y\\ \left((-k_f(z_c+a\theta_y-U_f)-c_f(\dot{z}_c+a\dot{\theta}_y-\dot{U}_f)\right)\cdot a-\\ \left(-k_r(z_c-b\theta_y-U_r)-c_r(\dot{z}_c-b\dot{\theta}_y-\dot{U}_r)\right)\cdot b=J_y\ddot{\theta}_y\end{gathered}\tag{A.42}$$

Where J_y is the rotational inertia in the pitch plane. For the Tracer this paramter is given by NHTSA as

$$J_y=1705\cdot kg\cdot m^2\tag{A.43}$$

The forces in the vertical direction can be summed:

$$\begin{gathered}(F_{kf}+F_{cf})+(F_{kr}+F_{cf})=m_c\ddot{z}_c\\ \left(-k_f(z_c+a\theta_y-U_f)-c_f(\dot{z}_c+a\dot{\theta}_y-\dot{U}_f)\right)+\\ \left(-k_r(z_c-b\theta_y-U_r)-c_r(\dot{z}_c-b\dot{\theta}_y-\dot{U}_r)\right)=m_c\ddot{z}_c\end{gathered}\tag{A.44}$$

Taking the Laplace transforms of equations A.42 and A.44:

$$\begin{gathered}z_c(-k_fa+k_rb)+sz_c(-c_fa+c_rb)+\theta_y(-k_fa^2-k_rb^2)+\\ s\theta_y(-c_fa^2-c_rb^2)+\left(k_faU_f+c_fasU_f-k_rbU_r-c_rbsU_r\right)=J_ys^2\theta_y\end{gathered}\tag{A.45}$$

$$\begin{gathered}z_c(-k_f-k_r)+sz_c(-c_f-c_r)+\theta_y(-k_fa+k_rb)+\\ s\theta_y(-c_fa+c_rb)+\left(k_fU_f+c_fsU_f+k_rU_r+c_rsU_r\right)=m_cs^2z_c\end{gathered}\tag{A.46}$$

Equation. A.46 can be rearranged to solve for the vertical displacement at the center of gravity Z_c:

$$z_c=\frac{e^{st}k_fU_r+k_rU_r+c_rU_rs+c_fU_re^{st}-ak_f\theta+bk_r\theta-ac_fs\theta+bc_rs\theta}{k_f+k_r+c_fs+c_rs+m_cs^2}\tag{A.47}$$

Equation A.47 is then substituted into equation A.46. This can then be rearranged to solve for the ratio θ_y/U_r:

$$\frac{\theta_y}{U_r} = \frac{Xe^{st}\left(\left(a+b\right)Y + am_c s^2\right) - Y\left(\left(a+b\right)X + bm_c s^2\right)}{2abXY + b^2Y\left(X + s^2 m_c\right) + aX\left(Y + s^2 m_c\right) + J_y s^2\left(X + Y + m_c s^2\right)} \qquad \text{A.48}$$

with

$$X = k_f + c_f s$$

$$Y = k_r + c_r s$$

The frequency response of the system is shown in Figure A.5

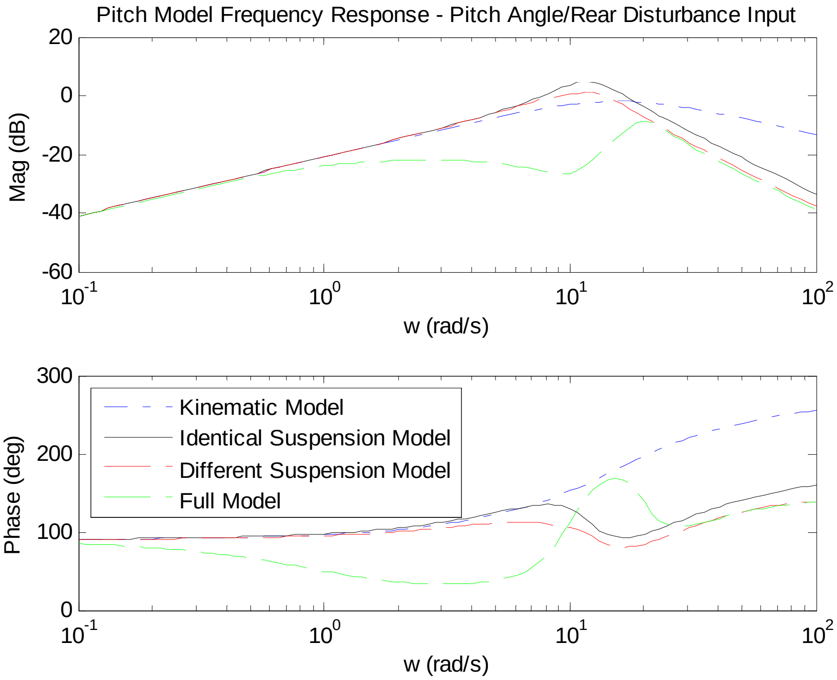

Figure A.5: Full Model – Frequency Response

This can then be inverted to solve for that ratio U_r/θ_y:

$$\frac{U_r}{\theta_y} = \frac{2abXY + b^2Y\left(X + s^2 m_c\right) + aX\left(Y + s^2 m_c\right) + J_y s^2\left(X + Y + m_c s^2\right)}{Xe^{st}\left(\left(a+b\right)Y + am_c s^2\right) - Y\left(\left(a+b\right)X + bm_c s^2\right)} \qquad \text{A.49}$$

As in the previous derivations, the Padé approximation is used to estimate the time delay with a rational function.

The inverse Padé approximation can be substituted into the above equation for e^{st}. This algebra was performed in Wolfram's Mathematica and the resulting equation is of the form:

$$\frac{U_r(s)}{\theta_y(s)} = \frac{E_6 s^6 + E_5 s^5 + E_4 s^4 + E_3 s^3 + E_2 s^2 + E_1 s + E}{F_5 s^5 + F_4 s^4 + F_3 s^3 + F_2 s^2 + F_1 s} \tag{A.50}$$

Where the *E* coefficients are:

$$E = k_f k_r n_3 \cdot (a+b)^2 \tag{A.51}$$

$$E_1 = \text{-}k_f k_r n_2 \cdot (a+b)^2 \ + c_r k_f n_3 \cdot (a+b)^2 + c_f k_r n_3 \cdot (a+b)^2 \tag{A.52}$$

$$\begin{aligned} E_2 = {} & k_f k_r n_1 \cdot (a+b)^2 \text{ - } c_r k_f n_2 \cdot (a+b)^2 \text{ -} c_f k_r n_2 \cdot (a+b)^2 + c_f c_r n_3 \cdot (a+b)^2 \\ & + J_y k_f n_3 \ + \ J_y k_r n_3 \ + \ a^2 k_f m_c n_3 \ + \ b^2 k_r m_c n_3 \end{aligned} \tag{A.53}$$

$$\begin{aligned} E_3 = {} & c_r k_f n_1 (a+b)^2 + c_f k_r n_1 (a+b)^2 \text{ -} c_f c_r n_2 (a+b)^2 \text{ - } J_y k_f n_2 \\ & \text{-} J_y k_r n_2 \ \text{ - } \ a^2 k_f m_c n_2 \ \text{ - } \ b^2 k_r m_c n_2 \ + \ c_f J_y n_3 \ + \ c_r J_y n_3 \ + \\ & a^2 c_f m_c n_3 \ + \ b^2 c_r m_c n_3 \end{aligned} \tag{A.54}$$

$$\begin{aligned} E_4 = {} & p1 \cdot (c_f c_r n_1 \cdot (a+b)^2 + \ J_y k_f n_1 + J_y k_r n_1 + \ a^2 k_f m_c n_1 \\ & + \ b^2 k_r m_c n_1 \text{ - } \ c_f J_y n_2 \text{ - } \ c_r J_y n_2 \text{ - } \ a^2 c_f m_c n_2 \text{ - } \ b^2 c_r m_c n_2 \\ & + \ J_y m_c n_3) \end{aligned} \tag{A.55}$$

$$E_5 = c_f J_y n_1 + c_r J_y n_1 + a^2 c_f m_c n_1 + b^2 c_r m_c n_1 \text{ -} J_y m_c n_2 \tag{A.56}$$

$$E_6 = J_y m_c n_1 \tag{A.57}$$

And the *F* coefficients are:

$$F_1 = \ 2ak_f k_r n_2 + 2bk_f k_r n_2 \tag{A.58}$$

$$F_2 = \ 2ac_r k_f n_2 + 2bc_r k_f n_2 + 2ac_f k_r n_2 + 2bc_f k_r n_2 + ak_f m_c n_3 \text{ - } \ bk_r m_c n_3 \tag{A.59}$$

$$F_3 = \ 2ac_f c_r n_2 + 2bc_f c_r n_2 + ak_f m_c n_2 + bk_r m_c n_2 + ac_f m_c n_3 \text{ -} bc_r m_c n_3 \tag{A.60}$$

$$F_4 = \ ak_f m_c n_1 \text{ -} bk_r m_c n_1 + ac_f m_c n_2 + bc_r m_c n_2 \tag{A.61}$$

$$F_5 = \ ac_f m_c n_1 \text{ -} bc_r m_c n_1 \tag{A.62}$$

When a pole is added to A.50 at p_1 each *E* coefficient is scaled by p_1 and the denominator is multiplied by $(s+p_1)$. The resulting equation is of the form:

$$\frac{U_r(s)}{\theta_y(s)} = \frac{p_1 \cdot \left(E_6 s^6 + E_5 s^5 + E_4 s^4 + E_3 s^3 + E_2 s^2 + E_1 s + E\right)}{F_6 s^6 + F_5 s^5 + F_4 s^4 + F_3 s^3 + F_2 s^2 + F_1 s} \tag{A.63}$$

Where the *E* coefficients are the same as before and the *F* coefficients are:

$$F_1 = 2ak_f k_r n_2 p_1 + 2bk_f k_r n_2 p_1 \tag{A.64}$$

$$\begin{aligned} F_2 = {} & 2ak_f k_r n_2 + 2bk_f k_r n_2 + 2ac_r k_f n_2 p_1 + 2bc_r k_f n_2 p_1 + \\ & 2ac_f k_r n_2 p_1 + 2bc_f k_r n_2 p_1 + ak_f m_c n_3 p_1 - bk_r m_c n_3 p_1 \end{aligned} \tag{A.65}$$

$$\begin{aligned} F_3 = {} & 2ac_r k_f n_2 + 2bc_r k_f n_2 + 2ac_f k_r n_2 + 2bc_f k_r n_2 + ak_f m_c n_3 \ - \\ & bk_r m_c n_3 + 2ac_f c_r n_2 p_1 + 2bc_f c_r n_2 p_1 + ak_f m_c n_2 p_1 + bk_r m_c n_2 p_1 \\ & + ac_f m_c n_3 p_1 - bc_r m_c n_3 p_1 \end{aligned} \tag{A.66}$$

$$\begin{aligned} F_4 = {} & 2ac_f c_r n_2 + 2bc_f c_r n_2 + ak_f m_c n_2 + bk_r m_c n_2 + ac_f m_c n_3 - \\ & bc_r m_c n_3 + ak_f m_c n_1 p_1 - bk_r m_c n_1 p_1 + ac_f m_c n_2 p_1 + bc_r m_c n_2 p_1 \end{aligned} \tag{A.67}$$

$$F_5 = ak_f m_c n_1 - bk_r m_c n_1 + ac_f m_c n_2 + bc_r m_c n_2 + ac_f m_c n_1 p_1 - bc_r m_c n_1 p_1 \tag{A.68}$$

$$F_6 = ac_f m_c n_1 - bc_r m_c n_1 \tag{A.69}$$

Appendix B

Detailed Interface DSP Operation

This appendix gives a detailed example of the Interface DSP operation which was introduced in Section 4.1.4.1.1. This will show how a standard NovAtel data log is decoded, processed and sent to the Mater DSP. This is meant to be used by anyone who follows this work and needs to change the systems current data logging configuration. This should be read simultaneously with the commented code in order to gain a complete understanding of how it works. Once again, this section is only an outline of the overall DSP code.

B.1 Data Retrieval from DL-4plus

The Interface DSP communicates with the DL-4plus receiver over standard RS-232 serial protocol. To do this the DSP utilized the serial port on the Digi-I/O board designed by Dan Block at the Control Systems Instructional Laboratory at the University of Illinois at Urbana-Champaign. The DSP is programmed with a high priority Task function to continuously monitor the serial port for incoming data.

```
void UART1ReceiveCharTask(void) {
   while(1)  //Wait forever for new character
   {   …
```

The UART1ReceiveCharTask task first looks for three new characters on the serial port. If three characters can be read in a row, it stores these characters into variables called sync1, sync2 and sync3 and sets a flag to indicate that three characters have been read.

```
if(syncflag == 0)
{
checkfornewcharUART1(&sync1,SYS_FOREVER);
checkfornewcharUART1(&sync2,SYS_FOREVER);
checkfornewcharUART1(&sync3,SYS_FOREVER);
syncflag = 1;
}
```

NovAtel specifies that each log type has its own three specific sync characters. In this example, the log to be decoded is INSSPDSB which is a short binary INS log. NovAtel provides the following information about this logs header structure [1, 2]:

Table **B.1**: Short Binary INS Message Header Structure

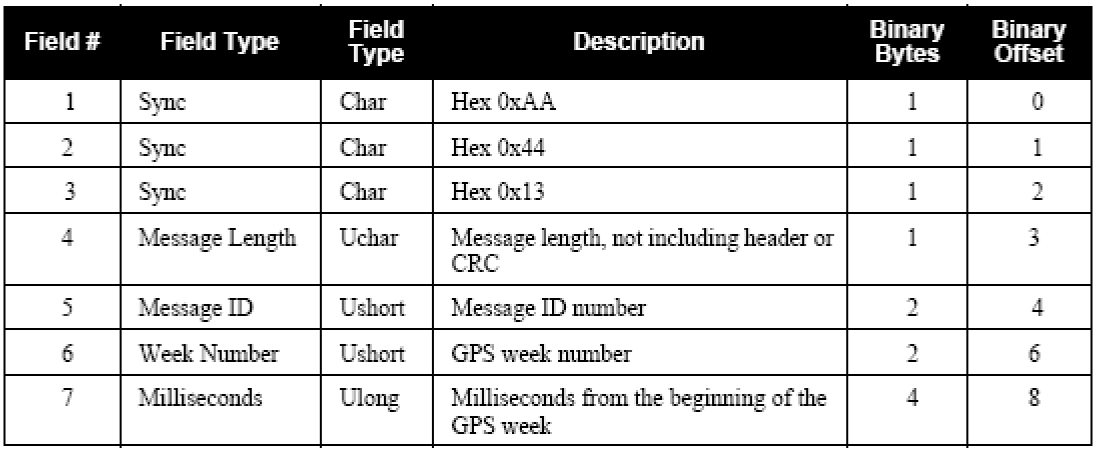

Field #	Field Type	Field Type	Description	Binary Bytes	Binary Offset
1	Sync	Char	Hex 0xAA	1	0
2	Sync	Char	Hex 0x44	1	1
3	Sync	Char	Hex 0x13	1	2
4	Message Length	Uchar	Message length, not including header or CRC	1	3
5	Message ID	Ushort	Message ID number	2	4
6	Week Number	Ushort	GPS week number	2	6
7	Milliseconds	Ulong	Milliseconds from the beginning of the GPS week	4	8

After the three bytes have been read from the serial port, they are compared to the sync bytes 0xAA, 0x44 and 0x13 (integer values 170, 68 and 19 respectively). If these sync characters do not match, they are shifted and a new byte is read:

```
else //sync bytes do not match
{
//Store last 2 sync bytes, and read in a new 3rd one to check again.
sync1 = sync2;
sync2 = sync3;
checkfornewcharUART1(&sync3,SYS_FOREVER);
}
```

If the specified bytes do match, then the program proceeds to read the remainder of the message. First an array is filled with the rest of the short header – 9 bytes:

```
while(UART1headercollect < 9) //Fill header with 9 bytes - short header logs
{
checkfornewcharUART1(&UART1receivechar,SYS_FOREVER);
UART1HeaderArray[UART1headercollect].IntValue = (char)UART1receivechar &
0xFF;
UART1headercollect++;
}
```

After the header array has been filled, the message ID can be extracted:

```
MessageIDByte1 = UART1HeaderArray[1].IntValue;
MessageIDByte2 = UART1HeaderArray[2].IntValue;
MessageIDByte2 = MessageIDByte2 << 8;  //Shifts bits over 8
MessageID = MessageIDByte2 | MessageIDByte1;
```

The last two lines of the above code combines the two bytes corresponding to the message ID by bit-shifting the second byte and then performing a bitwise "OR" between the two values.

The header also gives the message length which is specific to each log and has stored in the first element of the UART1HeaderArray array:

```
MessageLength = UART1HeaderArray[0].IntValue;
```

With the message length and ID known, the log content can be read. This is done in the function UART1MessageCollection in the same manner as reading the message header:

```
void UART1MessageCollection(void)
{
UART1messagecollect = 0;
  while ((UART1messagecollect < MessageLength))
  {
  checkfornewcharUART1(&UART1receivechar,SYS_FOREVER);
  UART1MessageArray[UART1messagecollect].IntValue = (char)UART1receivechar &
0xFF;
  UART1messagecollect++;
  }
} //end of function UART1MessageCollection
```

After the message collection is complete, the task UART1ReceiveCharTask posts a semaphore SEM_UART1MessageReady to initiate a second task NetReceiveMessageTask which is used parses the messages and send them over the CAN bus.

B.2 DL-4plus Log Parsing

For each available log, NovAtel supplies a table indicating the breakdown of all of its contents [1, 2]. Since binary messages have been used for speed purposes, the data parsing is not as straight forward as one may assume. In order to accomplish the processing in binary format, Structs and Unions were used extensively throughout the code to allow access to a variable in memory through both its double/integer value, or one byte at a time. This parsing process is described in this section for the INSSPDSB log.

After the entire message is received and stored in the UART1MessageArray array, the NetReceiveMessageTask is activated. This task identifies the message from its message ID – which was extracted from the header, and sends the message contents to the appropriate sub-function for parsing. In the case of the INSSPDSB log, the message ID and contents are given by NovAtel as [1, 2]:

Table B.2: INSSPDSB Message Structure

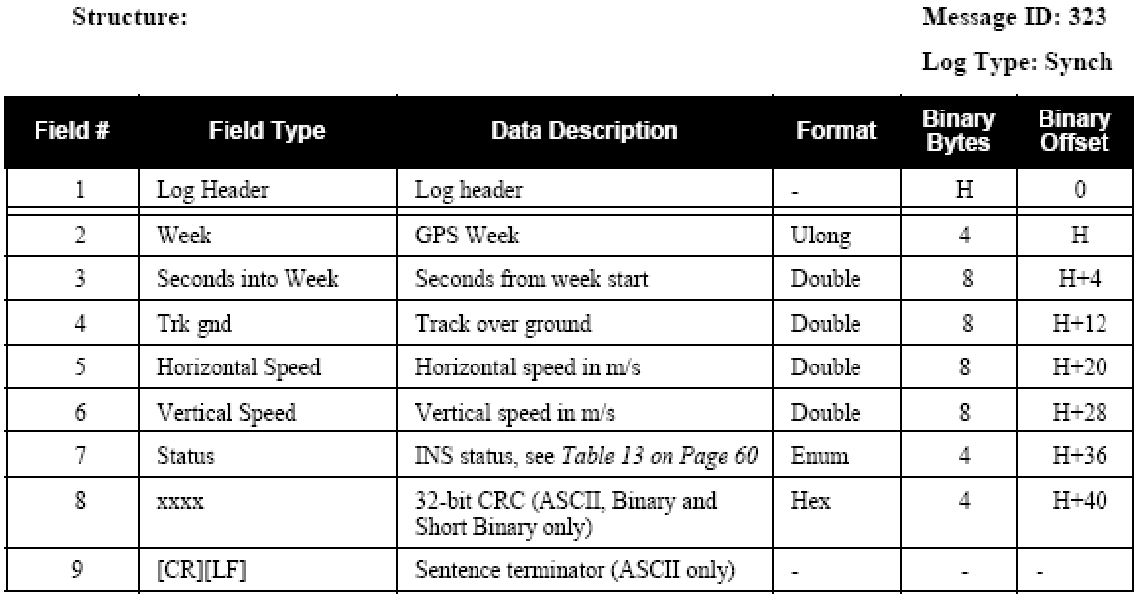

Structure:

Message ID: 323
Log Type: Synch

Field #	Field Type	Data Description	Format	Binary Bytes	Binary Offset
1	Log Header	Log header	-	H	0
2	Week	GPS Week	Ulong	4	H
3	Seconds into Week	Seconds from week start	Double	8	H+4
4	Trk gnd	Track over ground	Double	8	H+12
5	Horizontal Speed	Horizontal speed in m/s	Double	8	H+20
6	Vertical Speed	Vertical speed in m/s	Double	8	H+28
7	Status	INS status, see *Table 13 on Page 60*	Enum	4	H+36
8	xxxx	32-bit CRC (ASCII, Binary and Short Binary only)	Hex	4	H+40
9	[CR][LF]	Sentence terminator (ASCII only)	-	-	-

From this log, the current system utilizes the Trk gnd (velocity direction), Horizontal Speed and Vertical speed and disregards the remaining information. It is important that only the needed values are extracted from the messages so that the traffic over the CAN bus can be kept to a minimum.

As indicated in table B.2 the three values to be used are of type double and are 8 bytes long. Since the message was read into an array one byte at a time, it is necessary to reconstruct these double values from their one byte sections. This is most easily done by declaring these variables as Structs and making them part of a Union as demonstrated below:

```
struct DoubleBits{
    unsigned sb0: 8;
    unsigned sb1: 8;
    unsigned sb2: 8;
    unsigned sb3: 8;
    unsigned sb4: 8;
    unsigned sb5: 8;
    unsigned sb6: 8;
    unsigned sb7: 8;
};

union DoubleBitsType{
    double DoubleValue;
    struct DoubleBits bits;
};
volatile union DoubleBitsType horSpd, trkGnd, vertSpd;
```

The above code allows easy access to each of the 8 bytes of the double variables horSpd, trkGnd and vertSpd. In the case of trkGnd, the 8 bytes have been read and stored in elements 13 through 20 of the UART1MessageArray array. These bytes are recombined into the double value in the parseINSSPDS functions as follows:

```
trkGnd.bits.sb0 = UART1MessageArray[12].bits.sb0;
trkGnd.bits.sb1 = UART1MessageArray[13].bits.sb0;
trkGnd.bits.sb2 = UART1MessageArray[14].bits.sb0;
trkGnd.bits.sb3 = UART1MessageArray[15].bits.sb0;
trkGnd.bits.sb4 = UART1MessageArray[16].bits.sb0;
trkGnd.bits.sb5 = UART1MessageArray[17].bits.sb0;
trkGnd.bits.sb6 = UART1MessageArray[18].bits.sb0;
trkGnd.bits.sb7 = UART1MessageArray[19].bits.sb0;
```

Where UART1MessageArray's first element has an index of 0. Each byte of the trkGnd variable can be access as shown above or the full double value can be accessed calling trkGnd.DoubleValue.

This process is performed for each of the variables that need to be transmitted. After they have been processed the SendToCan function is called which sends them over the CAN bus to the Master DSP. At the systems current state, Float values are transmitted over CAN. Because of this, each variable of type double (except latitude and longitude) is truncated into type float since the extra precision is not necessary. The SendToCan function formats each of the values to agree with the current CAN protocol and transmits them to the Master DSP. This was done in previous work by Vishisht Gupta and will not be explained here.

B.3 Data Read from Steering Sensors

As discussed in chapter 4, the interface DSP is also responsible for processing the outputs of the steering sensors. The sensors which are installed are linear string potentiometers. In order to read these analog devices, an Analog-to-Digital Conversion (ADC) needs to take place. This is performed by the AD7864 chip on the custom CAN boards designed by Vishisht Gupta of The Pennsylvania State University. The code needed to perform this task is briefly described in this section.

The Interface DSP has been programmed with a period function, ADCStart which runs once at 50Hz. This function only has one line:

```
void ADCStart()
{
    ADC7864_Start();
}
```

The ADC7864_Start function has been written in the include file ad7864.c. This function is used to pulse a signal to the CONVST pin on the ADC chip. The CONVST pin initiates the analog to digital conversion on all four tracks of the ADC chip. This ADC7864_Start function also consists of only one line of code:

```
*(volatile int *)(0xA03C0080) = 0;
```

This line of code is a write command that pulls the CONVST pin low through several pin transitions. The ADC portion of the CAN board will not be described here as it is beyond the scope of this work. However, it is important to note that when the ADC chip has finished converting all of its tracks, the ADC sets its BUSY pin to low. The BUSY pin is directly connected to the external interrupt pin (EXT_INT7) on the DSP so that its value also becomes 0. When the eternal interrupt is triggered, the DSP goes into the Interrupt

Service Routine that is set for this interrupt pin. For this work, the hardware interrupt triggers the function ADC_Interrupt_Func which has been copied below:

```
void ADC_Interrupt_Func()
{
    ADC1_CAN_Read(&adc1, &adc2, &adc3, &adc4);
    analog1.data = adc1;
    analog2.data = adc2;
    analog3.data = adc3;
    analog4.data = adc4;
}
```

This function reads the data from the ADC chip through the function ADC1_CAN_Read which is also written in the include file ad7864.c. Each of the ADC channel values are saved in the variables adc1 – adc4. The details of this data read will not be discussed here.

After the analog data has been read, it is sent over the CAN bus to the Master DSP by using the SendToCan function just as the DL-4plus data logs were sent.

1. NovAtel, *OEM4 Family of Receivers User Manual - Vol. 2 Command and Log Reference, OM-20000047, Rev 18*. 2005: Alberta, Canada.
2. Novatel, *SPAN Technology User Manual, OM-20000062, Rev. 7*. 2005: Alberta, Canada.

Appendix C

GPS/INS Setup and Troubleshooting Guide

This appendix will present a detailed outline for implementing the DGPS/INS and data acquisition systems on a vehicle. This is meant to be used by researchers who will follow up this work. There are several minor problems with the system which will also be addressed and their temporary solution is given.

For completeness, this guide will assume no prior knowledge of the system that has not been presented elsewhere in this thesis and therefore includes more steps than necessary. It will be presented in two sections – the first demonstrates what to do with the current state of the system and the second addresses some possible problems.

C.1 Current Setup Procedure

The subsequent three sections describe the setup of the Base station, Rover station and the Data Acquisition system. It is possible to set up these systems simultaneously if the user chooses to do so. The order presented here represents the easiest, most logical way to start the system.

C.1.1 Base Station Setup

All of the base station components have been packaged into a locked carrying case for convenience. The Receiver's software settings have been saved into memory so no programming should be necessary at this state. The modems are also properly programmed at this time so the base station is easy to setup. Since the position has been saved, it must be placed in the same spot for each use. The base station is to be placed on the loading dock next to the skidpad as described below:

1. Locate and unlock the base station carrying case – The combination has been left with Dr. Brennan.
2. Align the base station with the mounting brackets located on the loading dock as pictured in Figure **C.1**

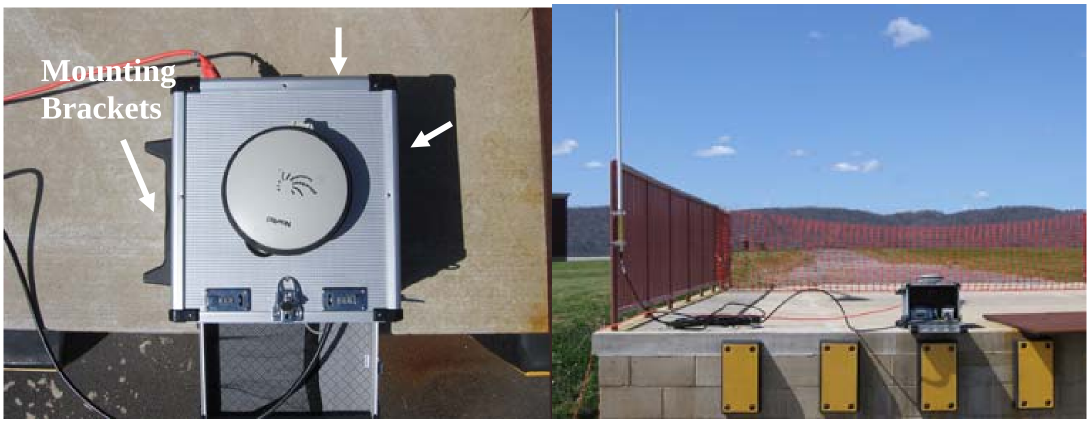

Figure **C.1**: Base Station Mounting

3. Mount the radio antenna vertically using the supplied mounting brackets as pictured in Figure **C.2** and connect it to the base station modem via the long cable labeled GPS-C006 0002.

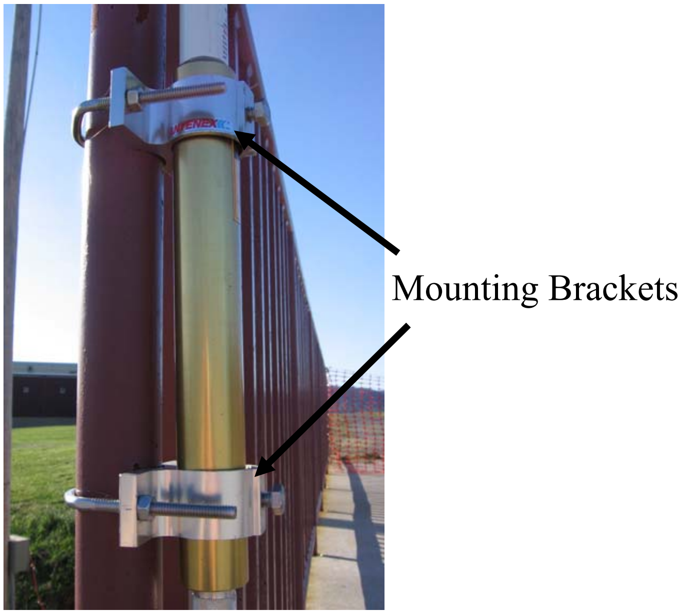

Figure C.2: Radio Antenna Mounting

4. Run an extension cord from the base station to the outlet located to the left of the loading dock
5. Power the DL-4plus receiver and wait approximately 5 minutes
   After 5 minutes or less the receiver should display "FIX" on the bottom of the LCD as shown in Figure C.3. If after 5 minutes FIX is not displayed, please see section C.2

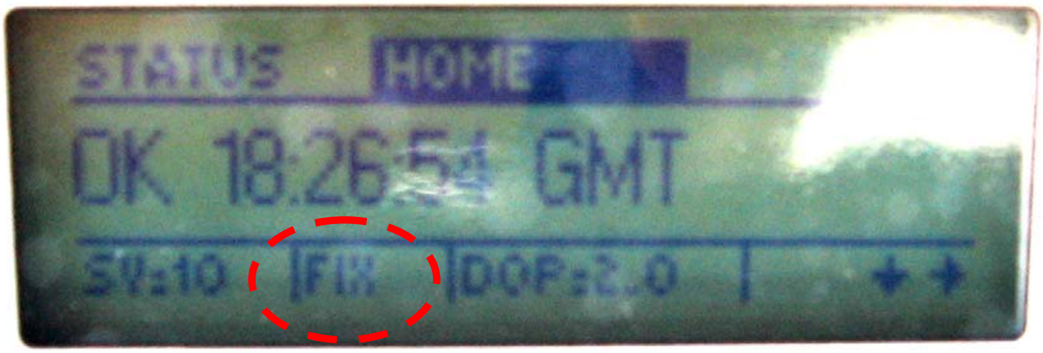

Figure C.3: Receiver with Fixed Position

6. After the receiver indicates its position is fixed, it can calculate and send differential corrections to the rover station. This transmission can be

verified by observing a flashing ***green light*** above the COM2 port on the rear of the receiver. This will occur only after the position is fixed. If the LCD indicates FIX, and this light is not flashing, see section Base station setup complete.

C.49.2 Rover Station Setup

The Rover Station setup consists of setting up both the Rover GPS/INS system and the Data Acquisition system. These will be described below.

C.49.2.1 GPS/INS System

1) Mount the IMU to the custom mounting bracket located at the center of gravity using the supplied hardware. A socket wrench and allen key will be needed – these tools have been left in the ashtray. When mounting the IMU, be sure to mount it in the proper orientation – with the Receiver-IMU connection facing the rear of the car. It is important that the receiver is seated properly in the mounting bracket. The proper mounting location is pictured in Figure **C.4**

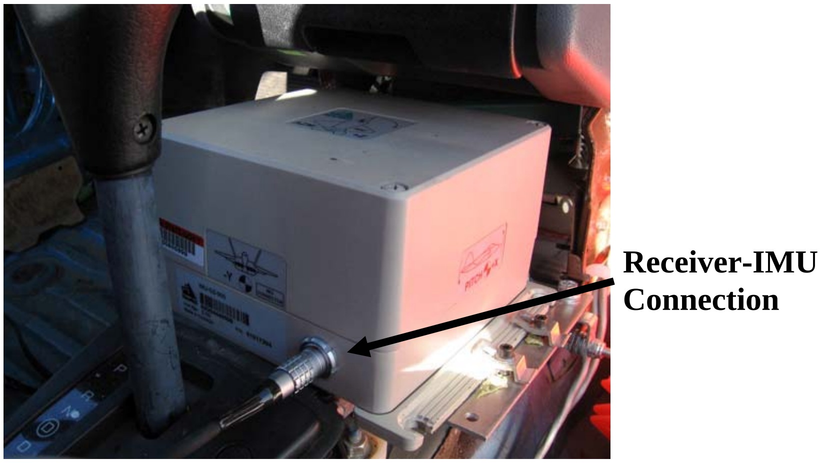

Figure C.4: IMU Mounting

2) Plug the IMU into the AUX port of the Rover DL-4plus via the cable labeled 01017384.
3) Mount the GPS antenna to the roof of the car. On the Tracer a roof rack is used which is permanently fixed above the IMU center as pictured below. Figure **C.5**

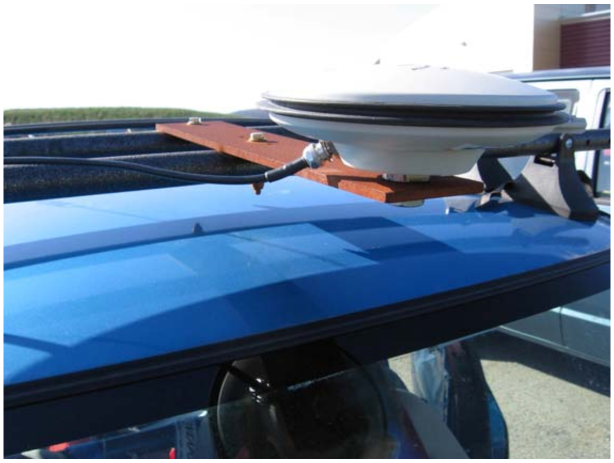

Figure C.5: GPS Antenna Mounting

Because of this, recalibration of the leverarm is not necessary. However if you are using the ChaseCam mounts, re-calibration of the lever arm is necessary as outlined in Chapter 4 of this thesis and in the SPAN Manual.

4) Plug the GPS antenna into the ANTENNA connection of the DL-4plus via cable GPS-C006 0002
5) Mount the small Radio antenna to the vehicle. The mounting of the Radio antenna need not be exact. Just be sure that it is in the upright position on the top of the vehicle (not obstructed by anything). On the Tracer a custom bracket is used, but in the future a ChaseCam mount can be used.
6) Connect the Radio antenna to the FreeWave modem via the antenna cable
7) Connect the FreeWave modem to the COM2 port of the DL-4plus via the brown RS-232 cable labeled "ST."
8) Turn the vehicle on.
9) With ***nothing*** plugged into the AC outlet of the DC Inverter, plug the inverter into the cigarette lighter. It is important that there is nothing plugged into the Inverter on startup because of voltage spikes which occur. *This has damaged the PC power supplies in the past.*
10) After the inverter has started up, plug the APC UPS Surge Protector into the inverters AC outlet. When the surge protector is powered on, the Client PC should start up.
11) Power on the Rover DL-4plus receiver. NOTE: On startup, the receiver will perform the IMU alignment routine outlined in Chapter 4 and the SPAN Manual. During this time, the vehicle should ***remain stationary***. If the vehicle is put in motion, the calibration will stop – thus resulting in an in-motion calibration routine. This should be avoided whenever possible.

When the calibration routine is finished, ***only the green light*** above the COM1 port should begin flashing. This indicates that the receiver has acquired four or more satellites, calibrated the IMU and started to transmit the pre-programmed logs (INSPVASB, INSSPDSB). If after 10 minutes the green light does not begin flashing, or if the red light is lit, please see section **C.2**

If the base station has been setup, at this time you will also observe the ***red light*** above the COM2 port blinking. This shows the base station/receiver communication via the radio modems. If this red light is not flashing, please see section **C.2**.

12) Connect the COM1 port of the rover receiver to the serial input of the Interface DSP via the black serial null modem cable.
13) Rover GPS/INS setup complete.

C.49.2.2 Data Acquisition System

The Data Acquisition system consists of the two DSP's and the two PC's. If the Rover GPS/INS calibration above has been complete, then the Client PC should already be powered on and will require no further setup. The following steps explain the DSP and Server PC setup.

1) Connect the batteries of both the DPS's – usually the negative terminal of each battery is disconnected after each use.
2) Verify that the interface DSP has been connected to the COM1 port of the rover receiver via the serial cable.
3) Verify that the Interface DSP is connected to the Master DSP via the two CAN wires (purple/blue) and the ground wire (brown) as shown in Figure **C.6**. These connections are as follows:
    a. CAN wire orientation must be the same on either end of the CAN bus. This means that if the purple wire is next to the jumper on the Interface board, it must also be next to the jumper on the Master board. In both cases, the CAN wire is set on the top row of pins on both boards as shown in Figure **C.6**.
    b. In order to ensure a proper voltage potential between the two boards, ground pins on each board have been connected together. Presumably this can be done at the battery terminals, but this has not been verified. In the current setup, the brown GND wire is connected from the bottom row of the analog input pins on the Interface CAN board (all pins on this row are grounds), to the bottom row of pins on the Master CAN board pictured in Figure **C.6**.

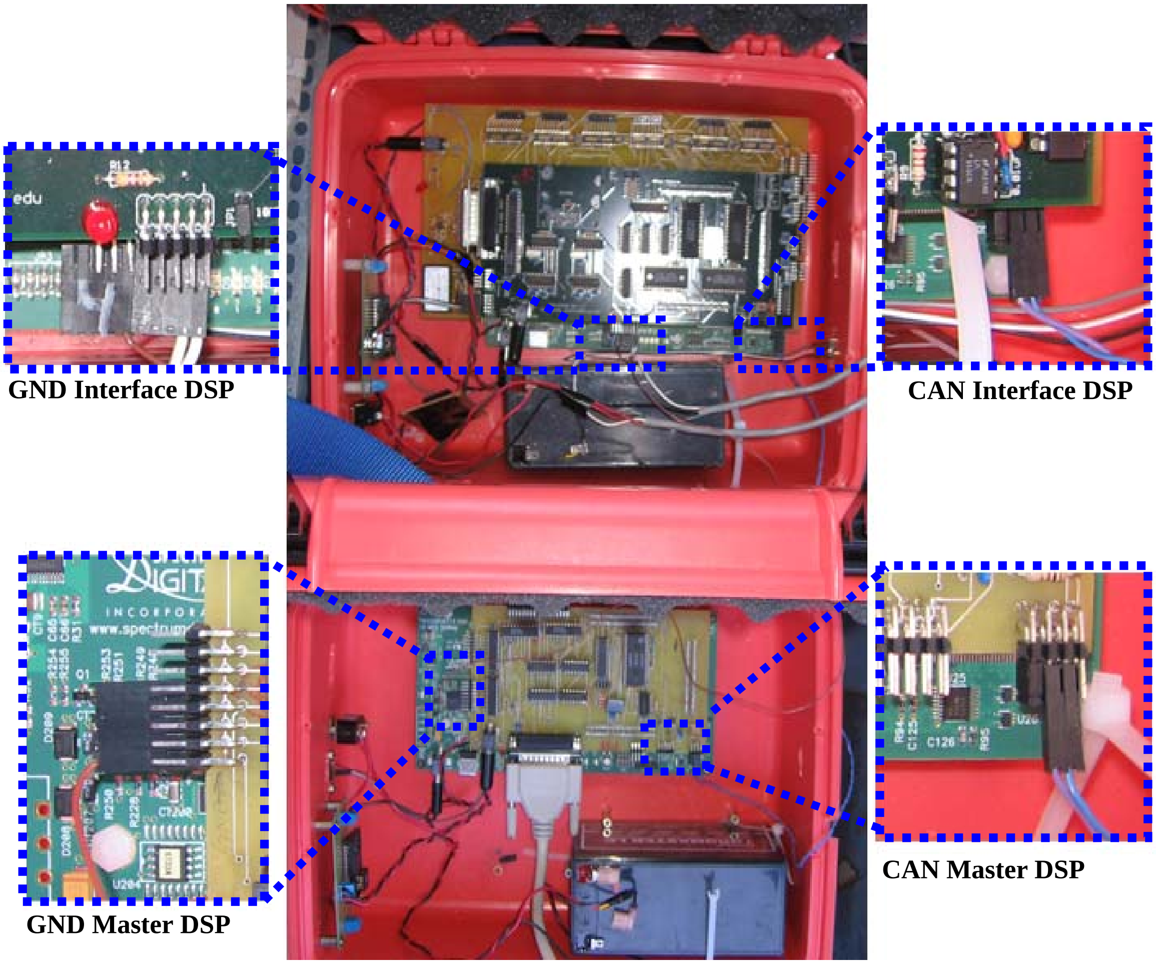

Figure C.6: DSP-DSP Connections

4) Verify that the steering sensors are properly connected to the Inteface DSP. The steering sensors have three connections – power, ground and output voltage. The power and ground are connected to the 15V and -15V lines of the Astrodyne circuit while the output voltage is connected to the analog input pins of the Interface CAN board. This can be seen in Figure C.7 as well as in the GND Interface DSP section of Figure C.6. Further clarification is given below
    a. Figure C.7 shows the steering sensors connected to analog input channels 3 and 4 of the CAN board. The pins used are the rightmost pins on the tops row of the analog input section.

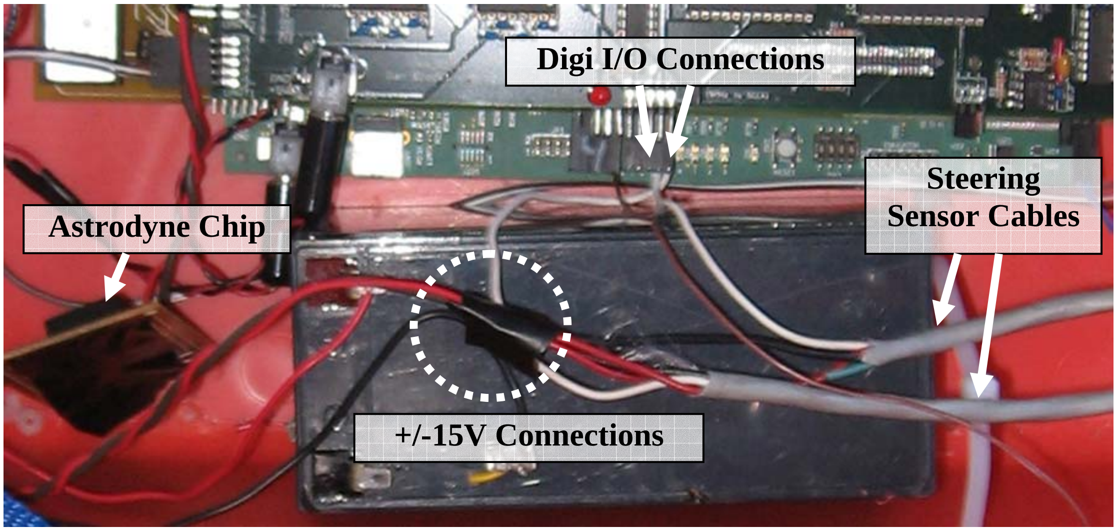

Figure C.7: Steering Sensor Connection

5) Verify that the Master DSP is connected to the Client PC via the parallel port.
6) If all the connections above have been made, turn on the two DSP's by switching the external switch on each enclosure DOWN.
7) Plug the laptop power cord into the power inverter and power on the Laptop.
8) Plug the laptop into the Client PC via the blue crossover Ethernet cable located on the passenger side of the vehicle.
9) Start MATLAB on Laptop (Server PC).
10) Change the MATLAB Directory to: C:\MartiniGPSFiles\GPS_Wincon
11) Start Simulink
12) Open the Simulink model named: gps_data_rd
13) At the top of the model click on Wincon->Build Model
14) When the model is built you will get 3 error messages about not being connected to a client – click OK to all.
15) In the Wincon dialog box, click Client->Recent Clients and select the IP Address of the client. To verify that the Client-Server connection has been made, click Client in the Wincon box and see if the Disconnect option is available. If so, you have been successfully connected. This step is shown in Figure C.8 where the server has already connected to the client.

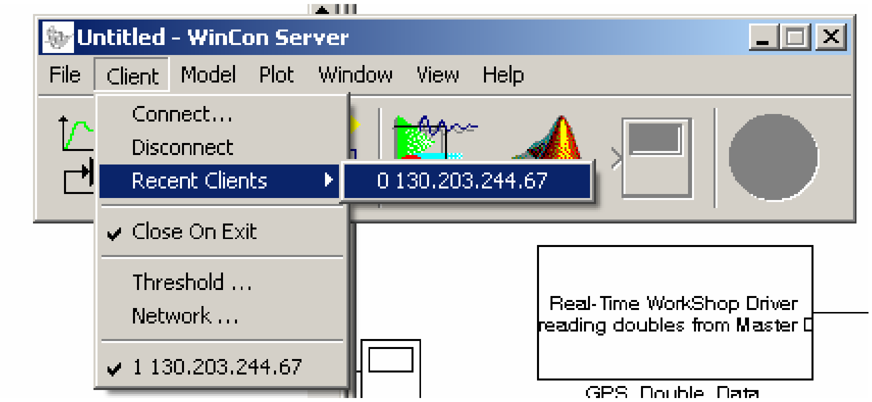

Figure C.8: Connecting to the Client

16) With the Client now connected, build the model again: Wincon->Build Model
17) When the model is done building, the green ***Start*** button will become available.
18) You can now select what you would like to plot by checking the options under the Plot dialog and clicking OK. Click the start button and the data will be viewable in real time. You may have to set the plot axes to make the data viewable in the given window. If the data is not accurate (e.g. you shake the car and the data does not show it) please see

C.49.2.3 Data Acquisition – Saving Data

A script has been written to automatically save each of the variables that are currently available for plotting. The script is located in the GPS_Wincon directory and is named script_saving_routine.m. In order to save your open plots complete the following steps which have been illustrated in Figure C.9:

1) In any open plot, click Update->Freeze All Plots and WAIT for them all to freeze – this will be dependent on how many seconds of data you have saved. In general this is about 3-4 seconds, this process is NOT instant.
2) Go to the MATLAB command prompt, be sure you are in the C:\MartiniGPSFiles\GPS_Wincon folder, and type script_saving_routine. This will save all the variables to the GPS_Wincon folder as *.mat files. You can then select the files and move them to an appropriately named folder. NOTE: If the files are left in the GPS_Wincon folder, they will be overwritten on the next saving command!
3) Go back to the plots and click Update->Real-Time to resume Real-Time data Acquisition.

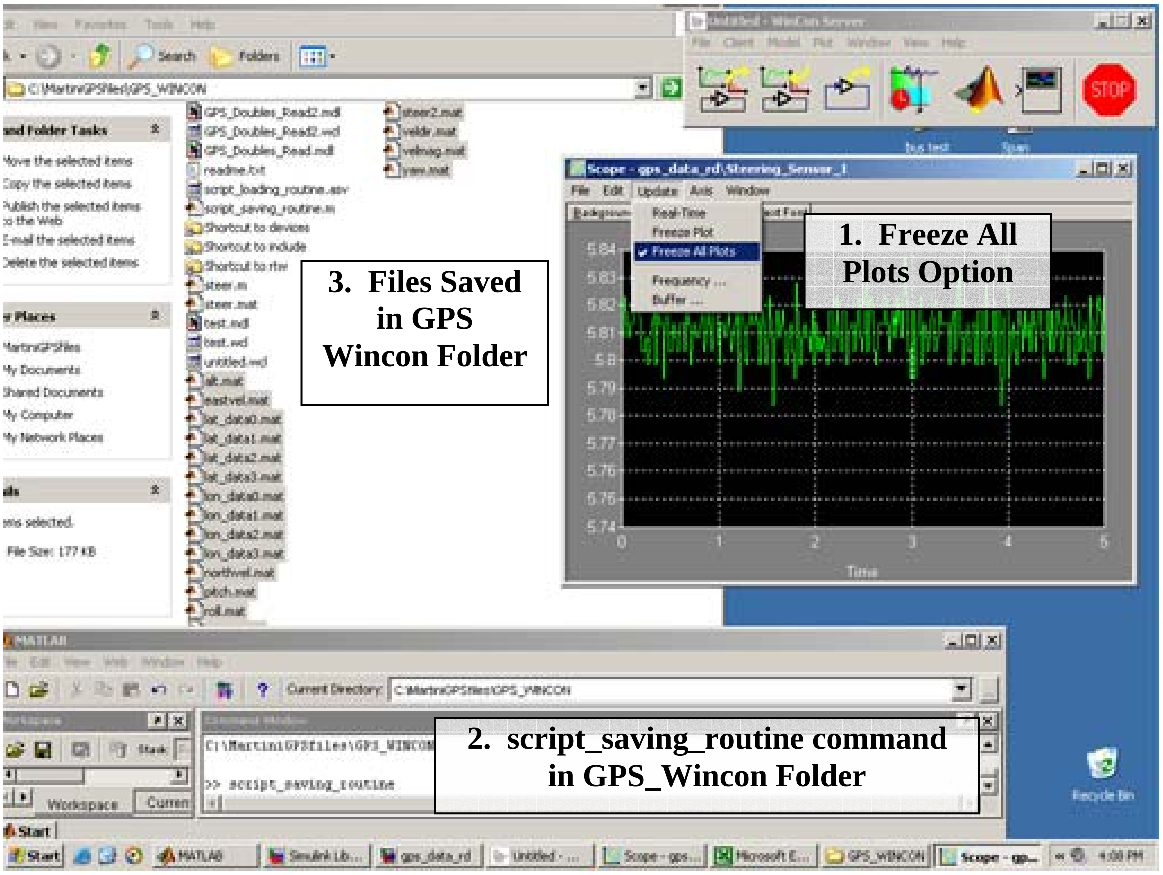

1. Freeze All Plots Option

2. script_saving_routine command in GPS_Wincon Folder

3. Files Saved in GPS Wincon Folder

```
C:\MartiniGPSfiles\GPS_WINCON

>> script_saving_routine
```

Figure C.9: Saving Active Plots

C.2 Troubleshooting

If all the steps described in the previous section are followed, the system should be up and running in approximately 10 minutes. However, it is necessary to include a trouble shooting section incase something does not go as planned. Table C.1 and the subsequent troubleshooting sections can be used if necessary.

Table C.1: Troubleshooting Table

Component	Symptom	Possible Causes	Solution
Base Station	Not in FIX mode	Not enough satellites in view	View status in GPSolution
		Receiver needs to be re-programmed with current position	See Section **B.2.1**
	No Correction Transmission (COM2 Green Light not Flashing)	Receiver not in FIX mode	See Above
		Receiver needs to be re-programmed to transmit corrections	See Section **B.2.1**
Rover GPS/INS	No Log Transmission (COM1 Green Light not flashing)	Not enough satellites in view/Calibration not complete	View Status in GPSolution
		Receiver needs to be re-programmed to send logs	See Section **B.2.2**
	No Corrections being received (COM2 Red Light not flashing)	Radio Modem not powered	Power it
		Radio Antenna not connected	Connect it
		Base Station not sending corrections	See Above
		Radio Modem's are not connectiong	See Section **B.2.3**
		Receiver needs to be re-programmed to reveive corrections	See Section **B.2.2**
Data Acquisiton	Server will not connect to Client	Ethernet crossover cable not connected	Connect it
		Wrong IP Address used	Verify this
		Client not powered on	Power it
		Client did not start Wincon Client	Restart Client
	Wincon data reads ***Infinity***	Master DSP not connected to Client PC	Connect Parallel Port
		Master DSP battery is dead	Check it/Replace It
		Master DPS needs to be restarted	Turn it off and back on
		Signals are noisy	See Section **B.2.4**
	Wincon data ***Flat Lines or Reads Zero***	Interface DSP is not connected to Reveiver	Check Serial Cable
		Receiver is not sending logs	See Above
		Interface DSP battery is dying	Check it/Replace It
		Inteface DSP needs to be restarted	Turn it off and back on

C.50.1 Reprogramming the Base Station

On occasion the memory of the Base Station receiver will be cleared. A common symptom is the receiver's inability to automatically fix its position and therefore transmit differential corrections. In this situation, the Base Station should be reprogrammed by doing the following:

1) Connect the COM1 serial port to that of the PC which will be used to program the receiver.
2) Open the GPSolution4 software on the PC and select Device->Open->New and enter a name e.g. "BASE Station"
3) Press Settings, select COM1 from the PC Port Dropdown
4) Set the Baud Rate to 115200 and uncheck the "Use Hardware Handshaking"
5) Select OK, and then OK and OPEN to open the new device.
6) If GPSolution4 connects to the receiver, skip to step 8
7) Navigate though the receiver's menus via the onboard LCD to the COM Port settings. Make sure that COM1 has been set to a baud rate of 115200, and COM2 has been set to a baud rate of 57600.
8) In the command window of GPSolution4 (with no other windows open), enter the following commands

```
unlogall
Interfacemode com2 none rtcm off
log com2 rtcm1 ontime 5
log com2 rtcm3 ontime 10
log com2 rtcm22 ontime 10,1
log com2 rtcm1819 ontime 1
fix positon 40.86313783175 -77.834902735600 367.3535
saveconfig
```

9) When the receiver has located four satellites, it will display "FIX" on the LCD and begin to transmit the corrections as seen by the flashing green light above the COM2 port.

C.50.2 Reprogramming the Rover Station

As with the base station, the rover station may need to be reprogrammed. A symptom of this would be if after 10 minutes the receiver has not yet begun to transmit logs to the

Interface DSP (no flashing green light above the COM1 port). To reprogram the Rover do the following

1) Perform steps 1-7 of section **C.50.1** with the rover receiver.
2) Enter the following commands (with all other windows closed)

```
unlogall
interfacemode com2 rtcm none off
setimutype IMU_HG1700_AG17
interfacemode aux imu imu OFF
interfacemode com2 rtcm none off
log insspdsb ontime 0.02
log inspvasb ontime 0.02
saveconfig
```

3) When the receiver has located four satellites and the IMU has been aligned, the receiver will transmit data logs to the Inteface DSP indicated by the flashing green light above the COM1 port. Also the red light above the COM2 port will be flashing, indicating that the receiver is communicating with the base station.

C.50.3 Reprogramming the Modems

Although it has not yet been necessary, in the future it may be necessary to reprogram the modems responsible for the receiver-receiver communication. This procedure will be outlined here:

C.50.3.1 Base Station Modem

1) Power the Base Station modem and plug it into the computer via the Serial cable, ***DO NOT*** use a NULL MODEM cable. The radio will not be able to communicate with the PC. You need a straight RS-232 cable.
2) Insert freewave software cd and start EZ-setup 2.0. If you do not have the CD, download the software from the freewave website under the Software Tools tab. I suggest against using the Hyper Terminal method mentioned in the book.
3) Select the com port you will be working from (should be 1 by default)
4) Use the settings displayed in the figures below:

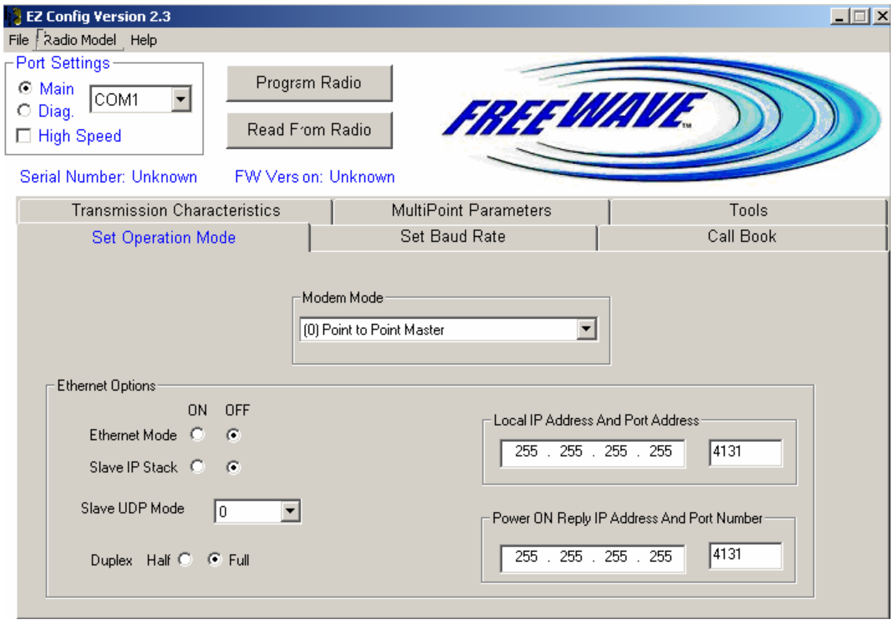

Port Settings
● Main ○ Diag. COM1
□ High Speed

Serial Number: Unknown FW Vers on: Unknown

Modem Mode: (0) Point to Point Master

Ethernet Options

	ON	OFF
Ethernet Mode	○	●
Slave IP Stack	○	●

Slave UDP Mode: 0

Duplex: Half ○ ● Full

Local IP Address And Port Address: 255 . 255 . 255 . 255 4131

Power ON Reply IP Address And Port Number: 255 . 255 . 255 . 255 4131

Figure C.10: Base Station Modem Operation Mode

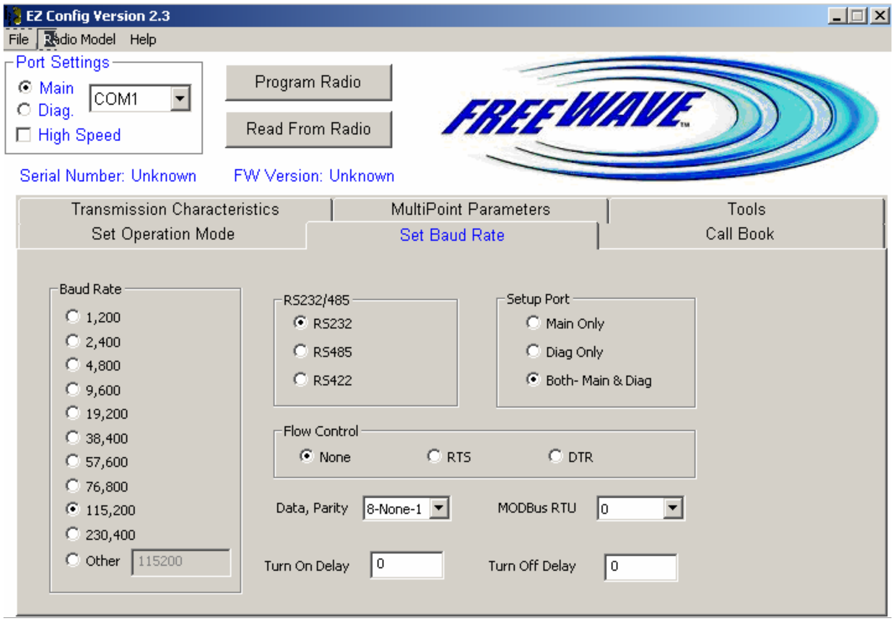

Port Settings
● Main ○ Diag. COM1
□ High Speed

Serial Number: Unknown FW Version: Unknown

Baud Rate
○ 1,200
○ 2,400
○ 4,800
○ 9,600
○ 19,200
○ 38,400
○ 57,600
○ 76,800
● 115,200
○ 230,400
○ Other 115200

RS232/485
● RS232
○ RS485
○ RS422

Setup Port
○ Main Only
○ Diag Only
● Both- Main & Diag

Flow Control
● None ○ RTS ○ DTR

Data, Parity: 8-None-1
MODBus RTU: 0
Turn On Delay: 0
Turn Off Delay: 0

Figure C.11: Base Station Modem Baud Rate Settings

5) Under the Call Book tab, enter the serial number of the ***ROVER***'s modem in the Entry To Call 0 field in the Number Tab. This should be the only number listed.

6) Click the Program Radio button
7) Press the black setup button on the back of the modem and wait for programming to complete.

C.50.3.2 Rover Station Modem

The procedure for programming the Rover Station modem is nearly identical to that of the Base station with only two changes:

1) Under the “Set Operation Mode” tab, change the Modem Mode to Point to Point Slave.
2) When programming the Call book, you have to enter the serial number for the ***BASE STATION’s*** modem.

NOTE: If you are planning to use the radios short range, or to bench test them, you may want to lower the “Transmit Power” on the “Transmission Characteristics” tab to a number like 1-2 instead of 10. This will stop the radios from “screaming” at each other.

C.50.3.3 Modem Loop Testing

There is a simple bench test you can do to determine if the radio communication has been successful. This method was suggested by the FreeWave customer support. With the radio transmission powers set to appropriate levels, do the following:

1) Connect the Base Station modem to the PC via the serial port.
2) Start Hyper Terminal: Start/Programs/Accessories/Communications/Hyperterminal
3) Create a new connection name called FreeWave and press OK
4) Change the Connect Using pulldown to COM1 and press OK
5) Change the COM1 Properties to the following and press OK:
    a. Baud Rate: 57600
    b. Data bits: 8
    c. Partity: None
    d. Stop bits: 1
    e. Flow control: None

6) Plug the power into the Rover's radio, and connect a serial cable to it as usual. Instead of plugging the Slave into the computer, short out Pins 2 and 3 on the other end of the serial cable using a jumper wire or a paper clip. (These are the transmit and receive lines)
7) On the PC which is connected to the Base Station, start typing in the Hyperterminal program. If what you type shows up on the screen, the radios are successfully communicating with each other. If nothing shows up, go back and check your settings. If what shows up is gibberish, then your baud rates are mis-matched.

C.50.4 Data Acquisition Troubleshooting

The majority of the errors regarding the data acquisition system are usually solved by simply reviewing the connections. Missing parallel, serial or ethernet connections are the primary sources. However, there has been an instance where these were not the problems. On occasion, Wincon will display values of infinity for all of the variables being recorded 99% of the time this indicates a missing parallel port connection, or a dead Master DSP battery. It has been seen that noise has also played a part in this error. An easy way to check for this is to do the following:

1) With the Rover receiver powered, calibrated and sending data logs, disconnect it from the Interface DSP at the DSP end (The serial cable should remain connected to the Rover receiver). Since this receiver is only sending messages on the COM1 port, only the ***green*** light should be lit. On occasion, when you disconnect the interface DSP the red light will illuminate as well.
2) If the red light is illuminated, move the serial connector on the receiver-side left or right until the red light turns off.
3) Reconnect to the Interface DSP and see if issue is resolved